

Master Thesis

Signal and background studies for scalar leptoquark pair production in the $t\bar{t} + 2\tau$ channel at the ATLAS experiment

Daniel Adlkofer



Supervisor
Prof. Dr. Raimund Ströhmer

Advisor
Dr. Mahsana Haleem

January 2019

Lehrstuhl für Physik und ihre Didaktik
Physikalisches Institut
Julius-Maximilians-Universität Würzburg

Summary

Grand unified theories has been introduced to solve some of the open questions that are not explained by the standard model of particle physics like the symmetry between quarks and leptons. Within such models the connection between the weak and strong sector are established with new gauge bosons called leptoquarks. The Large Hadron Collider with its capability to collide protons at a center of mass energy of 13 TeV has with the ATLAS detector the ideal instrument to search for new exotic particles like leptoquarks. Within the context of pair produced leptoquarks one possible decay within the minimal-Buchmüller-Rückl-Wyler model involves the $t\tau^- + \bar{t}\tau^+$ state. Due to this complex final state involving the heaviest quark and heaviest lepton, signal and background studies are performed at the ATLAS experiment in order to determine the tau reconstruction efficiencies and fake rates.

This is achieved with a set of two Monte Carlo samples that model the standard model background ($t\bar{t}$ and $t\bar{t}H$) and two Monte Carlo samples that model a hypothetical leptoquark signal with a mass point of 500 GeV and 1 TeV. Furthermore datasets from the ATLAS data-taking periods in 2015-2018 are used for a comparison between data and simulation. Within an event selection that addresses the final state of the leptoquark pair, fake candidates like jets faking a hadronic tau show a strong jet p_T dependence on the fake rate as determined from the background samples. Tau reconstruction efficiencies for the leptoquark signal samples leads to the conclusion that the efficiency only slightly depends on the taus' reconstructed p_T , whereas the efficiency is dependent on the minimum and maximum separation between taus and different objects like jets, b-jets or light leptons.

Kinematic distributions like the reconstructed tau p_T or the sum of all objects' transverse momentum S_T provide insight to the quality of signal extraction from the background and represent good discriminating variables. This fact is quantitatively confirmed in an evaluation of the discovery significance for both leptoquark samples. Within the significance consideration values for the transverse momentum of the reconstructed tau and the kinematic variable S_T are proposed to cut on for a further significance increase. Furthermore the significance is extrapolated depending on the branching fraction of the leptoquarks decaying into a top-pair and tau-pair.

Zusammenfassung

Große vereinheitlichte Theorien stellen eine Möglichkeit dar, um ungelöste Fragen des Standard Modells der Teilchenphyik zu erklären. Ein Beispiel hierfür ist die Symmetrie zwischen Quarks und Leptonen. Die Verbindung zwischen dem schwachen und starken Kraftsektor wird durch neu eingeführte Eichbosonen, den sogenannten Leptoquarks, hergestellt. Am Large Hadron Collider, der Protonen mit einer Schwerpunktsenergie von 13 TeV zur Kollision bringt, ist der ATLAS Detektor das ideale Instrument für eine Suche nach neuen, exotischen Teilchen wie den Leptoquarks. Im Rahmen der Paarproduktion von Leptoquarks ist der Zustand $t\tau^- + \bar{t}\tau^+$ ein möglicher Endzustand des Leptoquarkzerfalls, der durch das minimale-Buchmüller-Rückl-Wyler Modell erlaubt ist. Aufgrund seiner komplexen Zerfallsstruktur, die das massereichste Quark und das massereichste Lepton enthält, wurden Signal- und Untergrundstudien mithilfe des ATLAS Experiments durchgeführt, um die Rekonstruktionseffizienzen und Fehlidentifikationen von Tau Leptonen zu bestimmen.

Dies wurde mithilfe von Monte Carlo Simulationen der Untergrundprozesse ($t\bar{t}$ and $t\bar{t}H$) und von Simulationen, die das hypothetische Leptoquarksignal mit den zwei unterschiedlichen Massepunkten von 500 GeV und 1 TeV modellieren, erreicht. Außerdem wurden Daten des ATLAS Detektors für eine Gegenüberstellung genutzt, die während der Datennahmen aus den Jahren 2015-2018 gemessen wurden. Durch eine Ereignisselektion die dem Endzustand der Leptoquarkpaare angepasst ist, konnte anhand der Simulationen des Untergrunds festgestellt werden, dass die Fehlidentifikation von Jets als Tau Leptonen eine starke Transversalimpulsabhängigkeit aufweist. Die Rekonstruktionseffizienzen von Tau Leptonen für die Leptoquarksimulationen führen zu dem Schluss, dass die Effizienz nur schwach vom Transversalimpuls der rekonstruierten Tau Leptonen abhängen, während die Effizienz durchaus eine Abhängigkeit vom minimalem und maximalem Abstand zwischen Taus und verschiedenen Objekten wie Jets, b-Jets oder Leptonen aufweist.

Kinematische Verteilungen wie der rekonstruierte Transversalimpuls der Tau Leptonen p_T oder die Summe der Transversalimpulse aller physikalischer Objekte S_T geben Einblick in die Qualität der Signalextraktion aus den Untergrundprozessen und repräsentieren gute Diskriminanten. Dieser Umstand wird quantitativ in der Bestimmung der Entdeckungssignifikanz für beide Leptoquark Simulationen bestätigt. Innerhalb der Signifikanzbetrachtung wurden außerdem Werte für den Transver-

salimpuls der rekonstruierten Tau Leptonen und der kinematischen Variable S_T bestimmt bei deren Beschnitt die Signifikanz weiter erhöht werden konnte. Weiterhin wurde die Signifikanz für unterschiedliche Verzweigungsverhältnisse der Leptoquarks beim Zerfall in ein top-Paar und Tau-Paar berechnet.

Contents

1	Introduction	8
2	Theoretical background for the search for scalar leptoquarks	10
2.1	The Standard Model of particle physics	10
2.2	Beyond the scope of the Standard Model	14
2.3	Leptoquarks	16
2.3.1	Leptoquarks and grand unified theories	17
2.3.2	Effective Leptoquark model	17
2.3.3	Leptoquark-like couplings in supersymmetry	19
2.3.4	Leptoquark pair production in proton-proton collisions	20
2.3.5	Current status in the search for scalar leptoquarks	20
2.3.6	Starting point and research question for the analysis	23
3	Experimental setup for the search for scalar leptoquarks	27
3.1	The Large Hadron Collider accelerator complex	27
3.2	The ATLAS detector at the LHC	29
4	Turning detector signatures into physical objects	34
4.1	Electron reconstruction at ATLAS	34
4.2	Muon reconstruction at ATLAS	36
4.3	Jet reconstruction at ATLAS	37
4.4	b-jet reconstruction at ALTAS	38
4.5	Tau reconstruction at ATLAS	40
4.6	Monte Carlo simulations	41
5	Analysis	43
5.1	Datasets and Monte Carlo samples	43
5.2	Physical object selection	47
5.3	Event selection	49
6	Results	51
6.1	Number of event candidates	51

6.2	Signal and background efficiencies	53
6.2.1	Tau reconstruction efficiencies and fake rates	53
6.2.2	Taus reconstruction efficiency in signal samples	64
6.3	Kinematics	76
6.4	Discovery significance	94
7	Conclusion	101
	List of figures	104
	List of tables	105
	Bibliography	113

Introduction

The cornerstones for today's understanding of nature are based on successful theories like quantum mechanics and the theory of general relativity. Over centuries the discovery of new phenomena and the constant development of theoretical concepts helped to expand the frontiers of the knowledge - and this process is still in progress. Theoretical concepts based on empirical evidence are a great opportunity in order to get deeper insight into the nature of matter, forces, space and time with the ambition to deduce an universal description of the laws of nature. Within this evolving gain of knowledge the concept of symmetry was and is an appealing tool and indeed, symmetries are deeply connected with conservation laws formulated in Noether's theorem.

Four fundamental forces are known today. That is the electromagnetic, weak and strong force as well as gravity. The standard model of elementary particle physics describes the fundamental components of matter and their interactions induced by the electromagnetic, weak and strong force. Its development profited crucially from symmetry considerations and its formulation is realized with relativistic quantum field theory. Understanding particles as elements of symmetry groups made it possible to formulate the electroweak unification, bringing together the electromagnetic and weak force. Undisputably, the standard model is a powerful theory capable of describing the constituents of matter and their fundamental interactions and explains the phenomena encountered in this context. Nevertheless some open questions remain. Amongst others these are the puzzle of neutrino masses, the hierarchy problem or difficulties in formulating a theory of quantum gravity.

Thinking within the picture of symmetry it is very attractive to solve some of the open questions by further unifying the fundamental forces into a grand unified theory, which eventually includes gravity. This would imply the existence of new gauge bosons called leptoquarks. Leptoquarks are colored particles carrying both lepton and baryon number and act as mediators between leptons and quarks. In one of the simpler scenarios possible decay modes involve a top-quark pair and a tau lepton pair and would be a hint to such exotic particles. Leptoquark masses are possibly in reach of today's particle accelerators like the LHC at the research center

CERN and could be detected with the ATLAS detector. For this purpose it is crucial to understand tau reconstruction efficiencies for future search strategies in this specific $t\tau^-\bar{t}\tau^+$ channel. This work gives insight into tau reconstruction efficiencies and background contributions to a possible leptoquark signal.

The structure of the thesis is as follows: Chapter 2 gives an overview of the standard model of particle physics. Furthermore it presents issues, which are beyond the scope of the standard model and some approaches to solve these puzzles. One possibility is the introduction of leptoquarks in the context of grand unified theories. Within this chapter the research question of the thesis is discussed. Chapter 3 describes the experimental setup for the analysis. That is the hadron collider complex LHC and the ATLAS detector. An introduction into physical object reconstruction can be found in chapter 5.2. Chapter 5 presents the analysis framework with the object and event selection criteria as well as datasets used for the analysis. In chapter 6 the results of the efficiency and background study are presented. Also different kinematic distributions of signal and background events are compared to data. Additionally, insight into the discovery significance of the leptoquark Monte Carlo simulations is given here.

Theoretical background for the search for scalar leptoquarks

This chapter describes theoretical foundations required for the search for scalar leptoquarks including the successful Standard Model of elementary particle physics evolved from the symbiosis of experimental achievements and theoretical milestones. Besides its success some issues still remain unsolved and could be a hint to physics beyond the Standard Model, giving space to introduce the Leptoquark Model as one possible extension.

2.1 The Standard Model of particle physics

A remarkable development for understanding nature is the Standard Model (SM) of particle physics, embracing physics at the most fundamental level. This quantum field theory, incorporating the conceptual frameworks of special relativity and quantum mechanics, describes the constituents of matter and the laws governing their interactions. [1] Despite its success of being the most promising theory so far capable of explaining the observed results within its domain in agreement with empirical data, it seems not to be the complete story. [2]

One of the most important concept in physics is that of symmetries, because they are deeply connected with conservation laws, following Noether's Theorem. A physical property responds to a symmetry transformation in two different ways. It can appear in form of an invariant under symmetry transformation, leaving that property unchanged, or as covariant, changing their property induced by the symmetry transformation. Fundamental symmetries of particle physics include space translation symmetry and hence the conservation of momentum, rotational invariance and hence conservation of angular momentum and time translation invariance leading to energy conservation. The formal mathematical description for fundamental symmetries is based on group theory. In case of particle physics almost all

group	defining property	application
$U(n)$	$n \times n$ unitary ($U^\dagger U = 1$)	$U(1)$ electromagnetism
$SU(n)$	$n \times n$ unitary ($U^\dagger U = 1$)	$SU(2)$ weak interactions
	with $\det U = 1$	$SU(3)$ strong interactions
$SO(n)$	$n \times n$ orthogonal ($O^\top O = 1$)	$SO(3)$ rotations
	with $\det O = 1$	$SO(3, 1)$ Lorentz transformations

Table 2.1: Lie symmetry groups for the gauge interactions of the Standard Model [1].

groups are Lie groups \mathcal{G} , that are a set of objects $\{g_i\}$, which can be combined with a binary operation and has four basic properties: closure, identity, inverse element and associativity. Additionally, the group elements are continuous and differentiable functions of some finite set of parameters θ_a :

$$g = g(\theta_1, \dots, \theta_N) = \exp[i\theta_a \mathbf{T}^a] = \exp[i\vec{\theta} \vec{\mathbf{T}}] \quad \text{with } a = 1, \dots, N \quad (2.1)$$

Here \mathbf{T}^a are the generators of the group from which all elements of the group can be created. The irreducible representatives of a group can be written as complex matrices*, acting on the wave function of the particles and on charges as well as on space-time coordinates. [1] The local symmetry $SU(3)_c \times SU(2)_L \times U(1)_Y$ summarizes the gauge interactions of the SM (see table 2.1). Here c indicates the strong force, L the left handed chirality of the weak regime and $Y = B + s$ the hypercharge calculated from baryon number B and strangeness s . [3] Besides the continuous symmetries above also important discrete symmetries exist in the SM like parity P , referring to the transformation $\vec{x} \rightarrow -\vec{x}$, time reversal T , referring to $t \rightarrow -t$, and charge conjugation C , corresponding to the exchange of a particle with its anti-particle. The weak force breaks P and C , but not the product of CPT . [2]

Matter and its interactions can be described by two basic types of particles and four fundamental forces, i.e. the electromagnetic force, the weak and the strong force and gravity. Fermionic particles, following Fermi-Dirac statistics, make up matter, whereas bosons, following Bose-Einstein statistics, are acting as mediators of the fundamental forces. [4][5]

*Irreducible means that not all representing matrices of the group can be decomposed into block-diagonal form simultaneously [1].

The fermions can be further categorized into 6 leptons l characterized through the lepton quantum number L_l and 6 quarks q characterized through the baryon quantum number B together with their anti-particles (\bar{l} respectively \bar{q}). The difference between particle and anti-particle are the contrary charges and contrary lepton and baryon number respectively, whereas mass, mean lifetime and spin stay the same. Leptons occur in three generations with different flavor – electron (e), muon (μ) and tauon (τ) – and can carry electrical charge $Q = \pm e$ in units of the elementary charge. The electrically neutral leptons are the neutrinos ν_l . [5]

Table 2.2 shows the leptons with selected properties.

The quarks also occur in three generations and carry electrical charge of either $Q = \mp \frac{1}{3}e$ or $Q = \pm \frac{2}{3}e$ in units of the elementary charge as well as color charge. The new type of charge can be introduced, because the quarks lie in the fundamental representation of $SU(3)$. Possible color charges are red, green and blue and the additional anti-colors indicate that quarks are interacting with the strong force among the electromagnetic and weak interaction. [5] Quarks only occur confined in color-neutral compound systems called hadrons. Baryons are three-quark hadronic states with baryon number 1 and mesons are quark-anti-quark hadronic states, having a baryon number of 0. [4] The reason for quark confinement can be found in the potential $V(r)$ between quarks and anti-quarks depending on distance r . The potential has the shape $V(r) \propto \frac{-1}{r} + \text{const} \cdot r$. When separating a quark-anti-quark pair, additional potential energy must be supplied, which can exceed the potential $V(R) > 2m_q$ for more than two quark masses at distance R . Quantum fluctuations result in the origin of a new quark pair in between. The final state now consists of two pairs, again externally color-neutral. [2] Table 2.2 shows the different quark flavors up, down, charm, strange, top and bottom with some characteristic properties. The bosons shown in table 2.2 are the quanta of the fundamental forces [4]:

- The photon γ is the mediator of the electromagnetic force.
- Three mediators Z^0 , W^+ and W^- for the weak force.
- 8 colored gluons as mediators for the strong force.
- The Higgs boson H^0 as quantum of the Higgs field, providing the masses for the elementary particles.

At the current state of research a quantum field theory of gravity is purely hypothetical. The mediator for such theory would be the graviton (see chapter 2.2). A second aspect is that on elementary particle scales gravity is insignificant com-

leptons					
l	L_l	B	Q/e	$m/\frac{\text{MeV}}{c^2}$	Spin S_z/\hbar
e^-	$L_e = 1$	0	-1	0.511	$\frac{1}{2}$
ν_e	$L_e = 1$	0	0	$< 2 \cdot 10^{-6}$	$\frac{1}{2}$
μ^-	$L_\mu = 1$	0	-1	106	$\frac{1}{2}$
ν_μ	$L_\mu = 1$	0	0	$< 2 \cdot 10^{-6}$	$\frac{1}{2}$
τ^-	$L_\tau = 1$	0	-1	$1.78 \cdot 10^3$	$\frac{1}{2}$
ν_τ	$L_\tau = 1$	0	0	$< 2 \cdot 10^{-6}$	$\frac{1}{2}$

quarks					
q	L_l	B	Q/e	$m/\frac{\text{MeV}}{c^2}$	Spin S_z/\hbar
u (up)	0	$\frac{1}{3}$	$\frac{2}{3}$	2.2	$\frac{1}{2}$
d (down)	0	$\frac{1}{3}$	$-\frac{1}{3}$	4.7	$\frac{1}{2}$
c (charm)	0	$\frac{1}{3}$	$\frac{2}{3}$	$1.3 \cdot 10^3$	$\frac{1}{2}$
s (strange)	0	$\frac{1}{3}$	$-\frac{1}{3}$	95	$\frac{1}{2}$
t (top)	0	$\frac{1}{3}$	$\frac{2}{3}$	$17 \cdot 10^4$	$\frac{1}{2}$
b (bottom)	0	$\frac{1}{3}$	$-\frac{1}{3}$	$4.2 \cdot 10^3$	$\frac{1}{2}$

gauge bosons					
boson	L_l	B	Q/e	$m/\frac{\text{GeV}}{c^2}$	Spin S_z/\hbar
γ	0	0	0	0	1
Z^0	0	0	0	91.2	1
W^-	0	0	-1	80.4	1
W^+	0	0	+1	80.4	1
g	0	0	0	0	1
H^0	0	0	0	125	0

Table 2.2: Overview of leptons l , quarks q and gauge bosons as mediators of the fundamental forces with some selected properties and quantum numbers like electrical charge Q , mass m , lepton number L_l and baryon number B . [2][6]. The fermion anti-particles are not shown, which would have opposite charges and lepton/baryon number.

pared[†] to all other forces and is therefore not originally considered in the SM. [4]

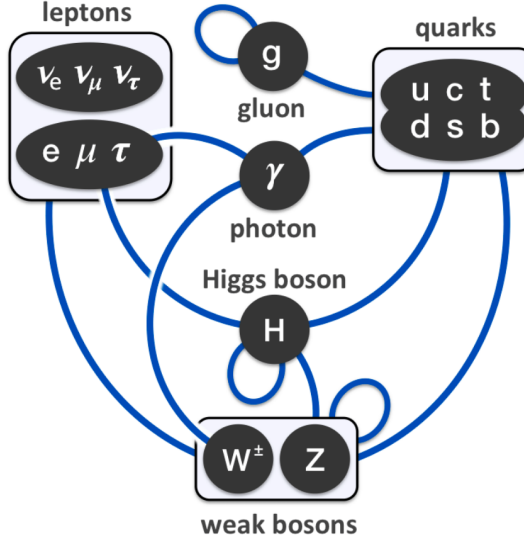


Figure 2.1: The Standard Model with its fermions and bosons and the involved interactions. The solid blue line indicates which particles interact with each other through the mediators, including self-interaction. [7]

Figure 2.1 summarizes the picture of the SM with its fermions and bosons. The lines indicate which particles interact with each other through the mediators, including self-interaction.

2.2 Beyond the scope of the Standard Model

Nevertheless, there are still many puzzles left which are not described by the SM. This circumstance keeps physicists well motivated to gain further progress and to push the frontiers of our understanding. [2] In the following some of the issues are briefly described, like neutrino masses, quantum gravity, the hierarchy problem and supersymmetry.

Neutrino masses are confirmed by various neutrino oscillation experiments [8][9], although the SM does not predict neutrino masses. The neutrino flavor states ν_α with

[†]Relative strength of gravity compared to the weak interaction is 10^{-35} [1].

$\alpha = e, \mu, \tau$ are quantum entangled with the mass states ν_i where $i = 1, 2, 3$ described by an unitary matrix $U_{\alpha i}$ [10]. One possible extension of the SM, explaining neutrino masses, is the seesaw mechanism. Because of the absence of the right chirality spinor components $\Psi_{R,j}$, the mass term of the Dirac lagrangian $\bar{\Psi}_L \Psi_R + \bar{\Psi}_R \Psi_L$ cannot be formed in case of neutrinos. One possible solution is to describe the neutrino masses with a Majorana mass term, which introduces very massive right-chiral neutrinos* besides light weight left-chiral neutrinos. One caveat is that such right-chiral neutrinos as a consequence have to exist, although within the SM there are only left-handed neutrinos known. [2]

Quantum gravity could be the embedding of general relativity into a framework of quantum theory. Quantum theory provides a well confirmed framework for all theories describing particular interactions. Therefore it would be appealing to have a quantum formulation of gravity, following the example of all other fundamental forces and being one step closer to an unified description. From the point of view of cosmology, quantum gravity could be an encompassing theory for a more fundamental understanding where general relativity breaks down, when it comes to the initial conditions of the early universe or conditions of black holes. [11]

The hierarchy problem is a current challenge in particle physics and arises from quadratic corrections to the weak scale. [12] The hierarchy problem formulates the large differences of scales at which symmetries are broken. Considering a single, unifying symmetry, including the standard model symmetries $SU(3)_c \times SU(2)_L \times U(1)_Y$ (see chapter 2.1), which has to be broken at scale V , because it is not manifested at the currently explored energy scales. A lower bound is $V \approx 10^{37} \text{ GeV}$. At the same time spontaneous symmetry breaking takes place for $SU(2)_L \times U(1)_Y$ at scales of $v \approx 246 \text{ GeV}^\dagger$ in order to allow for massive W^\pm and Z^0 bosons as well as massive quarks and leptons. Within the framework of perturbation theory in quantum field theory such great scale differences are difficult to keep due to the fact that corrections of symmetry breaking are controlled by the highest masses involved. One approach for v is $v^2 = v_0^2 \sum_{i=1}^k c_i \lambda^i V_0^2$ with the initial value v_0 , the coupling constant λ and general coefficients c_i . This shows that including the first order of correction, the equation becomes $v^2 = v_0^2 + c_1 \lambda V_0^2$. The consequence is that v_0^2 has to be adjusted in such a way that it cancels out several decimal places, for instance 25, of the term $c_1 \lambda V_0^2$, but the decimal places beyond that limit should add up to the scale of 246 GeV. This fine tuning is an unsatisfactory situation, even worsened by

*The large masses are consistent with the lack of evidence for right-chiral neutrinos at present day energies [2].

^{\dagger}This is the vacuum expectation value for the Higgs field. [13]

adding more orders of quantum corrections. [2] A non-perturbative solution to the hierarchy problem is proposed by supersymmetric models. [14]

Supersymmetry (SUSY) is a theory, which unifies fermions and bosons. The corresponding transformation can be described by an operator in spinor form $Q_{\alpha i}$ and converts fermion fields into boson fields and vice versa. Here α is the spinor index and i are internal degrees of freedom. The field pairs are called superpartners (sparticles) and belong to the same multiplet. The difference between particles and sparticles is the spin quantum number which distinguishes them by half an unit of \hbar . [15] Due to the lack of evidence of sparticles in the same mass range as the already known elementary particles, also supersymmetry has to be broken. [3]. SUSY is very attractive, because it can solve the hierarchy problem, achieve gauge unification and can even provide a candidate for dark matter. [16] There are two main categories of supersymmetric models, namely R -parity conserving and R -parity violating models. R is a discrete symmetry in the coupling of particles and their superpartners, defined as [15]:

$$R = (-1)^{2S+3B+L} = \begin{cases} +1 & \text{for ordinary particles} \\ -1 & \text{for SUSY particles} \end{cases}, \quad (2.2)$$

where S is the spin, B the baryon number and L the lepton number. An exactly conserved R -parity will result in a stable lightest supersymmetric particle and the SUSY particles will be produced in pairs. Whereas a R -parity violation will result in singly producable sparticles and all of them are intrinsically unstable. [17]

2.3 Leptoquarks

Different shortcomings of the standard model open up chances to extend the current understanding of elementary particle physics with concepts briefly introduced in chapter 2.2. One basic idea develops the symmetry approach further, taking the current symmetries as an example (see chapter 2.1), into a grand unified theory (GUT). This can be made possible by embedding the SM gauge groups $SU(3)_c \times SU(2)_L \times U(1)_Y$ into a higher symmetry G_{GUT} . This group has to be broken at the so called GUT-scale of $\sim 10^{16}$ GeV to such an extent that the three SM interactions occur as separate interactions below this scale. [3] The previously mentioned issues in chapter 2.2 already gave a clue on this unification concept in different degrees of manifestations and show that GUT can be a solution for different issues, for example

the gauge hierarchy problem [18][19], the generation problem [19], the parameter problem [19] and neutrino masses [20]. GUTs imply new gauge bosons called leptoquarks (LQ), which would explain the strong similarities between leptons and quarks. [16]

2.3.1 Leptoquarks and grand unified theories

The first GUT model was proposed by Georgi and Glashow in 1974 [21]. They proposed that the group $SU(5)$ incorporates all the fermions into one multiplet following the same universal coupling. This enables the possibility to transform leptons and quarks into each other with leptoquarks as mediators. Various global symmetries can embed the SM symmetries, but $SU(5)$ is the simplest one. [22] Although the Georgi-Glashow model had a great impact, this model has been ruled out [23]. It predicts a lifetime of the proton of 10^{30} years, but the current experimental lower limit is 10^{33} years* [5][24].

Another unifying group would be $SO(10)$, which is broken to $SO(10) \rightarrow SU(4)_c \times SU(2)_L \times SU(2)_R$, where the leptons are treated as a forth color. [25] This model is known as Pati-Salam GUT model [26]. Here also the right-handed leptons are included, acting differently than their left-chiral counterparts as it is expected for solutions of the neutrino masses for example. [25]

Other symmetry groups like E_6 , inspired by superstring models, are also candidates for a GUT theory. [27] E_6 has a rank of 6 and is a member of the exceptional Lie groups. Furthermore it can be seen as the natural extension of $SU(5)$ and $SU(10)$ and naturally includes a greater set of particles. These additional particles can be, for instance, interpreted as dark matter candidates. [28]

2.3.2 Effective Leptoquark model

All the GUT models, which are briefly mentioned in section 2.3.1, share a common implication, namely the introduction of new gauge bosons called leptoquarks. This implication can be formulated as an effective theory of leptoquarks for energy scales below the GUT-scale , describing the underlying physical concepts.

*This value is valid for the decay mode $p \rightarrow e^+ K^0$. The predictions of the proton lifetime for other dominant decay modes – relevant in GUT models – are higher and can be found in reference [24].

$ F = 2$ leptoquarks				$ F = 0$ leptoquarks			
LQ	Q/e	T_3	decay	LQ	Q/e	T_3	decay
$S_{0,L}$	-1/3	0	$l_L^- u_L$ or $\nu_L d_L$	$V_{0,L}$	-2/3	0	$l_L^- \bar{d}_R$ or $\nu_L \bar{u}_R$
$S_{0,R}$			$l_R^- u_R$	$V_{0,R}$			$l_R^- \bar{d}_L$
$\tilde{S}_{0,R}$	-4/3	0	$l_R^- d_R$	$\tilde{V}_{0,L}$	-5/3	0	$l_R^- \bar{u}_L$
$S_{1,L}$	-4/3	-1	$l_L^- d_L$	$V_{1,L}$	-5/3	-1	$l_L^- \bar{u}_R$
	-1/3	0	$l_L^- u_L$ or $\nu_L d_L$		-2/3	0	$l_L^- \bar{d}_R$ or $\nu_L \bar{u}_R$
	2/3	1	$\nu_L u_L$		1/3	1	$\nu_L \bar{d}_R$
$V_{1/2,L}$	-4/3	-1/2	$l_L^- d_R$	$S_{1/2,L}$	-5/3	-1/2	$l_L^- \bar{u}_L$
$V_{1/2,R}$	-4/3		$l_R^- d_L$	$S_{1/2,R}$	-5/3		$l_R^- \bar{u}_R$
	-1/3	1/2	$l_R^- u_L$		-2/3	1/2	$l_R^- \bar{d}_R$
$\tilde{V}_{1/2,L}$	-1/3	-1/2	$l_L^- u_R$	$\tilde{S}_{1/2,L}$	-2/3	-1/2	$l_L^- \bar{d}_L$
	2/3	1/2	$\nu_L u_R$		1/3	1/2	$\nu_L \bar{d}_L$

Table 2.3: Overview of the scalar (S) and vector (V) leptoquarks proposed by the minimal-Buchmüller-Rückl-Wyler model with their third component of the weak isospin T_3 , electric charge Q and fermion number F . The fourth column shows possible decay modes of the leptoquarks. [17]

The introduction of the effective leptoquark model closely follows [17]. Leptoquarks are color-triplet scalar (S) or vector (V) bosons having baryon and lepton numbers and carrying fractional electrical charge. [17] A general formulation of an effective Lagrangian for leptoquark interaction with SM fermions was proposed by Buchmüller, Rückl and Wyler [29]. It assumes the following:

- (i) LQs have renormalizable interactions.
- (ii) LQs have interactions invariant under the SM gauge symmetries $SU(3)_c \times SU(2)_L \times U(1)_Y$.
- (iii) LQs couple only to the SM fermions, gauge bosons and the Higgs boson.
- (iv) LQs are required to conserve the lepton number L and the baryon number B separately. They carry the fermion number

$$F = 3B + L \quad (2.3)$$

with $|F| = 0$ or $|F| = 2$.

- (v) Each LQ couples to only one quark-lepton generation, i.e. there are three LQ families.
- (vi) LQs has pure chiral couplings to the SM fermions.

Condition (iv) makes sure that the proton instability is avoided. Condition (v) only allows inter-generational interactions and large tree-level flavor changing neutral currents and flavor universalities. Condition (vi) avoids direct contributions to chirally suppressed meson decays like $\pi \rightarrow e\nu$. The LQ model, fulfilling conditions (i)-(vi), is the so called minimal-Buchmüller-Rückl-Wyler effective model (mBRW) with the Yukawa coupling[†] constant λ . [17]

Fourteen different leptoquark types are proposed and are listed in table 2.3. The same symbol represents LQs of different electric charge within an isospin family, i.e. $S_{1/2,L}$ stands for both, the $S_{1/2}$ state of charge $-\frac{5}{3}$ and for $-\frac{2}{3}$. Here l_X are the left-handed lepton doublets in case of $X = L$ and the right handed lepton singlet in case of $X = R$. This differentiation between left-chirality and right-chirality is also valid for the quarks q_X of up-type ($q = u$) or down-type ($q = d$). Seven of the fourteen LQs are scalars ($S_{0,L}, S_{0,R}, \tilde{S}_{0,R}, S_{1,L}, S_{1/2,L}, S_{1/2,R}, \tilde{S}_{1/2,L}$) and seven are vectors ($V_{0,L}, V_{0,R}, \tilde{V}_{0,R}, V_{1,L}, V_{1/2,L}, V_{1/2,R}, \tilde{V}_{1/2,L}$) with their fermion number $|F| = 0$ and $|F| = 2$. For specific models based on mBRW the branching ratio $\beta(LQ \rightarrow lq)$ is usually fixed to values like 0, $\frac{1}{2}$ or 1. [17]

From the experimentalists' point of view it makes sense to expand the phenomenology of leptoquarks and ease some restrictions of the mBRW model, giving rise to more generic models. This means a broader sensitivity to possibly new physics in the face of already determined exclusion limits. One example is to consider the branching ratio β as a free parameter. Relaxing condition (iv) or (v) in the lepton sector could open new lepton-flavor violating decays. As a result the search for leptoquarks is more sensitive to various possibilities in the decay modes or to restrictions on the LQ-coupling. [17]

2.3.3 Leptoquark-like couplings in supersymmetry

An additional generic picture can result from the point of view of supersymmetry. In R -parity violating SUSY models squarks can produce leptoquark-like signature due to decay modes involving the Yukawa coupling. The left-chiral \tilde{u}_L [‡] squark couples

[†]Yukawa coupling describes the interaction of a scalar field with a scalar or pseudoscalar Dirac field [30].

[‡]Usually the supersymmetric partner particles are denoted with a tilde (\sim).

to a $e^+ + d$ pair similar a leptoquark $\tilde{S}_{1/2,L}$ with an electric charge of $|Q| = \frac{2}{3}e$ would do. Accordingly the \tilde{d}_R squark couples to a $e^- + u$ pair or $\nu_e + d$ pair and mimics a S_0 leptoquark of charge $|Q| = \frac{1}{3}e$. From an experimental point of view, the observation of such a decay is not only restricted to LQ models, but also has implications on constraints for the coupling of squarks in SUSY models. [17]

2.3.4 Leptoquark pair production in proton-proton collisions

For the search of leptoquarks, the mBRW model (see chapter 2.3.2) is taken as a basis.

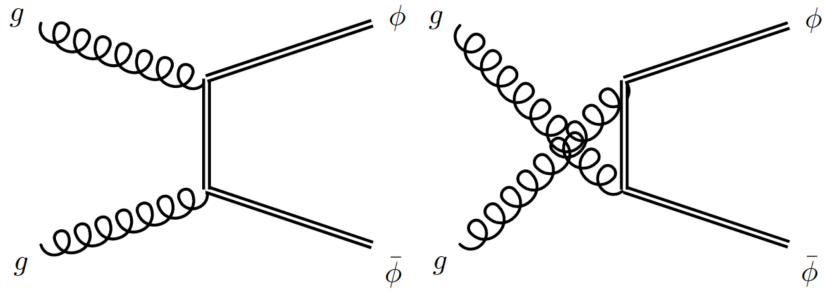
At proton-proton colliders, like the LHC, leptoquarks can be produced in pairs by gluon-fusion and smaller contributions of quark-fusion. These main processes are shown with feynman diagrams in figure 2.2. Figure 2.2a and 2.2b describes the gluon initiated production in the s-, t- and u-channel and figure 2.2c the quark initiated production in the s- and t-channel. The last feynman diagram (lower right) is proportional to the square of the coupling constant (λ^2) due to the virtual lepton exchange [31][32]. Cross section calculations for such processes and further details can be found for example in reference [33]. The detectable final states are governed by the Yukawa coupling λ_{lq} of the leptoquark directly to the quark q and lepton l (see figure 2.3). The model is defined by two parameters derived from λ_{lq} : The branching ratio β and the coupling constant λ . They are connected to the Yukawa coupling constant by $\lambda_{lq} = \sqrt{\beta}\lambda$ for a charged lepton and by $\lambda_{lq} = \sqrt{1-\beta}\lambda$ for neutrinos. [34]

The focus of this thesis lies on the search of pair produced scalar leptoquarks with the final state $LQ + LQ \rightarrow t\tau^- + \bar{t}\tau^+$. These final states would correspond to leptoquarks $S_{0,L}$ and $S_{1,L}$ (cf. table 2.3).

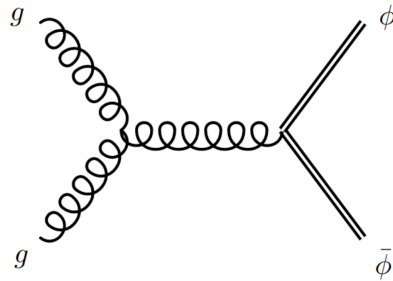
2.3.5 Current status in the search for scalar leptoquarks

Leptoquarks are a promising research field for physics beyond the SM. Various efforts are made with the physics program available at today's particle accelerators to search for LQ-like signatures. The following summarizes briefly the current status for the search for scalar leptoquarks at the LHC.

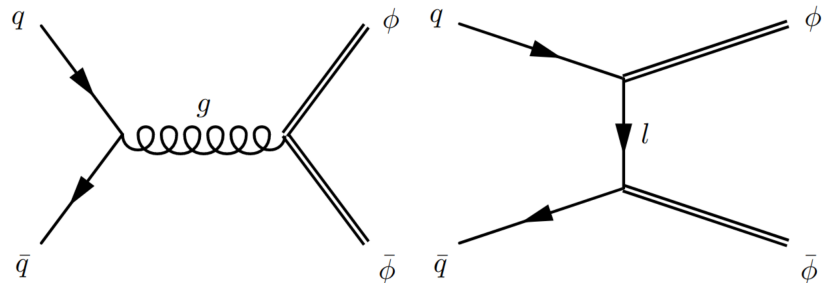
LQ considered by the minimal-Buchmüller-Rückl-Wyler model (cf. section 2.3.2) can result in various final states, which can be potentially detected by the ATLAS or CMS detector.



(a) Leptoquark pair production via gluon-fusion in the t-channel and the u-channel.



(b) Leptoquark pair production via gluon-fusion in the s-channel.



(c) Leptoquark pair production via quark-fusion in the s-channel and the t-channel.

Figure 2.2: Feynman diagrams of leptoquark pair production processes dominated by gluon-fusion (a), (b) and smaller contributions by quark-fusion (c) at proton-proton colliders like the LHC. [31]

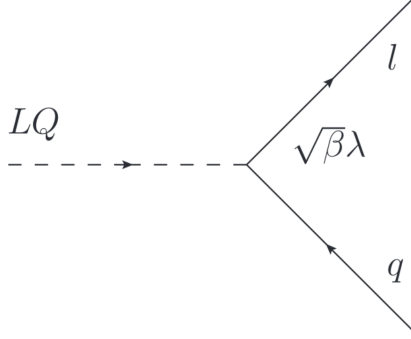


Figure 2.3: Feynman diagrams of a leptoquark decay into a lepton l and a quark q governed by Yukawa coupling $\lambda_{lq} = \sqrt{\beta}\lambda$. [34]

The data samples recorded by the ATLAS experiment in 2012 at a center of mass energy of $\sqrt{s} = 8$ TeV were searched for signal events of pair-produced LQs decaying to $LQ + LQ \rightarrow e^+ q + e^- \bar{q}$, $LQ + LQ \rightarrow \mu^+ q + \mu^- \bar{q}$, $LQ + LQ \rightarrow t\nu_\tau + q + \bar{t}\bar{\nu}_\tau$ and $LQ + LQ \rightarrow b\nu_\tau + q + \bar{b}\bar{\nu}_\tau$ at an integrated luminosity of 20.3 fb^{-1} . The search for first and second generation LQs was performed in the $e^+ q e^- \bar{q}$ and $\mu^+ q \mu^- \bar{q}$ channel. The integrated luminosity for the search of third generation LQs ($t\nu_\tau \bar{t}\bar{\nu}_\tau$ and $b\nu_\tau \bar{b}\bar{\nu}_\tau$) is 20.1 fb^{-1} . [35][§] For a branching ratio of the LQs of $\beta = 1.0$ exclusion limits were found for the first and second generation LQs. The exclusion limit for first generation LQ masses are $m_{LQ1} < 1050 \text{ GeV}$ and for second generation LQ masses are $m_{LQ2} < 1000 \text{ GeV}$ at a confidence limit (CL) of 95 %. For the third generation the mass exclusion limit at CL 95 % is $m_{LQ3} < 625 \text{ GeV}$ based on the $b\nu_\tau \bar{b}\bar{\nu}_\tau$ decay mode and $210 \text{ GeV} < m_{LQ3} < 640 \text{ GeV}$ based on the $t\nu_\tau \bar{t}\bar{\nu}_\tau$ decay mode. [35]

A more recent study by the ATLAS collaboration at $\sqrt{s} = 13$ TeV was published in reference [34] for first and second generation leptoquarks. The observed exclusion limits for the LQ mass at 95 % CL are 1100 GeV and 1050 GeV assuming a branching ratio of $\beta = 1.0$. The study has increased the sensitivity for the leptoquarks and agrees with the former study [35]. The exclusion limits are extended [34] compared to the previous study.

The CMS collaboration published a study for the search of third generation scalar leptoquarks decaying to a top quark and τ -lepton at a center of mass energy of 13 TeV. The corresponding integrated luminosity is 35.9 fb^{-1} . The results agree with the standard model expectation and no evidence for LQ pair production was

[§]The search for scalar leptoquarks at $\sqrt{s} = 7$ TeV at the ATLAS experiment is addressed by reference [36].

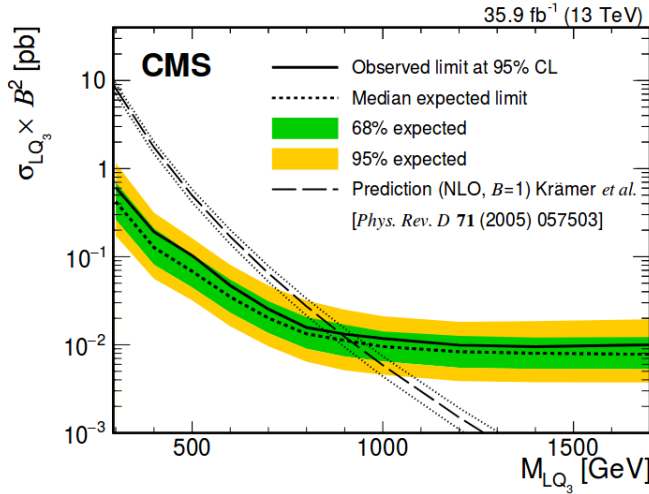


Figure 2.4: Upper limits at CL 95 % of the product of the cross section and β^2 depending on the leptoquark mass for the $t\tau^-\bar{t}\tau^+$ channel (third generation) at $\sqrt{s} = 13$ TeV [34].

found. The study excludes LQ with masses below 900 GeV at a branching fraction of $\beta = 1.0$ and at a CL of 95 %. Figure 2.4 shows upper limits at CL 95 % of the product of the cross section and β^2 depending on the leptoquark mass for the $t\tau^-\bar{t}\tau^+$ channel. These results are the most stringent limits to date for the production of third generation LQs decaying to top quark and τ -lepton. [37]

2.3.6 Starting point and research question for the analysis

This work is enclosed in the general research context briefly described in section 2.3.5 and makes a contribution to the search of pair-produced scalar LQs of type $S_{0,L}$ and $S_{1,L}$ (cf. table 2.3) decaying to $LQ + LQ \rightarrow t\tau^- + \bar{t}\tau^+$ at the ATLAS experiment. The common difficulty in searches for exotic particles is that in the measured datasets signal and background contributions appear as one entity. To reliably distinguish between signal and background events it would be ideally to break the data down into its single constituents. Of course this is not possible, but using Monte Carlo simulations provides up a chance for a better understanding of signal and background contributions in real data (see also section 4.6). Although this work does not presents a full search strategy for third generation leptoquarks it provides insight into τ reconstruction efficiencies and background studies for the search of LQ-signal signatures based on Monte Carlo samples (see section 6.2). Within the context of the $t\tau^- + \bar{t}\tau^+$ channel, efficiencies reflect the ability to successfully recon-

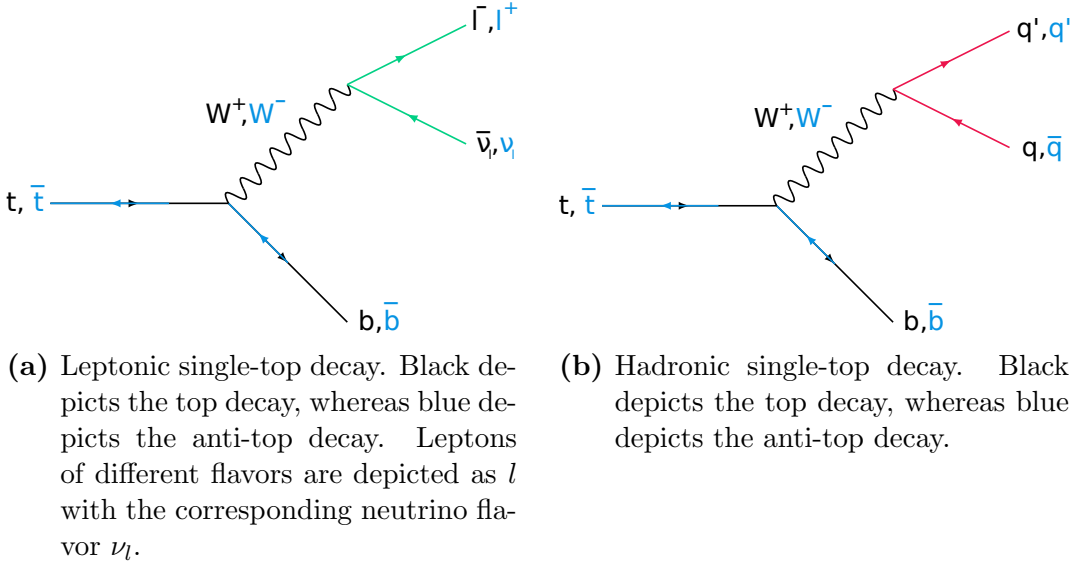


Figure 2.5: Leptonic (a) and hadronic (b) single-top decay.

struct a tau lepton in the detector. The thesis makes further contributions to fake rate estimations for objects that incorrectly mimic the signature of a tau lepton. It also presents kinematic variables (see section 6.3) within the event selection (see section 5.3) that are sensitive to the decay of third generation leptoquark pairs. By taking into account findings from the kinematic distributions, the efficiency and fake rate contributions, the discovery significances based on signal samples are calculated, which allows first optimization steps (see section 6.4). The used data sets are from the data taking periods 2015, 2016, 2017 and partly 2018 adding up to an integrated luminosity of 140 fb^{-1} .

The search for third generation LQ decaying to top quarks and τ -leptons is complex because of the multiple objects resulting from the subsequent decays of the heaviest quark and heaviest lepton. The top quark decays weakly into $t \rightarrow Wq$ with $q = b, s, d$. The main decay mode involves the bottom quark. The subsequent decay of the weak gauge boson W is either hadronically ($(66.5 \pm 1.4) \%$) or leptонically ($(34.0 \pm 1.0) \%$) [6]. This is shown in figure 2.5, where the black diagram paths indicates the top decay and the blue diagram path indicates the the anti-top decay. Leptons of different flavors are depicted as l with their corresponding neutrinos ν_l . This means that top-pairs can produce fully-leptonic decays following both the feynman diagram of figure 2.5a, fully-hadronic decays following both the feynman diagram of figure 2.5b and semi-leptonic decays, where one top decays leptонically and one hadronically. The overall percentage of the final state evolving from top pair pairs is shown in figure 2.6.

Tau leptons have various decay modes, which can be categorized by the num-

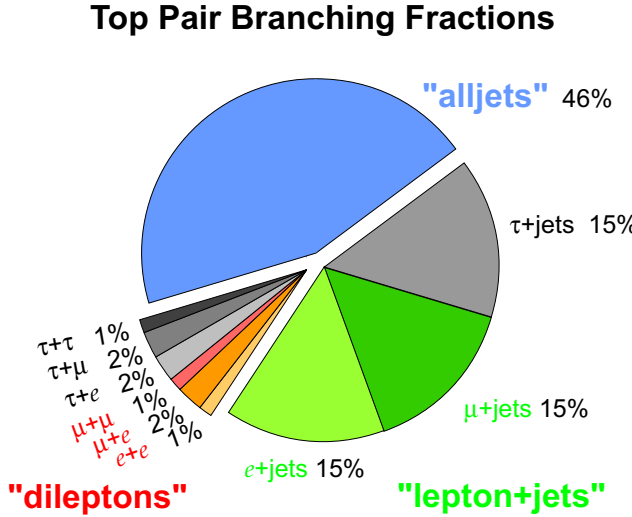


Figure 2.6: Branching fractions of top-pairs decaying fully-hadronically ('alljets'), fully-leptonically ('dileptons') and semi-leptonically ('lepton+jets') [38].

ber of charged particles involved in the decay. Main decay modes for taus include one charged particle ('1-prong') and three charged particles ('3-prong') in the decay. They are shown in table 2.4 for τ^- . Here h^\pm are charged pions π^\pm and Kaons K^\pm , ' neutrals' are photons γ or neutral pions π^0 . The decay modes of the τ^+ can be inferred by having corresponding decay products with opposite charges.

Signal and background studies with various objects in the final state depend crucially on the purity of the signatures left in the detector (cf. chapter 4) and how they are traced back to the potential LQ. For example electrons and muons can be reconstructed reliably from their corresponding detector signatures (see chapter 4). Therefore the dileptonic and semi-leptonic decay modes of the top quark-pair are good candidates to study the signal and background contributions for the search of LQ. A pair of LQ provide, in addition to the hadronic τ final states, two leptons from the top-pair decay or one lepton and one jet respectively. In the face of high contributions from underlying QCD events, resulting in jet objects, dileptonic and semi-leptonic modes are more accurately to reconstruct compared to the full hadronic decays with jets only in the final state. In order to optimize the LQ signal selection the reconstruction efficiencies and fake rates of hadronically decaying taus is investigated in the $t\tau^- + \bar{t}\tau^+$ channel.

mode		fraction Γ_i/Γ
1-prong decay		
Γ_1	$\text{particle}^- \geq 0 \text{ neutrals} \geq 0 K_L^0 \nu_\tau$	$(84.58 \pm 0.06) \%$
Γ_2	$\mu^- \bar{\nu}_\mu \nu_\tau$	$(17.39 \pm 0.04) \%$
Γ_3	$e^- \bar{\nu}_e \nu_\tau$	$(17.82 \pm 0.04) \%$
Γ_4	$h^- \nu_\tau$	$(11.51 \pm 0.05) \%$
Γ_5	$h^- \geq 1 \pi^0 \nu_\tau$ (excluding K^0)	$(36.51 \pm 0.09) \%$
Γ_6	$h^- \pi^0 \nu_\tau$	$(25.93 \pm 0.09) \%$
Γ_7	$h^- \geq 2 \pi^0 \nu_\tau$	$(10.81 \pm 0.09) \%$
Γ_8	$h^- 2 \pi^0 \nu_\tau$	$(9.48 \pm 0.10) \%$
3-prong decay		
Γ_9	$h^- h^- h^+ \geq 0 \text{ neutrals} \geq 0 K_L^0 \nu_\tau$	$(15.21 \pm 0.06) \%$
Γ_{10}	$h^- h^- h^+ \geq 0 \text{ neutrals} \nu_\tau$ (ex. $K_S^0 \rightarrow \pi^+ \pi^-$)	$(14.55 \pm 0.06) \%$
Γ_{11}	$h^- h^- h^+ \nu_\tau$	$(9.80 \pm 0.05) \%$
Γ_{12}	$\pi^- \pi^+ \pi^- \nu_\tau$	$(9.31 \pm 0.05) \%$
Γ_{13}	$h^- h^- h^+ \geq 1 \pi^0 \nu_\tau$ (excluding K^0)	$(5.09 \pm 0.05) \%$
Γ_{14}	$h^- h^- h^+ \pi^0 \nu_\tau$	$(4.76 \pm 0.05) \%$
Γ_{15}	$\pi^- \pi^+ \pi^- \pi^0 \nu_\tau$	$(4.57 \pm 0.05) \%$

Table 2.4: Main decay modes of τ^- including one charged particle ('1-prong') and three charged particles ('3-prong'). h^\pm are charged pions π^\pm and Kaons K^\pm , 'neutrals' are photons γ or neutral pions π^0 . The decay products of τ^+ have opposite charges correspondingly. [6]

3

Experimental setup for the search for scalar leptoquarks

For the search for scalar leptoquarks the ATLAS detector at the Large Hadron Collider (LHC) is used as experimental setup, which will be described within this chapter. The general setting of the proton-proton collider located at the CERN research center is the topic of section 3.1. The particle detection of the resulting collision events, taking place in the ATLAS detector with its different specialized components (section 3.2). Section 2.3.4 addresses the possible leptoquark pair production in proton-proton collisions.

3.1 The Large Hadron Collider accelerator complex

The CERN (Conseil Européen pour la Recherche Nucléaire) research center was founded in 1954 and is located near Geneva, Switzerland. It became a major European joint venture on elementary and nuclear particle physics. Currently, 22 member states are participating in that large-scale project. The scientific ambition is manifold and includes to probe the essential constituents of nature and the fundamental forces acting between them. [39]

In the accelerator complex protons reach energies of 6.5 TeV by going through different accelerator stages and are brought to collisions at defined interaction points in time intervals of 25 ns. Particle detectors, which are positioned at these interaction points, then register signatures of the resulting collision events and the analysis of newly created particles gives insight to the nature of elementary particle physics.[41] The LHC is designed as two-ring proton-proton collider. It is also possible to collide lead ions. These ion collisions are provided for the ALICE[42] experiment. However, the ATLAS and CMS experiment are in principle also capable of measuring lead collisions, but currently they are focused mainly on proton events. Figure 3.1 shows the different acceleration stages of the LHC among other CERN experiments.

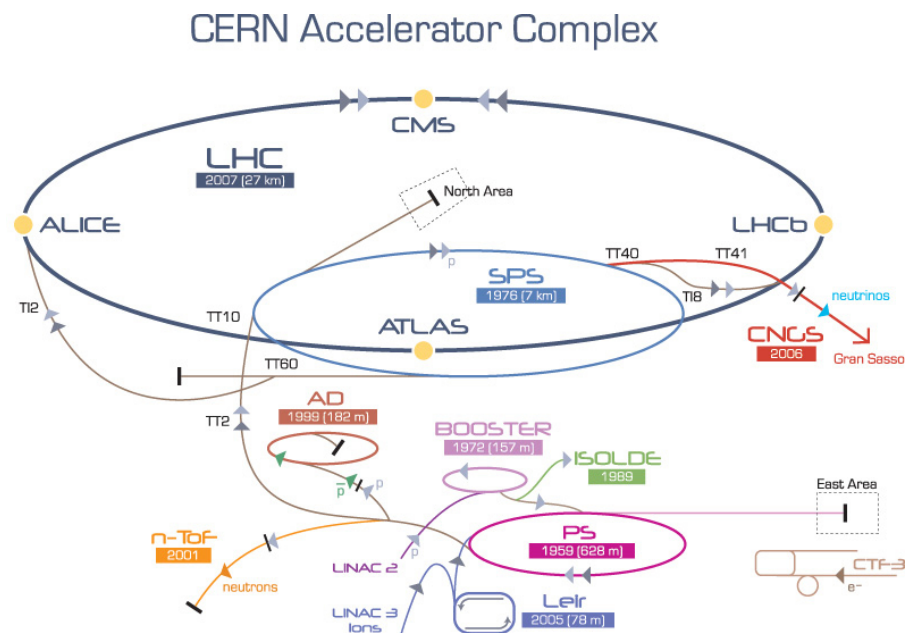


Figure 3.1: Schematic of the CERN accelerator complex with its different stages and few experiments like ATLAS located at the interaction points of the LHC. [40]

A hydrogen bottle is the starting point of the proton injection and acceleration. Fully ionized by an electron gun in chambers the protons are guided with electric fields towards the first acceleration stages. Radiofrequency (RF) cavities are responsible for the proton acceleration. Moreover the protons are accelerated in packages, known as bunches. [41][43] Starting from the injection, protons will gain a kinetic energy of 50 MeV in the linear accelerator LINAC2 and will be further transferred to the Proton Synchrotron Booster (1.4 GeV), the Proton Synchrotron (25 GeV), the Super Proton Synchrotron (450 GeV) and finally to the LHC ring with its 26.7 km circumference. [39] Dipole magnets are responsible for directing the protons through the stages and keep them on closed paths. Quadrupole magnets focus the beam to compensate the repulsive forces between the particles and to ensure small beam diameters at the interaction points for high collision rates. Conditions for a stable proton beam are diverse, including high vacua of 10^{-10} mbar to 10^{-11} mbar to avoid collisions with gas atoms and temperatures of 1.9 K for the superconducting NbTi-magnets of the accelerator. [41][43]

Different experiments like ALICE[42], LHCb[44] are located at the LHC due to the variety of research questions. The general-purpose detectors ATLAS and its counterpart CMS[45] are specialized to high luminosities*, exploiting the large range of physics opportunities made possible by the LHC. Main tasks of the ATLAS experiment are precision measurements of the SM (see chapter 2.1), a better understanding of Quantum Chromo Dynamics (QCD) and the search for supersymmetric models, and new physics, among others. With the LHC collision rate of 10^9 inelastic events per second, up to 23 simultaneous events per bunch-crossing at dominating high QCD cross sections require a powerful detector that is capable of recognizing the characteristic signatures. These circumstances are the reasons for the demands on the ATLAS detector, including fast electronic elements, high detector granularity, handling high particles fluxes and reducing overlapping events at a large acceptance and coverage region. [46]

3.2 The ATLAS detector at the LHC

One of the general purpose detectors for proton-proton collisions is the ATLAS detector. This 25 m tall detector is located at one interaction point of the LHC where bunches, consisting of approximately 10^{11} protons, collide at a rate of 40 MHz [46]. The number of particles encountered per time is given by [22]

$$\dot{N} = \mathcal{L}\sigma \quad (3.1)$$

*For the physical definition see eq. (3.2).

with the cross section σ for the present event and the instantaneous luminosity \mathcal{L} . The luminosity depends only on the characteristics of the collider and is often used as key parameter in collider physics [41].

$$\mathcal{L} = \frac{N_b n_b f_{\text{rev}} \gamma_r}{4\pi \epsilon_n \beta^*} F \quad (3.2)$$

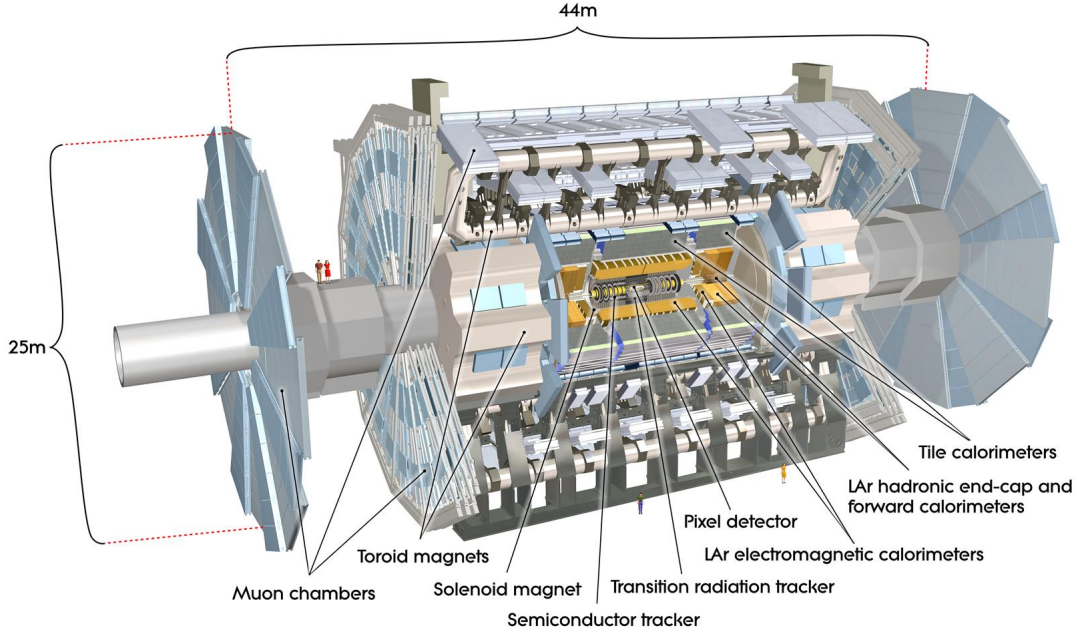
Where N_b is the number of particles per bunch, n_b the number of bunches per beam, f_{rev} the rotational frequency, γ_r the Lorentz factor, ϵ_n the normalized transverse beam emittance, β^* the betatron function at the collision point and F respects the geometric luminosity reduction factor due to the crossing angle at the collision point. The luminosity measured at the ATLAS interaction point exceeded the design luminosity of $\mathcal{L} = 2.05 \times 10^{34} \text{ cm}^{-2} \text{ s}^{-1}$ by a factor of 2.05 on the 2nd of November 2017, proving the great success of the LHC machine setup over the years [47].

To meet the requirements of a general-purpose detector, several considerations for the detector design were taken into account: On the one hand there is the demand to be sensitive to the great variety of particles governed by the fundamental forces (see chapter 2.1). On the other hand the yet unknown physics should be potentially covered as well by the ATLAS detector – all seen from the angle of performing precision measurements. The basic structure of ATLAS is shown in figure 3.2 with its different sub-detector systems together with the convention for the coordinate system. The nominal interaction point acts as origin of the coordinate system, where the z -axis follows the beam line counterclockwise. Perpendicular to the z -axis lies the transverse x - y -plane usually described through the azimuthal angle ϕ . The positive x -axis points towards the center of the LHC. The cylindric symmetry of the detector suggests a cylindric coordinate system with the angle θ starting from the beamline. [46] Since the polar angle is not a Lorentz invariant quantity, it is useful to describe the position in terms of rapidity [41] $w = \frac{1}{2} \ln \frac{E+p_z c}{E-p_z c}$ in that highly relativistic regime. In the limit of large momenta, i.e. $|\mathbf{p}|c \approx E$, the rapidity coincides with the pseudorapidity formulated as [48]

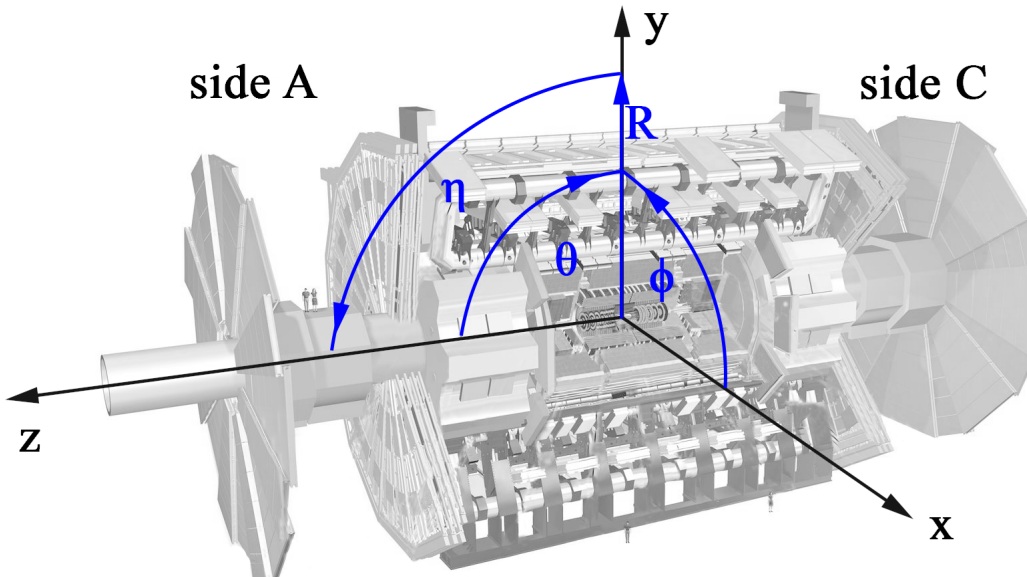
$$\eta = -\ln \tan \frac{\theta}{2}. \quad (3.3)$$

This variable only depends on the polar angle is therefore the adequate quantity in the context of collision experiments, where usually the angle θ from the beamline is measured. [48]

The collision products, originating from the interaction point at the center of the ATLAS detector, will propagate through the different layers of the detector's subsystems. The inner detector is responsible to track electrically charged particles.



- (a) The layered structure of the ATLAS detector at the LHC with its sub-systems inner detector, calorimeter, magnets and muon spectrometer [46].



- (b) The global ATLAS coordinate system formulated in cylindric coordinates with the z -axis parallel to the beam line and the transverse plane defined through azimuthal angle ϕ and pseudorapidity η . Based on [46].

Figure 3.2: Structure of the ATLAS detector and the coordinate system.

3 Experimental setup for the search for scalar leptoquarks

The magnetic fields for identifying the particles' electric charge and for momentum measurement is provided by the ATLAS magnet system. The next layer includes the calorimeter. The electromagnetic calorimeter measures mainly the energy deposit of electrons, positrons and photons and allows the distinction between them with the help of the track information given by the inner detector. Hadronic particles will deposit their energy in the hadronic calorimeter. The outermost layer consists of the muon system responsible for a second independent measurement of the muon and anti-muon tracks. [46]

The magnet system includes a superconducting solenoid with a field strength of 2 T surrounding the inner detector as well as three large superconducting toroid magnets composed in an eight-fold azimuthal symmetry around the calorimeter. The barrel toroid magnet delivers a field strength of 0.5 T and in the end-cap a field of 1 T is present. [46]

The inner detector is responsible for momentum measurements, vertex measurements and pattern recognition for the identification of electrically charged particles. This is achieved with a combination of semiconductor pixel and microstrip trackers (SCT). The Insertable B-Layer (IBL) is the innermost layer of the pixel detectors at a radius of 3.3 cm away from the beam line. Additional straw tube tracking detectors are sensitive to transition radiation (TRT) located in the outer part that are responsible for high vertex and momentum resolution. The $R - \phi$ segmented pixel detectors are of a size of $50 \times 400 \mu\text{m}^2$ and the SCTs with their 8 strip layers cover together a range of $|\eta| < 2.5$. Typically 36 hits per track are provided by the 4 mm straw tubes of the TRTs, which cover the range $|\eta| \leq 2.0$. [49][46]

Liquid argon electromagnetic sampling **calorimeters** with high granularity allow for an excellent energy measurement of electrons and photons. They have a total thickness of more than $22 X_0$ in the barrel region ($|\eta| < 1.475$) and more than $24 X_0$ in the end-cap region ($1.375 < |\eta| < 3.2$). For hadronic energy measurements a scintillator-tile calorimeter covering $|\eta| < 1.7$ is in operation. It is a sampling calorimeter and uses steel as absorber material and scintillating tiles as active material in conjunction with wavelength shifting fibres. Further LAr technology is used for hadronic particles in the outer pseudorapidity range up to $|\eta| = 3.2$. Here copper plates provide the absorber material. The forward calorimeters extend the coverage of hadronic and electromagnetic energy measurements to $|\eta| = 4.9$ and are $10 X_0$ deep. [46]

The **muon system** is located in the outer layer of the ATLAS detector and provides resolution for high energy muon tracks with three layered precision chambers up to the range of $|\eta| < 2.7$. This is possible because of the air-cored toroid magnet system including one barrel and two end-cap magnets generating strong bending power in a large volume and delivering a mostly perpendicular magnetic field with respect to the muon trajectories. The bending power $\int \vec{B} d\vec{l}$ along the track of the muon $d\vec{l}$ reaches from 1.5 T m to 5.5 T m in the range $|\eta| < 1.4$ (barrel) and up to 7.5 T m

(end-cap). The precision chambers are Monitored Drift Tubes (MDT) and in the larger pseudorapidity range Cathode Strip Chambers (CSC), which are multiwire proportional chambers. Due to the fact that the overall performance crucially depends on the alignment of the muon detectors with respect to each other and with respect to the inner detector, MDTs are equipped with a optical monitoring system with 12000 sensors. Resistive Plate Chambers (RPC) and Thin Gap Chambers (TGC) are the constituents of the muon trigger system. [46]

Due to technology and resource limitations the data recording rate has to be reduced from 40 MHz to 1 kHz. This poses high demands on an efficient **trigger system** which is organized in two levels. This is the level 1 hardware-based trigger and the software-based high level trigger (HLT). Level 1 uses only a subset of the total detector information making basic decisions to flag so called regions of interest within the detector's coordinate system. Searches include patterns for high transverse momenta of muon tracks, electrons and photons as well as jets or large missing energy balances. The output rate after this first selection accounts for 100 kHz. The HLT is responsible for selecting the level 1 triggered regions at full granularity and precision, reconstructing the complete events. This event filter is the final stage and achieves data reduction down to the final data-taking rate of 1 kHz, writing events of the size of approximately 2.4 GB s^{-1} to the disks. The HLT selection criteria are implemented using offline analysis procedures. [46][50]

Turning detector signatures into physical objects

All components of the detector system of ATLAS (see chapter 3.2) deliver electronic signals of the proton-proton collisions, which have to be reconstructed to physical objects for the analysis. This chapter describes the reconstruction of the physical objects like electrons, muons, jets and b-flavor jets and taus, which are relevant to the analysis in this thesis. Furthermore, the role of Monte Carlo simulations in the analysis is presented briefly.

4.1 Electron reconstruction at ATLAS

Electrons and positrons are stable and abundant final states of collision products. Therefore, relying on signatures of such particles in the detector is essential. Electrons and positrons* give rise to tracks in the inner detector and deposit their total energy in the electromagnetic calorimeter. The tracks and calorimeter signals are used for the electron reconstruction. [51]

For the reconstruction of electrons in the central region ($|\eta| < 2.47$) several steps are necessary. At first, with respect to the granularity of the calorimeter, it is searched for electron cluster seeds in the so called step of *seed-cluster reconstruction*. For more information on clusters see section 4.3. The efficiency of this search is 95 % to 99 % for transverse energies up to 7 GeV and > 15 GeV respectively. The *track reconstruction* is responsible for the pattern recognition in the inner detector taking into account the energy loss due to mainly bremsstrahlung in the detector material of up to 30 %. The track seed, consisting of at least three hits in different layers of the silicon detectors, is extended to a full track of at least seven hits and is extrapolated to the regions of interest at the electromagnetic calorimeter. This

*In this section, the term ‘positron’ is absorbed in the term ‘electron’.

is done by the ATLAS Global χ^2 Track Fitter [52]. Afterwards a loose matching of the tracks to the clusters in the electromagnetic calorimeter is done in the *electron specific track fit*. The final step, *electron candidate reconstruction*, is the selection of the final track candidate out of the different tracks with the best matching to the initial cluster seed. [51]

Both, the information of the track and the energy cluster, are used for the four-momentum calculation of the electrons. Algorithms for reconstructed electron identification are applied to distinguish signal-like or background-like electron candidates. For that the TRT likelihood method plays an important role, which uses the high-threshold hits of each TRT. Several discriminating variables are evaluated[†] for this likelihood method (LH). Based on the outcome, three quality categories for the electron identification are defined: *Loose* relies on information of the hadronic calorimeter and the first two layers of the electromagnetic calorimeter. *Medium* adds information from the TRTs, the transverse impact parameter and the third layer of the electromagnetic calorimeter, whereas the *Tight* operating point additionally considers track-cluster matching variables like the ratio of the cluster energy over the track momentum. [51]

For a well reconstructed electron additional requirements on the isolation of the cluster and the track need to be met. In this thesis the definition of the operating point *Gradient* is relevant. The efficiency depends linearly on the transverse energy E_T . For Gradient the isolation efficiency used in the operating point optimization is $0.1143\% \text{ GeV}^{-1} \cdot E_T + 92.14\%$ for the calorimeter cluster and the track. [51]

The high level electron trigger has a transverse energy threshold of at least 24 GeV and requires at least a medium quality electron based on the likelihood categories described in section 4.1 (`e24_lhmedium`). This high level trigger (HLT) is seeded from the electromagnetic calorimeter of the level 1 trigger system with a threshold of at least $E_T < 20 \text{ GeV}$ (L1EM20VH). Additionally a energy dependent veto against energy deposits in the hadronic calorimeter behind the electromagnetic cluster is implemented. Thus it acts as hadronic veto (denoted with ‘H’). Furthermore the transverse energy threshold depends slightly on the pseudorapidity to compensate for energy losses in the material directly in front of the electromagnetic calorimeter (denoted with ‘V’). The next step of a tighter trigger selection includes a transverse energy threshold of $E_T > 60 \text{ GeV}$ and requires a medium quality electron (`e60_lhmedium`). Adapted for high energy electrons the trigger `e120_lhloose` provides electrons with transverse energies of at least 120 GeV by requiring at the same time the loose electron working point. [53] The above electron trigger menu is valid for data taken in 2015. For the data-taking periods in 2016-2018 the following changes are applied:

HLT thresholds are set to 26 GeV with the tight quality requirement (`e26_lhtight`) and a variable cone size isolation (`ivarloose`), which uses the criteria that the sum

[†]For further details see [51]

of the track momentum must not exceed 10 % of the electron’s transverse energy within a cone of $\Delta R = \sqrt{\Delta\eta^2 + \Delta\phi^2} < 0.2$ [54][55]. Additional to that no transverse impact parameter cut is applied (`nod0`) [54]. The complementary trigger for the high transverse energy regime is increased to 140 GeV [53].

4.2 Muon reconstruction at ATLAS

Muons are good tracers of particles with shorter lifetimes and thus should be reconstructed as an important information carrier of the particle collisions. Muons* are reconstructed independently in the inner detector and the muon spectrometer and the resulting combination of the two gives the full muon track. [56]

The first reconstruction step is again pattern recognition for seeds in the silicon layers from the inside towards the outside of the inner detector. Seeds are formed out of three space points. The space points are provided by the pixel detectors with their local two-dimensional space points and from the combination of a pair of SCTs. The default setting of the seeding algorithm allows three combinations for space points: all space points within the pixel detector, all within the SCTs or two within the pixel detector and one within the SCT. [57]

The muon reconstruction in the muon spectrometer is initiated by the search for hit patterns in the muon chambers to form segments. Muon track candidates are created by fitting the segments from different layers, which is done by a combinatorial search. Selection criteria include hit multiplicity and fit quality to find the optimal track. The hits associated to each track candidate, after applying an overlap removal algorithm, are fitted using a global χ^2 fit. [56]

Different types of reconstructed muons are distinguished, depending on which information of the possible muon candidate is available in the inner detector, the calorimeter and the muon spectrometer. After a first signature combination of the involved sub-detector signatures, the energy loss of the muon traveling through the calorimeters and the detector material is included in a refit. A *combined muon* is reconstructed from the independent inner detector and muon spectrometer measurement in a global refit, if both sub-detector components have registered a muon signature. *Segment-tagged muons* are extrapolated from the inner detector muon track to at least one local segment of the muon spectrometer. If the track of the inner detector can be matched to energy deposits in the calorimeter, the reconstructed muon is called *calorimeter-tagged* muon. Muons reconstructed only on the basis of the muon spectrometer are extrapolated back to the interaction point and therefore are called *extrapolated muons*.[56]

*In this section, the term ‘anti-muon’ is absorbed in the term ‘muon’.

Quality requirements on the track suppress background contributions and guarantee a robust momentum measurement by including discriminating variables like the χ^2 of the combined track. This categorization finalizes the muon identification process. For the category *Loose muons* all above listed muon types are used. The category *medium muons* minimizes the systematic uncertainties and is based only on combined muons and extrapolated muons. *Tight muons* only uses the combined muon type and is optimized for maximum purity at the cost of some efficiency. The *high- p_T muons* are designed for a maximization of the momentum resolution for tracks above 100 GeV. [56]

The relevant isolation requirement used in this thesis for muons is the so called *Gradient* isolation, which includes track-based and calorimeter-based discriminating variables. In this case it is the sum of transverse momenta of the tracks in a cone around the muon with $\Delta R = \sqrt{\Delta\eta^2 + \Delta\phi^2} < 0.3$, excluding the muon track itself. The calorimeter condition is based on the sum of transverse energies of the topological clusters around the muon in a cone of $\Delta R < 0.2$. [56][58]

Trigger decisions for muons are based on the MS and the quality of the match that combines the track measurement of the MS and the ID. The requirement on the transverse momentum of the combined muon is at least 20 GeV with an additional loose isolation (`mu20_iloose`). The loose isolation means that the scalar sum of the track p_T values does not exceed 12 % of the muon's transverse momentum within a cone of $\Delta R < 0.2$. This HLT is based on the decisions of the trigger level 1 seed, which selects muons with a transverse momentum of at least 15 GeV (L1MU15). The HLT trigger `mu50` has a threshold of $p_T < 50$ GeV and complements the trigger's high momentum regime without isolation conditions. The above muon trigger menu is based on the data taking periods in 2015 [53]. Changes to the data selection of the periods of the year 2016-2018 are as follows:

The HLT transverse momentum requirement is changed to at least > 26 GeV and the isolation requirement is changed in such a way that the scalar sum of the track momentum must not exceed 7 % of the muon's transverse momentum within a cone of $\Delta R < 0.3$ (`e26_ivarmedium`) [59].

4.3 Jet reconstruction at ATLAS

Note that jets are not physical objects in the sense of elementary particles, but denote collimated streams of colored final states. Due to confinement (cf. chapter 2.1) colored fragments will always result in jet signatures. [3]

For the reconstruction of hadronic parts of final states like isolated hadrons, jets (see also section 4.4) and hadronically decaying taus (see also section 4.5), the ATLAS experiment employs clusters of topologically connected calorimeter cell sig-

nals (topo-clusters). The topo-cluster algorithm analyzes the spatial distribution of the cell signals to reconstruct the energy and direction of the incoming particle. [60]

The segmented lateral readout of the high granularity calorimeter allows the distinction between signals from particle showers and background events with the aid of the cell signal significance $\zeta_{\text{cell}}^{\text{EM}}$. [60] Seeds are defined by cells, where the absolute energy $|E|$ exceeds the noise level by a factor of four standard deviations. The topo-clusters are expanded by iteratively adding all neighbor cells with energies two standard deviations above the noise level. [61]

For this thesis the relevant clustering algorithm is the anti- k_t algorithm. The algorithm is based on the following definitions [62]:

$$d_{ij} = \min(k_{ti}^{-2}, k_{tj}^{-2}) \frac{\Delta_{ij}^2}{R^2}, \quad (4.1)$$

$$d_{iB} = k_{ti}^{-2}, \quad (4.2)$$

where d_{ij} is the distance between the objects i and j and d_{iB} the distance between i and the beam B in the transverse plane. k_t denotes the transverse momentum and $\Delta_{ij}^2 = (\eta_i - \eta_j)^2 + (\phi_i - \phi_j)^2$ denotes the cone between i and j . The radius parameter R scales the distance d_{ij} with respect to d_{iB} that any final pair of jets a and b is at least separated by $\Delta_{ab}^2 = R^2$. The final clustered jet is obtained by the search of the minimum in distances d_{iB} and d_{ij} . If the minimum is d_{ij} , then the sum of the four-momentum of object i and j is calculated and is treated as a new object. Again all distances between the objects are re-calculated until d_{iB} is a minimum. This means, object i is the final jet. The anti- k_t algorithm is a stable jet reconstruction algorithm and is not prone to fluctuations because of adding low k_t -objects. [62]

4.4 b-jet reconstruction at ATLAS

The third generation quarks, i.e. top (t) and bottom (b), play a crucial role in the SM and its various extension possibilities like the Leptoquark Model due to their large masses [63]. Therefore, it is essential to identify hadrons containing b quarks and separating them from light-flavor quarks at hadron collider detectors like ATLAS. This task is commonly referred to as b-tagging and can be seen as a classification problem with the goal to assign correct jet flavors. To this end the particle tracks in the inner detector and the jet reconstruction of clusters in the electromagnetic and hadronic calorimeter are discriminating objects. [64]

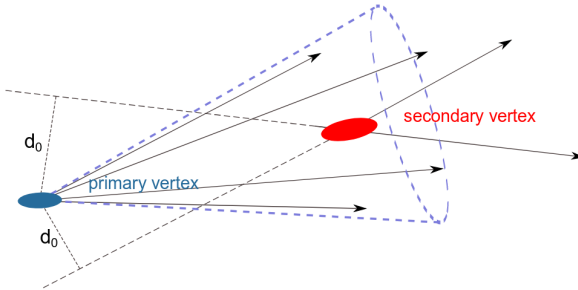
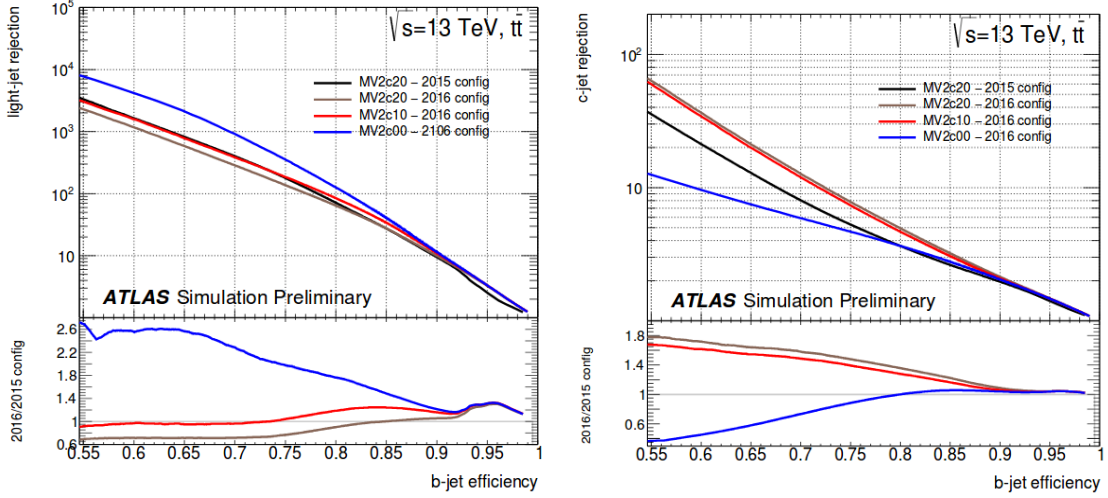


Figure 4.1: Signature of a b-jet with the primary and secondary vertex created relevant for b-tagging. d_0 is the impact parameter. [63]

The long lifetime of B hadrons of ~ 1.6 ps allows them to travel a few millimeters in the detector. The subsequent decay of those heavy particles within a secondary vertex produces tracks with a comparably large impact parameter d_0 that is the shortest distance of the particle track from the primary vertex (see figure 4.1). This signature and the deduced impact parameter significance $S(d_0) = \frac{d_0}{\sigma(d_0)}$, where $\sigma(d_0)$ is the uncertainty of the impact parameter, are used by the b-tagging algorithms including five low-level and two high-level taggers. [63] The b-tagging algorithms rely on multivariate combinations of the information and process them to calculate a discriminant value for each jet. Thresholds on these values define the working point to provide efficient identification of b-jets. For better information processing of the combinations of large input parameters neural network models can be used. [65] One example for a b-tagging algorithm is the MV2 tagger which uses 24 input variables of the low-level taggers together with kinematic properties*. [64] It uses a boosted decision tree (BDT) to discriminate b-jets from light-jets and c-jets. [66] The light-flavor and c-jet rejection as a function of b-jet efficiency for MV2c10 (red line) is shown in figure 4.2. The description ‘c10’ indicates the fraction of c-jet composition of the training background sample, e.g. for MV2c10 the c-jet to light-jet composition is 10 %/90 %. Three other tagger configurations are shown in comparison as well as their ratio to MV2c10. Following the MV2c10 efficiency curve different working points can be defined. The relevant working point for the physical object selection in this work is 77 % (cf. chapter 5.2). The c-jet rejection rate for this working point is 6, for light-jet rejection 134 and for τ -rejection 22 extracted from $t\bar{t}$ events. [67]

*For further details on MV2 see [66]



(a) Light-jet rejection versus b-jet efficiency for the MV2c10 tagger (red) in comparison to previous configurations evaluated on $t\bar{t}$ events. The ratio is evaluated with respect to MV2c10. [67]

(b) c-jet rejection versus b-jet efficiency for the MV2c10 tagger (red) in comparison to previous configurations evaluated on $t\bar{t}$ events. The ratio is evaluated with respect to MV2c10. [67]

Figure 4.2: Light-flavor and c-jet rejection versus b-jet efficiency for the MV2c10 tagger. [67]

4.5 Tau reconstruction at ATLAS

Final states with tau leptons*, decaying hadronically, play an important role for the physics at the ATLAS experiment. Five hadronic decay modes cover over 90 % of the overall hadronic modes, which results in one (1-prong) or three (3-prong) charged hadrons (h^\pm), up to two neutral pions (π^0) and a tau neutrino ν_τ . [68] For the reconstruction of hadronic taus $\tau_{\text{had-vis}}$ at the ATLAS detector, the anti- k_t algorithm (see eq. (4.2)) for jet formation is used (see section 4.3) with a distance parameter of $R = 0.4$. The requirements for the transverse momentum is $p_T > 10 \text{ GeV}$ and for the pseudorapidity is $|\eta| < 2.5$. The hadronic identification of the tau relies on topo-clusters in the last layer of the electromagnetic calorimeter and the hadronic calorimeter. The additional track selection requires at least two associated hits in the pixel detector/IBL in the $\tau_{\text{had-vis}}$ direction and at least seven hits in total in the pixel detector and the SCTs. Also requirements on the distance of closest approach are set to $|d_0| < 1.0 \text{ mm}$ in the transverse plane and to $|\Delta z_0 \sin \theta| < 1.5 \text{ mm}$.[69]

Due to the fact that the reconstruction of tau candidates provides very little rejection

*In this section, the ‘term anti-tau’ is absorbed in the term ‘tau’.

against jet background a detailed set of discriminating variables[†] are introduced. Tau identification relies on separate boosted decision trees (BDT) for each prong case. The working points for that are labeled *loose*, *medium* and *tight* corresponding to different signal efficiency values. In case of 1-prong they are, respectively, 0.6, 0.55 and 0.45 for loose, medium and tight. The working points for 3-prong decays correspond to 0.5, 0.4, 0.3. [69]

To ensure that electrons will be not misinterpreted as 1-prong tau decays an additional BDT is implemented as a tau-electron veto. It has the same classification of *loose*, *medium* and *tight*, but with signal efficiencies of 0.95, 0.85 and 0.75 respectively. [70]

4.6 Monte Carlo simulations

A steady comparison and adaption of theory and experiment is crucial to be able to draw physically reliable conclusions. This fact holds true for high energy particle collision experiments, like the LHC. Therefore predictions for collision events, the creation of new particles, the understanding of decays and fragmentation of these generated particles, modeling the underlying event, predictions to the subsequent hadronisation of quarks, the calculation of interactions with the detector and predictions of final states are necessary for the search of new physics. These scenarios are an extremely challenging endeavor. Typically hundreds of particles of different kinds are involved and their energy and momentum spectra are widely distributed over different orders of magnitude. One important cornerstone to cope with the above mentioned challenges are Monte Carlo (MC) simulations. [71]

MC simulations are based on an algorithm relying on sequences of pseudo random numbers. Effectively it is a method to numerically compute multidimensional integrals over a complex region as it is often the case for matrix elements in perturbation theory. [72] The MC chain for the ATLAS detector consists of three main steps. This includes the generation of MC events with event generators and the subsequent simulation of fragmentation and showering processes in the first step. The second step is the simulation of the detector and the propagation of the particles through it with the associated interactions and, as third step, the digitization of energy deposits in the detector's sensitive areas. This digitization step involves the simulation of the resulting signals in the readout system for comparison with real data. The detailed implemented simulation of the detector and the particles interaction with it is done with GEANT4[73], which additionally considers realistic detector conditions and misalignments as well as the detector response to be as realistic as

[†]They can be found in [69].

possible. This fact enhances the digital copy to furthermore test the effectiveness of proposed search strategies for specific signatures like the ones created from exotic particles. [74]

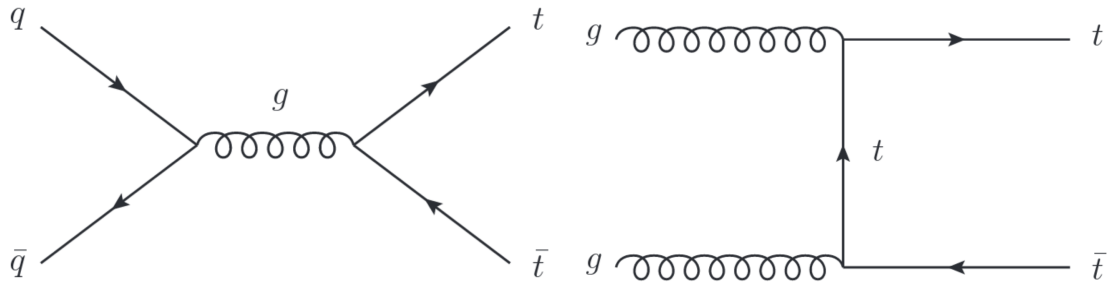
Analysis

Before investigating the research question formulated in section 2.3.6, the framework principles have to be defined. The MC samples and data samples, which are taken into account, are listed in detail in section 5.1. The physical object definition and the event selection for the performed analysis are presented in section 5.2 and 5.3.

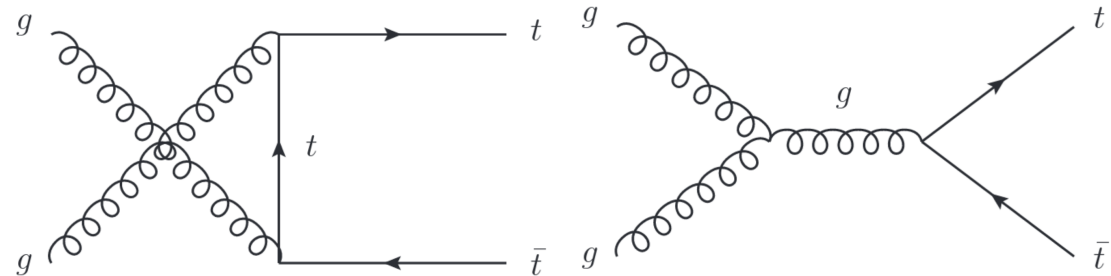
5.1 Datasets and Monte Carlo samples

The motivation is to estimate tau efficiencies for the search for third generation leptoquarks in the $t\tau^- + \bar{t}\tau^+$ channel. To draw convincing conclusions from the efficiency study, a good estimation of the standard model background events has to be chosen. The choice of background samples involves the following considerations: Dominant background processes, contaminating the potential LQ signal, originate from QCD events producing top-quark pairs and top-pair production in association with Higgs, where Higgs decays into tau leptons.

The differential cross section for top-quark pair generation at $\sqrt{s} = 13$ TeV is (829 ± 189) pb [75] including the statistical and the systematic uncertainty as well as the uncertainty from the luminosity measurement. Due to the nature of a proton-proton collider mainly gluon fusion (90 % [6]) is responsible for the top-quark pair production at the LHC. Also quark fusion can lead to $t\bar{t}$ states. The corresponding Feynman diagrams involved in the pair production are shown in figure 5.1. Because of its high production cross section and the lack of naturally existing taus, the $t\bar{t}$ sample is the ideal candidate to study jets and especially b-jets that fake as a hadronic tau. The total cross section measured for Higgs production is (12^{+25}_{-16}) pb [77]. The dominant Higgs production mechanisms of leading order at hadron colliders are gluon fusion, vector boson fusion, Higgs-strahlung or the associated production with a pair of top (bottom) quarks [6]. The relevant background SM process for the search of LQs is the associated Higgs production with a top pair, which can



(a) Quark fusion process generating a top-
quark pair in the s-channel [76]. (b) Gluon fusion process generating a top-
quark pair in the t-channel [76].



(c) Gluon fusion process generating a top-
quark pair in the u-channel [76]. (d) Gluon fusion process generating a top-
quark pair in the s-channel [76].

Figure 5.1: Feynman diagrams showing the dominant top-pair production at the LHC
including quark fusion (a) and gluon fusion (b)-(d) [76].

mimic the $t\tau^- + \bar{t}\tau^+$ state. The $t\bar{t}H$ cross section is (0.51 ± 0.06) pb. The corresponding Feynman diagram for $t\bar{t}H$ production is depicted in figure 5.2. The used $t\bar{t}H$ sample (cf. section 5.1) acts as an inclusive sample, which allows all possible Higgs decays. The Higgs coupling strength is proportional to the particle's mass and therefore the direct decay of the Higgs boson into a tau-pair is possible, as it involves the heaviest lepton (cf. 2.2). Together with the decay $H \rightarrow b\bar{b}$ the mode $H \rightarrow \tau^-\tau^+$ is the dominant process below the threshold of 160.8 GeV and 182.4 GeV that is the on-shell $H^0 \rightarrow W^-W^+$ and $H^0 \rightarrow Z^0Z^0$ production [6]. On-shell means that both vector bosons are produced with their likeliest mass rather than producing one vector boson of the pair as a virtual particle. From the point of view of the Higgs boson's coupling to large masses in principle $H \rightarrow t\bar{t}$ is also a possible decay mode. But the di-top mass exceeds the Higgs mass by a factor of roughly three times, which suppresses that decay due to the fact that the top-pair can exist only virtually. The above mentioned aspects make the $t\bar{t}H$ sample a good candidate

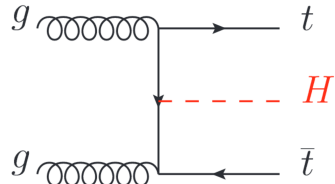


Figure 5.2: Feynman diagram in leading order for the top-quark pair associated Higgs production [6].

to study faked taus from jets with the additional condition that also real taus are naturally present compared to the top-pair production. Furthermore efficiencies for different tau selections can be studied as well in this events as they occur as signal signatures. Findings in the background processes then can be compared to the LQ signal samples (see section 6.2.2).

Together these two background samples cover most of the contamination of the $t\tau^- + \bar{t}\tau^+$ for the LQ search.

The MC samples in the analysis are used to investigate the signal and background composition and to estimate fake rates related to tau reconstruction of LQs in the $t\tau^- + \bar{t}\tau^+$ channel. The analysis uses two types of MC samples. One category includes the LQ signal following the decays after the mBRW model (cf. section 2.3.2). These signal samples were produced with the event generator MADGRAPH5_aMCNLO (v2.6.0) [78] with two different mass points of the LQ of $m_{LQ} = 500$ GeV and $m_{LQ} = 1$ TeV and with a production cross section of 271 fb and 3 fb respectively. The top pair is allowed to decay either fully leptonically or semi-leptonically in the LQ sample (cf. section 2.3.6). The parton showering and fragmentation as well as the underlying

5 Analysis

event generation were done with PYTHIA8.2 [79] with the particle distribution function (PDF) sets NNPDF3.0NLO [80] and the A14 [81] tunes at next-to-leading order (NLO) in matrix calculation.

The other category of simulations includes main background contributions of standard model processes as motivated above. That is background from $t\bar{t}$ pairs and inclusive $t\bar{t}H$ decay processes. The $t\bar{t}$ samples are generated with POWHEG-Box [82] and allow the $t\bar{t}$ pair to decay fully leptonically. Showering, fragmentation and the underlying event generation are simulated with the generator PYTHIA8.2 at NLO with the PDF set of NNPDF2.3NLO and the parameter set of A14. The h_{damp} parameter was set to 258.75 GeV, which is a resummation damping factor and regulates the highest transverse momentum of the first additional parton radiation beyond the Born level [83][84].

The $t\bar{t}H$ sample is generated with POWHEG-Box. Like for the $t\bar{t}$ samples, the

data-taking year	integrated luminosity
2018	60 fb^{-1}
2017	44 fb^{-1}
2016	33 fb^{-1}
2015	3 fb^{-1}
total	140 fb^{-1}

Table 5.1: Integrated luminosity for the data-taking periods 2015, 2016, 2017 and 2018.

event generator PYTHIA8.2 at NLO with the PDF set of NNPDF2.3NLO and the parameter set of A14 was used to simulate the showering, fragmentation and underlying event. The mass of the Higgs boson is set to 125 GeV and the resummation parameter was set to 325.5 GeV.

For all samples the EVTGEN (v1.6.0) [85] program was used for the decay of the bottom and charm hadrons produced by the top-quark decay.

Data sets of the data-taking periods 2015, 2016, 2017 and 2018, which were produced at a center of mass energy of $\sqrt{s} = 13 \text{ TeV}$, are studied and compared to the MC predictions. Table 5.1 shows the integrated luminosity of the different years and the total integrated luminosity of 140 fb^{-1} used in the analysis. Because of the fact that for this study no systematic uncertainties are considered, the luminosity values are rounded to the next whole number. Their uncertainty contributions of usually few percent are small compared to uncertainties from systematics.

5.2 Physical object selection

The physical object selection for electrons, muons, hadronic taus, jets and b-jets in the analysis is described in this section. For the general reconstruction concepts of physical objects see chapter 4.

The ATLAS software framework for event generation, simulation, reconstruction and derivation production (cf. also section 4.6) is Athena [86]. The standard package for physical object reconstruction used in this analysis is AnalysisTop. It is derived from the general software chain of AthAnalysisBase specifically adapted for the needs of the top-quark analysis group. The C++ framework ROOT is used as data analysis tool. For this work a package based on AnalysisTop of release 21.2.56 (build on November 29, 2018) was used.

Electrons

Electrons have to fulfill the tight quality requirement and need to have at least a transverse momentum of $p_T > 27 \text{ GeV}$ and lie within the pseudorapidity range of $|\eta| < 2.5$. In order to get a clean signal from a leptonic decaying top quark, the electrons have to meet the p_T dependent isolation requirements. For the electron trigger requirements see the paragraph ‘Lepton trigger’ below.

Muons

Muons have to meet the medium quality requirement and need to have a transverse momentum of $p_T > 27 \text{ GeV}$. The selected muons are reconstructed as a combined muon within a pseudorapidity region of $|\eta| < 2.5$. Analogous to the electron selection for a clean lepton signal, the muon has to further fulfill the p_T dependent isolation requirements. For the muon trigger requirements see the paragraph ‘Lepton trigger’ below.

Taus

Taus selected for this analysis need to have a transverse momentum of at least $p_T > 25 \text{ GeV}$ and must lie within the pseudorapidity range of $|\eta| < 2.5$. Additional to that the taus have to decay hadronically. Following their basic reconstruction

5 Analysis

procedure, taus have to meet the conditions of the loose working point (see section 4.5). To avoid misinterpretations of electrons as taus, the corresponding working point is set to loose.

Jets

Jets are reconstructed with the anti- k_T algorithm and need to have a transverse momentum of at least $p_T > 25 \text{ GeV}$.

b-jets

For the b-jet selection the b-tagger MV2c10 is used with a working point of 77% b-tagging efficiency.

Lepton trigger

The trigger requirements relevant for the analysis on electrons and muons are described here and are categorized each after the corresponding data-taking period.

Electrons are required to pass the ‘OR’ condition of the single electron triggers. This means that for an electron at least one of the triggers presented in table 5.2 had indicated an electron signature for the specific data-taking period in the detector.

data-taking year	‘OR’ required trigger	important parameter
2018, 2017, 2016	e26_lhtight_nod0_ivarloose	$p_T > 26 \text{ GeV}$, tight working point
	or e60_lhmedium_nod0	$p_T > 60 \text{ GeV}$, medium working point
	or e140_lhloose_nod0	$p_T > 140 \text{ GeV}$, loose working point
2015	e24_lhmedium_L1EM20VH	$p_T > 24 \text{ GeV}$, medium working point
	or e60_lhmedium	$p_T > 60 \text{ GeV}$, medium working point
	or e120_lhloose	$p_T > 120 \text{ GeV}$, loose working point

Table 5.2: List of single electron triggers.

The same strategy as it is used for electrons is valid for muons. Muons are required to pass the ‘OR’ condition of the single muon triggers. This means that

for an muon at least one of the triggers presented in table 5.3 had indicated a muon signature for the specific data-taking period in the detector.

data-taking year	‘OR’ required trigger	important parameter
2018, 2017, 2016	mu26_ivarmedium or mu50	$p_T > 26 \text{ GeV}$, medium working point $p_T > 50 \text{ GeV}$
	mu20_iloose_L1MU15	$p_T > 26 \text{ GeV}$, loose working point
2015		

Table 5.3: List of single muon triggers.

For more detailed information about the trigger requirements and their explanation see section 4.1 and 4.2.

Overlap removal

To avoid misinterpretations an overlap removal between different objects acts like a veto and is applied for the event reconstruction. The overlap is determined by thresholds in the separation variable $\Delta R = \sqrt{\Delta\eta^2 + \Delta\phi^2}$. The following overlap removals are applied for objects like electrons e , muons μ , tau leptons τ and jets j :

- electron removal if $\Delta R(e, j) < 0.4$
- muon removal if $\Delta R(\mu, j) < 0.4$
- jet removal if $\Delta R(j, e) < 0.2$
- tau removal if $\Delta R(\tau, l) < 0.2$ with $l = e, \mu$

5.3 Event selection

The signal and background studies for the $t\tau^- + \bar{t}\tau^+$ channel involves the event selection shown in figure 5.3.

The selection includes one electron and one muon of opposite electrical charge and a transverse momentum of at least $p_T > 27 \text{ GeV}$. This di-lepton selection covers the leptonic decay of the top-pair mediated by the W^- boson in case of the anti-top quark and mediated by the W^+ in case of the top quark. Due to conservation of the electric charge the resulting leptons of the subsequent decay of the W^\pm boson



Figure 5.3: Overview of the event selection involved for the signal and background studies in the $t\tau^- + \bar{t}\tau^+$ channel.

is of opposite sign. In addition to that at least two jets are selected because the weak top-pair decay produces a bottom-pair (cf. figure 2.5), which will result in a jet. At least two of the above selected jets have to be b-tagged or at least one of the above jets have to be b-tagged. To cover the full $t\tau^- + \bar{t}\tau^+$ channel, an additional selection is made to select at least either one or two tau leptons for each cases of b-jet selection. The samples include these categories of one b-tagged jet, two b-tagged jets, one tau or two taus and the corresponding distributions as separate categories.

6

Results

6.1 Number of event candidates

The observed and predicted number of event candidates for the event selection described in section 5.3 is summarized in this chapter.

The event yield table 6.1 includes all the main background contributions from $t\bar{t}$ and $t\bar{t}H$ processes as well as the LQ signal samples generated with two different mass points compared to the number of event candidates from data. The error consists of the statistical uncertainty only. The differentiation of the event number categories follow the event selection described in section 5.3. Its main categories include the selection of either at least one b-jet or at least two b-jets. The decay channel of the LQ involves a pair of b-quarks originating from the subsequent top-pair decay mediated by the weak interaction (cf. section 2.3.6). After the two b-jet selection the sample is dominated by contributions from standard model $t\bar{t}$ productions. Selecting only one b-jet will be useful for a full search strategy for scalar LQs. Due to the leptoquarks' high masses of 500 GeV and 1 TeV and experimental exclusion limits as well as theoretically considerations, the assumed production cross section at the LHC is small compared to abundant QCD processes of the SM*. Thus the looser selection of at least one b-jet and the resulting higher event yield gives room for tighter cuts on kinematic variables to optimize the signal and at the same time loses almost nothing in background rejection.

The additional selection of at least either one or at least two tau leptons impose an additional reduction on the event yield for both b-jet selections. The difference between the background simulations is that selecting ≥ 1 b-jet + $\geq 1 \tau$ additionally results in a strong reduction of the events without any tau lepton selection down to $(0.50 \pm 0.75)\%$ in case of the $t\bar{t}$ sample, whereas the amount in case of the $t\bar{t}H$ sample is reduced to $(5.4 \pm 2.0)\%$. The expectation is that the events surviving the tau selection contributed from the $t\bar{t}$ sample are mainly due to faked taus. No real τ lepton is expected here. In contrast, some real τ contributions from the Higgs

*For a cross section comparison see 5.1, where the different samples are discussed.

channel	event selection					
	≥ 1 b-jet	≥ 1 b-jet + $\geq 1\tau$	≥ 1 b-jet + $\geq 2\tau$	≥ 2 b-jet	≥ 2 b-jet + $\geq 1\tau$	≥ 2 b-jet + $\geq 2\tau$
$t\bar{t}$	$555\,369 \pm 303$	2793 ± 21	7.5 ± 1.1	$270\,799 \pm 210$	765 ± 11	2.99 ± 0.69
$t\bar{t}H$	517.4 ± 2.7	28.02 ± 0.55	1.554 ± 0.070	338.1 ± 1.6	14.24 ± 0.37	0.735 ± 0.043
total	$555\,886 \pm 303$	2821 ± 21	9.0 ± 1.1	$271\,137 \pm 210$	779 ± 11	3.72 ± 0.69
$LQ_{500\,\text{GeV}}$	1304 ± 40	598 ± 27	96 ± 10	650 ± 28	287 ± 19	45.9 ± 6.7
$LQ_{1\,\text{TeV}}$	14.69 ± 0.41	6.65 ± 0.27	0.745 ± 0.093	7.44 ± 0.29	3.38 ± 0.19	0.371 ± 0.063
data	$554\,745 \pm 745$	3342 ± 58	12.0 ± 3.5	$265\,437 \pm 515$	1022 ± 32	3.0 ± 1.7

Table 6.1: The observed and predicted number of event candidates with statistical uncertainty for the event selection described in section 5.3 including the LQ signal, the background contributions of $t\bar{t}$ and $t\bar{t}H$ processes and data. The integrated luminosity is $140\,\text{fb}^{-1}$.

sample are expected from the possible decay $H^0 \rightarrow \tau^- \tau^+$. This is because the Higgs coupling strength is proportional to the mass and therefore the heaviest lepton (cf. table 2.2) is a direct decay product of the Higgs boson. The reduction of the event yield for both signal samples, when at least one tau is selected, is only down to $(45.9 \pm 5.5)\%$ (mass point 500 GeV) and $(45.3 \pm 4.9)\%$ (mass point 1 TeV). The data event candidates reduce to $(0.6 \pm 1.7)\%$ in that selection. A more detailed efficiency study is presented in the following section 6.2.

6.2 Signal and background efficiencies

Main background contributions are processes from Higgs and top-quark pairs, which contaminate the potential LQ signal. A sub-selection of the event selection (cf. 5.3) allows for a more detailed picture of the final states' origin in the $t\tau^- + \bar{t}\tau^+$ channel for signal and background samples. The MC samples include the so called ‘truth’ information that is the information of the generated particles and the subsequent decay without the digitization and reconstruction step of their signatures in the detector. Taking into account this capability of the MC simulations (cf. 4.6) a comparison between the fully reconstructed events and the mere information of the simulated particles is possible. Thus reconstruction efficiencies are the adequate description for that comparison and give insight to the signal and background composition. The efficiency study for signal and background samples are done in two sections 6.2.1 and 6.2.2 separately.

6.2.1 Tau reconstruction efficiencies and fake rates

The sub-selections for the efficiency study are as follows: The event selection (cf. section 5.3) with at least two b-jets and at least one tau lepton is applied additionally to the object selection (cf. section 5.2), in the following named together as basic selection. Applying the common definition of efficiency, which compares the number of events passing a special selection Z compared to the total event number, different efficiency selections are created. The efficiency definition within the tau reconstruction efficiencies are defined as:

$$\epsilon = \frac{\#\text{truth hadronic } \tau \text{ matched to a reconstructed } \tau + Z}{\#\text{truth } \tau \text{ passing the basic selection} + Z}. \quad (6.1)$$

6 Results

The applied single selections are summarized in table 6.3. The error σ_ϵ is derived from the binomial uncertainty in efficiency following the definition

$$\sigma_\epsilon = \frac{\sqrt{n\epsilon(1-\epsilon)}}{n} .. \quad (6.2)$$

Before discussing the tau reconstruction efficiency a fake rate estimation for the background samples is done at first. The efficiency definition from eq. (6.1) can be transferred into the context of fake rates:

$$f = \frac{\#\text{truth fake candidate matched to a reconstructed } \tau}{\#\text{truth fake candidate passing the basic selection}} . \quad (6.3)$$

Objects that possibly fake a hadronic tau are given the name ‘fake candidate’. Four different fake candidates are available, estimating the taus faked by jets in general, by b-jets, by light jets excluding b-jets and electrons and are summarized in table 6.2. The fake rate for jets that is the number of truth jets matched with a reconstructed tau-jet over the number of truth jets satisfying the basic selection is $(0.1741 \pm 0.0019)\%$ and $(1.0063 \pm 0.0068)\%$ for the top-pair related background and the Higgs related background respectively.

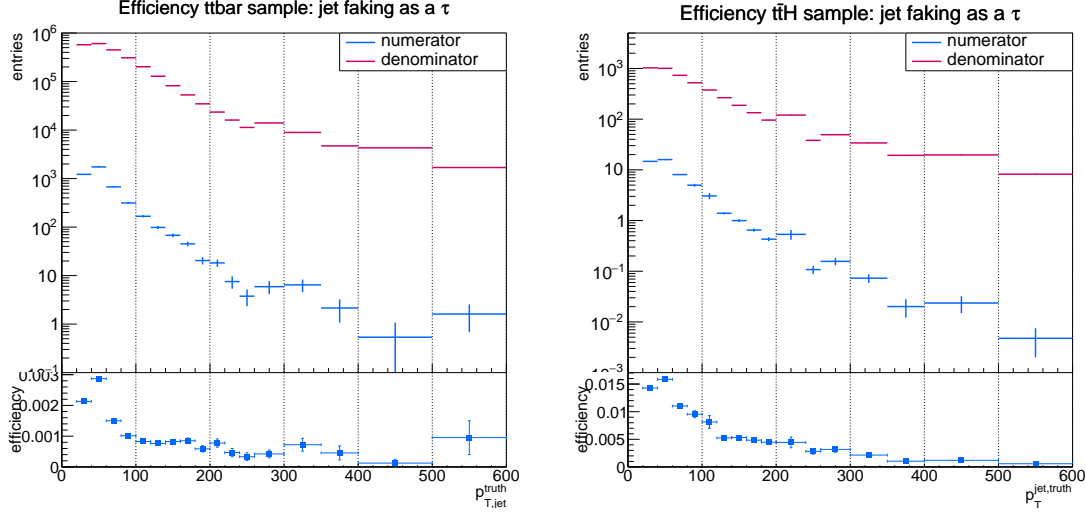
The efficiency depending on the transverse momentum of the truth jet is shown as ratio plot in figure 6.1. The qualitative trend is for both background samples the same, showing a peak fake rate at $p_{T,\text{jet}}^{\text{truth}}$ at 50 GeV. There exists a plateau in the range of the truth jet transverse momentum between 100 GeV and 200 GeV before the efficiency goes down. As a result the jet fake rate depends directly on the jets’ transverse momentum. The main difference is that the fake rate for the $t\bar{t}H$ sample is greater than that of the $t\bar{t}$ sample. These differences in the mean fake rate could be due to the difference in jet composition. For $t\bar{t}$ the jets are gluon-originated (cf. fig. 5.1) and for $t\bar{t}H$ quark-originated (cf. fig. 5.2) jets.

The fake rate for b-jets is defined in the same way as for jets above with the difference of selecting only jets of b-flavor. The fake rate values of the two background samples are not in agreement within the uncertainties, Although they are in the same range of $(0.1616 \pm 0.0022)\%$ and $(0.1496 \pm 0.0033)\%$ corresponding to $t\bar{t}$ and $t\bar{t}H$. The efficiency depending on the truth transverse momentum of the b-jet is shown in figure 6.2. The dependence of the fake rate in case of b-jets faking a tau follows the same trend as observed for jets in general. The only difference is that the b-jet fake rate in the Higgs sample is slightly higher compared to the top-pair sample. This fact can be explained by the p_T dependence of the fake rate: The b-jet’s p_T spectrum is slightly harder in the Higgs sample (see fig. 6.2b) compared to the top-pair sample (see fig. 6.2a). To complete the view on jet composition the next fake candidates are light jets explicitly excluding b-jets and their corresponding fake rate plot is shown in figure 6.3. The fake rate is $(0.2034 \pm 0.0038)\%$ and

sample	$t\bar{t}$			$t\bar{t}H$		
selection	reconstructed taus matched to fake object	total number of potential fake objects	reconstructed taus matched to fake object	reconstructed taus matched to fake object	total number of potential fake objects	
jet faking as tau efficiency	8232 (0.1741 ± 0.0019) %	4728730	21925 (1.0063 ± 0.0068) %	21925 (1.0063 ± 0.0068) %	2178770	
b-jet faking as tau efficiency	5361 (0.1616 ± 0.0022) %	3317260	1993 (0.1496 ± 0.0033) %	1993 (0.1496 ± 0.0033) %	1332650	
not b-jet faking as tau efficiency	2871 (0.2034 ± 0.0038) %	1411470	19932 (2.356 ± 0.016) %	19932 (2.356 ± 0.016) %	846121	
electron faking as tau efficiency	17 (0.00104 ± 0.00025) %	1639390	17 (0.00348 ± 0.00084) %	17 (0.00348 ± 0.00084) %	488234	

Table 6.2: Fake rates for different tau lepton categories for the $t\bar{t}$ and the $t\bar{t}H$ Monte Carlo sample. The fake rate is defined as $f = \frac{\# \text{truth fake candidate matched to a reconstructed } \tau}{\# \text{truth fake candidate passing the basic selection}}$

6 Results



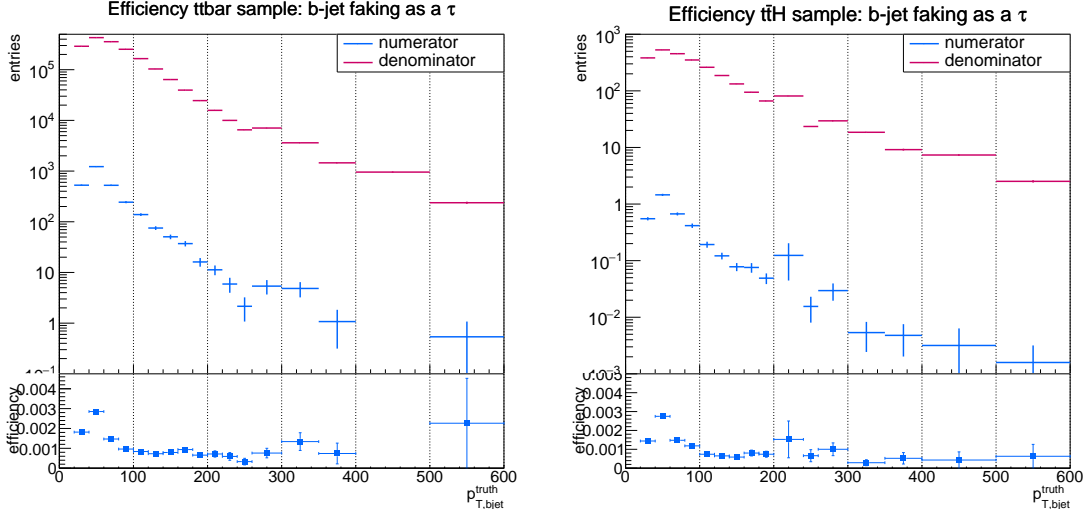
- (a) Estimation of a jet faking a tau lepton of $(0.1741 \pm 0.0019)\%$ for the top-quark pair events.
- (b) Estimation of a jet faking a tau lepton of $(1.0063 \pm 0.0068)\%$ for the Higgs events.

Figure 6.1: Estimation of a jet faking a tau lepton for the background events. The efficiency is defined as number of truth jets passing matched to a tau-jet over the number of truth jets passing the basic selection.

$(2.356 \pm 0.016)\%$ for $t\bar{t}$ and $t\bar{t}H$ sample respectively. As the ratio plot shows, the fake rate is high for the background contributions related to Higgs in a greater range up to 120 GeV, whereas the background contributions related to the top-pair events show the characteristic peak at 50 GeV as observed earlier. The difference in the fake rate, where light jets fake as tau is consistent with the above mentioned fact that the jet composition and therefore the light jet composition is different in both background samples.

The fake tau contributions from electrons is very tiny in this efficiency consideration. The fake rate estimation is done by taking the true number of electrons, which are reconstructed as a hadronic tau over the truth electrons passing the basic selection. For the top-pair related events the fake rate is $(0.00104 \pm 0.00025)\%$ and for the Higgs related events $(0.00348 \pm 0.00084)\%$.

As discussed in section 5.1 the advantage of the $t\bar{t}H$ sample is that it includes real tau signals. Therefore tau efficiency study is not only possible for the signal samples, but can be studied as well of the background is done here for the $t\bar{t}H$ sample. The efficiency definition was already given with eq. (6.1) at the beginning of this section. To determine the tau efficiency further sub-selections shown in table



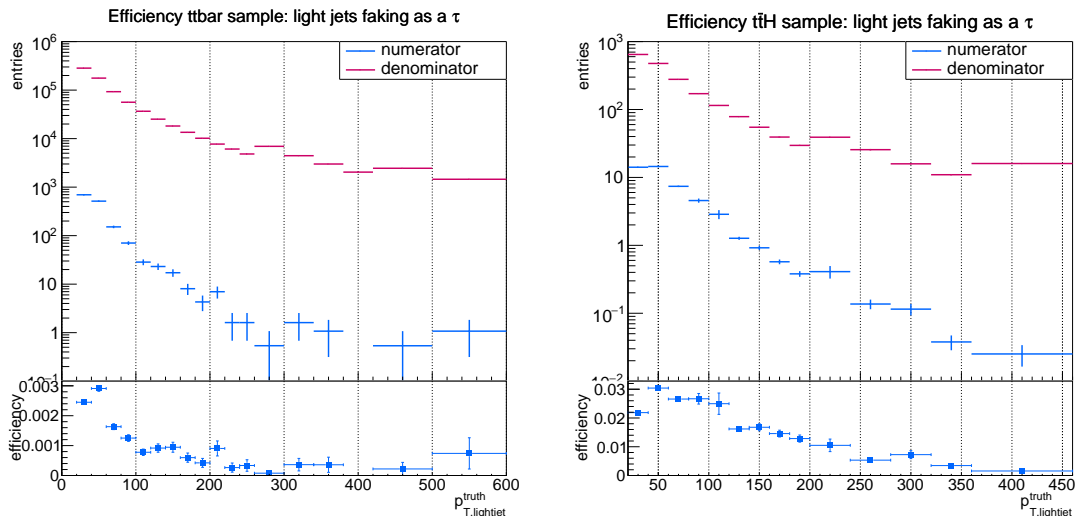
- (a) Estimation of a b-jet faking a tau lepton of $(0.1616 \pm 0.0022)\%$ for the top-quark pair events.
- (b) Estimation of a b-jet faking a tau lepton of $(0.1496 \pm 0.0033)\%$ for the Higgs events.

Figure 6.2: Estimation of a b-jet faking a tau lepton for the background events. The efficiency is defined as number of truth b-jets matched to a tau-jet over the number of truth b-jets passing the basic selection.

sample	$t\bar{t}H$	
selection	reconstructed taus matched to truth taus	total number of taus
tau originated from H^0	5140	11372
efficiency	$(45.20 \pm 0.47)\%$	
tau originated from H^0 (1-prong)	4132	8390
efficiency	$(49.25 \pm 0.55)\%$	
tau originated from H^0 (3-prong)	1008	2958
efficiency	$(34.08 \pm 0.87)\%$	

Table 6.3: Efficiencies for different tau lepton categories for the $t\bar{t}H$ Monte Carlo sample. The efficiency is defined as $\epsilon = \frac{\# \text{truth hadronic } \tau \text{ matched to a reconstructed } \tau+Z}{\# \text{truth } \tau \text{ passing the basic selection} + Z}$.

6 Results



- (a) Estimation of a light jet (excluding b-jets) faking a tau lepton of (0.2034 ± 0.0038) % for the top-quark pair events.
- (b) Estimation of a light jet (excluding b-jets) faking a tau lepton of (2.356 ± 0.016) % for the Higgs events.

Figure 6.3: Estimation of a light-jet (excluding b-jets) faking a tau lepton for the background events. The efficiency is defined as truth number of light jets, explicitly not including the b-flavor, matched to a tau-jet over the number of truth light jets without truth b-jets passing the basic selection.

6.3 are performed.

Two main sources of taus can be distinguished and include both the sub-categories of 1-prong and 3-prong decays (cf. 2.3.6 and 4.5): Taus originating from bosons of the weak interaction (W^\pm, Z^0) and taus originating directly from Higgs bosons. This variety comes with the diversity of the Higgs decay modes like di-boson and di-tau events. Applied overlap removals between tau leptons and light leptons (see section 5.2) reduce the efficiency numbers significantly. Therefore only taus from H^0 are considered.

The efficiency derived from the number of taus matched to a truth tau and originating from a Higgs boson over the total number of truth taus passing the basic selection and its origin from Higgs is $(45.20 \pm 0.47)\%$. The efficiency plot is shown in figure 6.4a. Splitting the taus' origin from H^0 into 1-prong and 3-prong case gives the efficiency of $(49.25 \pm 0.55)\%$ and $(34.08 \pm 0.87)\%$ respectively (see figure 6.4b and 6.4c). The overall efficiency dependence increases towards 200 GeV and fluctuates beyond that threshold for higher transverse momenta. This behavior is mostly dominated by the 1-prong cases with its highest contribution to the prompt Higgs decay, because the 1-prong case in figure 6.4b shows the same trend. In contrast to that, the smaller contributions of $(34.08 \pm 0.87)\%$ efficiency in the 3-prong case show slightly less dependence in efficiency (see fig. 6.4c).

The evaluated efficiencies of the sub-selection, where taus originate directly from Higgs, can also be expressed as a function of various kinematic variables, which is presented here for the $t\bar{t}H$ sample. The next section (6.2.2) provides this study for the LQ signal samples as well.

Thus, as a reference for the LQ signal samples the sum of the transverse momenta of different physical variables $S_{T,\text{lep}}, H_{T,\text{had}}, S_T, H_T$ and the number of jets are plotted against the efficiency for taus originating from Higgs bosons. The definition of the sum-variables are as follows:

$$S_{T,\text{lep}} = \cancel{E}_T + \sum_i p_{T,i}^e + \sum_i p_{T,i}^\mu + \sum_i p_{T,i}^\tau \quad (6.4)$$

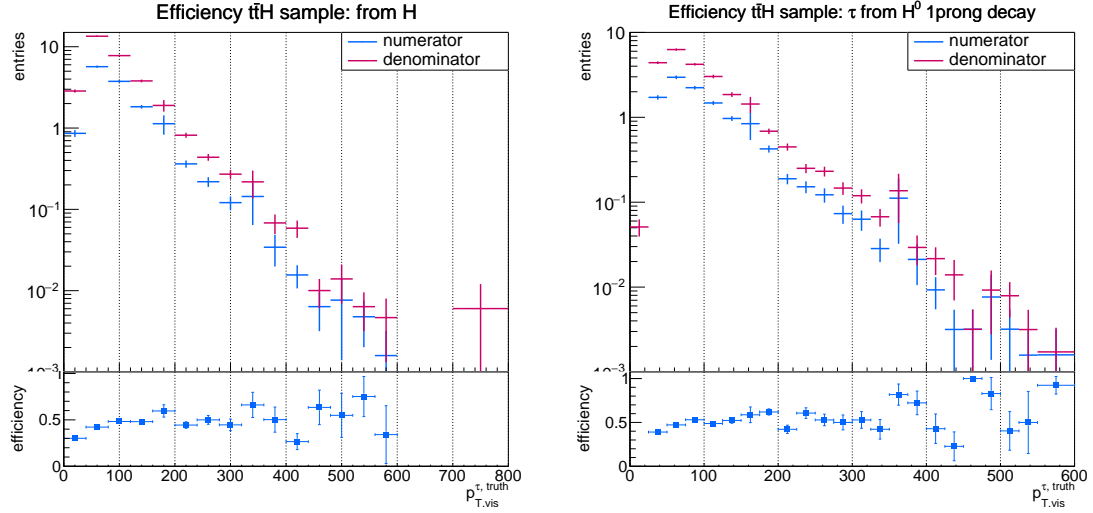
$$H_{T,\text{had}} = \sum_i p_{T,i}^{\text{jet}} \quad (6.5)$$

$$S_T = \cancel{E}_T + \sum_i p_{T,i}^e + \sum_i p_{T,i}^\mu + \sum_i p_{T,i}^\tau + \sum_i p_{T,i}^{\text{jet}} \quad (6.6)$$

$$H_T = \sum_i p_{T,i}^e + \sum_i p_{T,i}^\mu + \sum_i p_{T,i}^{\text{jet}}, \quad (6.7)$$

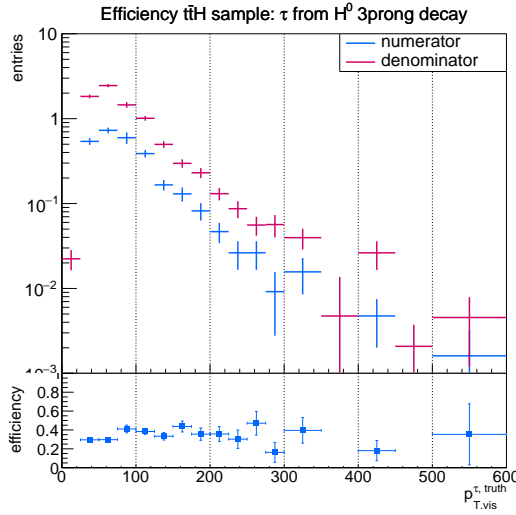
where $p_{T,i}^X$ is the transverse momentum of single electrons $X = e$, muons $X = \mu$, taus $X = \tau$ and jets $X = \text{jet}$ and \cancel{E}_T denotes the missing transverse energy, which includes in standard model considerations the neutrinos. With the definitions of eq. (6.4)-(6.7) different sensitivities are covered. S_T is sensitive to all considered objects

6 Results



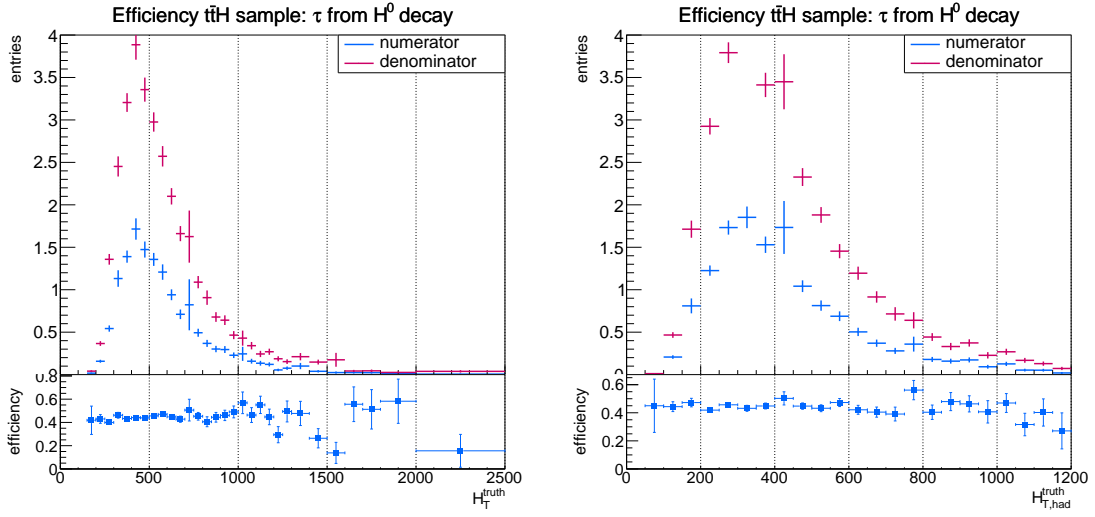
(a) Efficiency of taus originating from Higgs bosons of $(45.20 \pm 0.47)\%$ for the Higgs events.

(b) Efficiency of taus originating from Higgs bosons and decaying in the 1-prong mode. The efficiency is $(49.25 \pm 0.55)\%$ for the Higgs events.



(c) Efficiency of taus originating from Higgs bosons and decaying in the 3-prong mode. The efficiency is $(34.08 \pm 0.87)\%$ for the Higgs events.

Figure 6.4: Efficiency of taus originating from Higgs. The efficiency is defined as the number of taus matched to a hadronic truth tau as well as the origin is from a H^0 boson over the total number of truth taus passing the basic selection and originating from a H^0 boson.



- (a) Efficiency of taus originating from Higgs bosons depending on H_T for the Higgs events.
 (b) Efficiency of taus originating from Higgs bosons depending on $H_{T,\text{had}}$ for the Higgs events.

Figure 6.5: Efficiency of taus originating from Higgs bosons depending on H_T (a) and $H_{T,\text{had}}$ (b) for events from $t\bar{t}H$ sample.

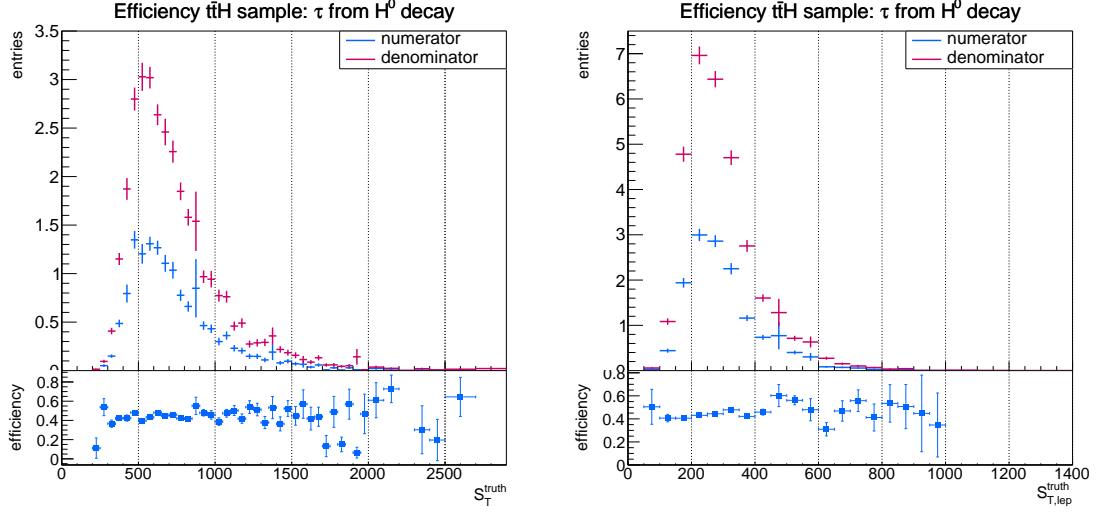
with the sub-category of $S_{T,\text{lep}}$, which only takes the leptonic objects into account, while H_T is sensitive to electrons and muons as well as jets. $H_{T,\text{had}}$ only includes jets.

In figure 6.5 the sum of the transverse momenta are shown against the efficiency in case of taus generated by H^0 . Adding up the electrons' and muons' transverse momentum (see 6.5a) to the sum of the jets' transverse momentum (see 6.5b) influences the number of elements and expands the spectrum, but influences not the shape of the efficiency depicted in the ratio plot. Only slight changes in efficiency is visible apart from the constant efficiency curve in the ratio plot for the variable H_T . The difference of the variables regarding electrons and muons adds one remarkable minimum to the efficiency depending on H_T at 1.45 TeV to the efficiency dependence, which can be local lack of enough statistics.

The sum of all considered objects in S_T or the subset $S_{T,\text{lep}}$ are depicted in figure 6.6a and 6.6b respectively. Efficiency variations over the whole momentum range in S_T are caused mainly by hadronic tau multiplicity and transverse momenta, because H_T and $H_{T,\text{had}}$ does not contain hadronic taus. This conclusion can be drawn from stronger variations in the $S_{T,\text{lep}}$ distribution (see fig. 6.6b).

The efficiency dependence on the number of jets shows very low efficiency of 5% for taus originating from Higgs bosons with 2 jets, while with 3 jets the efficiency

6 Results



- (a) Efficiency of taus originating from Higgs bosons of depending on S_T for the Higgs events.
 (b) Efficiency of taus originating from Higgs bosons of depending on $S_{T,\text{lep}}$ for the Higgs events.

Figure 6.6: Efficiency of taus originating from Higgs bosons depending on S_T (a) and $S_{T,\text{lep}}$ (b) for events from $t\bar{t}H$ sample.

increases significantly and its further trend is continuously. The efficiency graph is shown in figure 6.7.

Decay characteristics will influence the separation of different objects involved in the event selection. Therefore the minimum and maximum separation ΔR is studied between taus and leptons, taus and jets as well as taus and b-jets. This is done for taus originated from Higgs bosons.

Figure 6.8 shows the minimum and maximum separation between taus and light leptons (electrons and muons) for the origin candidate H^0 . Almost no efficiency dependence for the minimum separation can be detected , besides the low efficiency at $\Delta R < 0.5$ which results from overlap removal between these objects. The maximum separation between taus and light leptons in contrast show fluctuations in the separation range $2.4 < \Delta R < 3.0$.

The minimum and maximum separation between taus and jets is presented in figure 6.9. For that case of the taus' origin from Higgs they seem to be either well separated explained by peak in number of tau leptons at $\Delta R = 3.0$ for the maximum separation (see figure 6.9b). Or there is no separation shown by the abundant entries for $\Delta R < 0.5$ in the minimum separation (see fig. 6.9a), which become the main fake rate contributors for the category jets. High efficiency dependence is shown from the maximum separation in the range of less than 2.0.

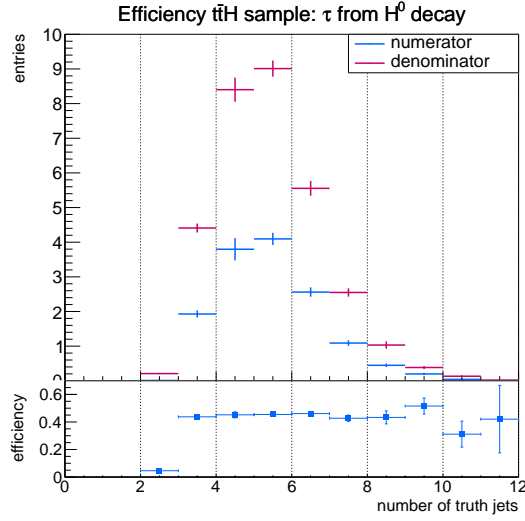
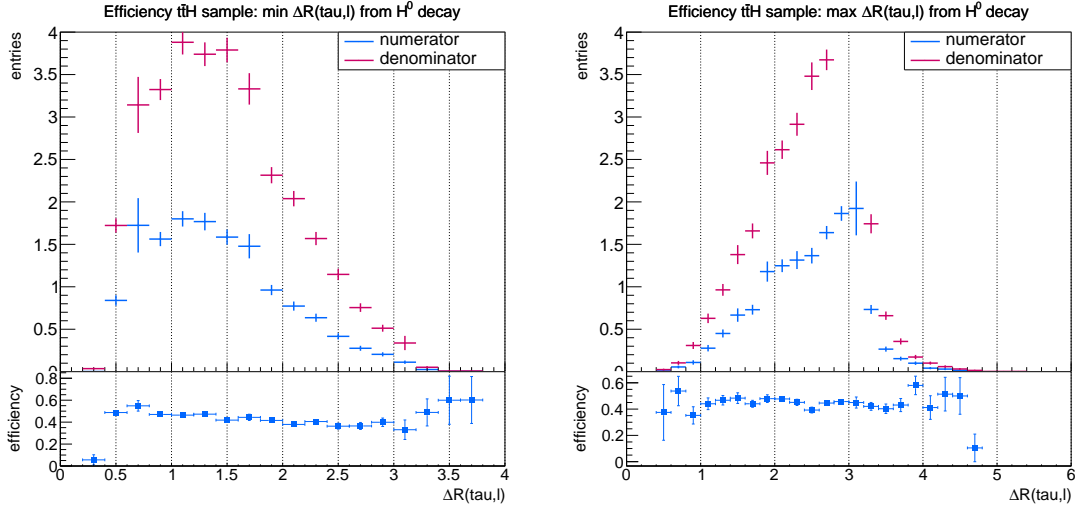


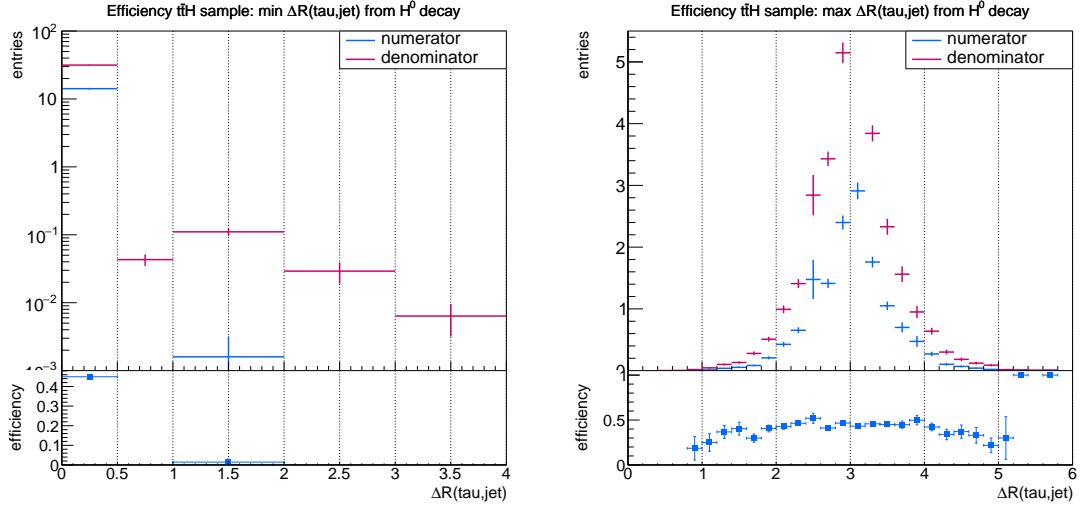
Figure 6.7: Efficiency of taus originating from Higgs bosons depending on the number of jets.



(a) Minimum separation between taus originating from the Higgs events and leptons.
 (b) Maximum separation between taus originating from the Higgs events and leptons.

Figure 6.8: Efficiency of taus originating from Higgs bosons for the minimum and maximum separation between taus and leptons (electrons and muons).

6 Results



- (a) Minimum separation between taus originating from the Higgs events and jets. (b) Maximum separation between taus originating from the Higgs events and jets.

Figure 6.9: Efficiency of taus originating from Higgs bosons for the minimum and maximum separation between taus and jets.

The maximum separation between taus and b-jets shows a slightly shifted peak at $\Delta R = 2.8$ compared to the jet separation (see 6.10b), but the efficiency dependence is very similar to the jets separation. This is valid for taus coming from H^0 . The minimum separation between taus and b-jets show large changes compared to all jet flavors (see 6.10b). The minimum separation is extended over a full separation range up to $\Delta R = 4.5$ and has significantly less efficiency close to zero for small separations.

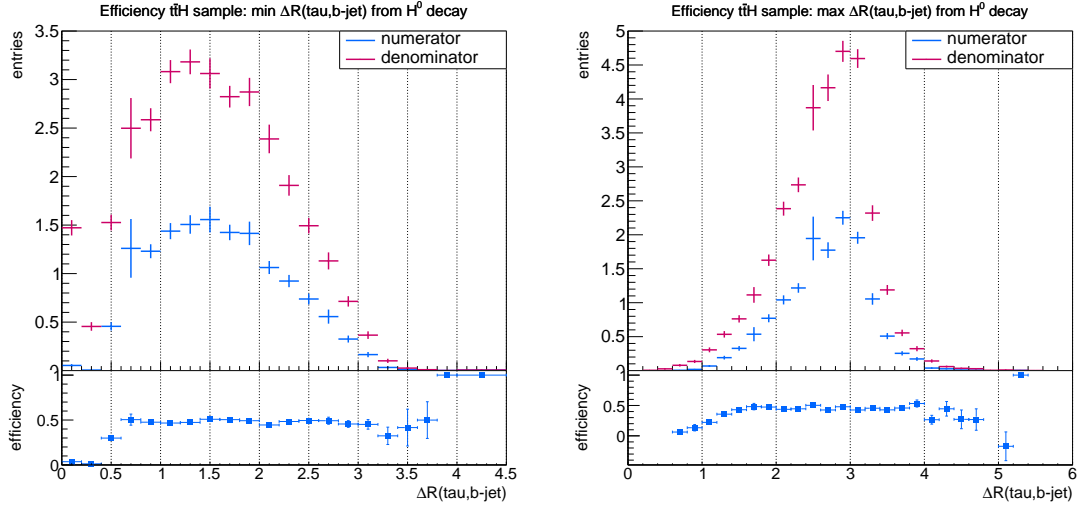
6.2.2 Taus reconstruction efficiency in signal samples

The efficiencies for the leptoquark signal samples with their two mass points are summarized in table 6.4 following the example of the background efficiencies in table 6.3. The uncertainty is derived from the binomial error of the efficiency after eq. (6.2). The efficiency definition is the same as for the background samples (see eq. (6.1)) with the difference that the category of taus originating from a Higgs boson is replaced by the category of tau leptons originating from leptoquarks.

sample		$LQ_{500\text{GeV}}$		$LQ_{1\text{TeV}}$	
selection	reconstructed taus matched to truth taus	total number of taus	reconstructed taus matched to truth taus	total number of taus	
tau originated from LQ efficiency	905 (51.3 ± 1.2) %	1764	571 (50.7 ± 1.5) %	1127	
tau originated from LQ (1-prong) efficiency	745 (55.5 ± 1.4) %	1343	160 (55.0 ± 1.7) %	419	
tau originated from LQ (3-prong) efficiency	160 (38.2 ± 2.4) %	419	94 (36.3 ± 3.0) %	259	

Table 6.4: Efficiencies for different tau lepton categories for the two different LQ Monte Carlo samples with 500 GeV and 1 TeV mass point. The efficiency is defined as $\epsilon = \frac{\#\text{truth hadronic } \tau}{\#\text{truth } \tau}$ matched to a reconstructed $\tau + Z$. passing the basic selection + Z .

6 Results

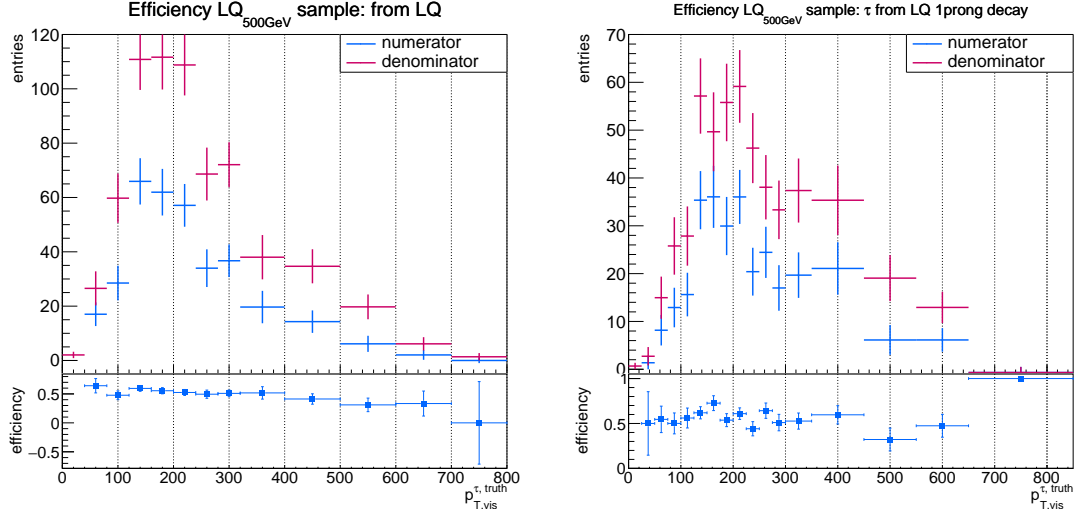


- (a) Minimum separation between taus originating from the Higgs events and b-jets. (b) Maximum separation between taus originating from the Higgs events and b-jets.

Figure 6.10: Efficiency of taus originating from Higgs bosons for the minimum and maximum separation between taus and b-jets.

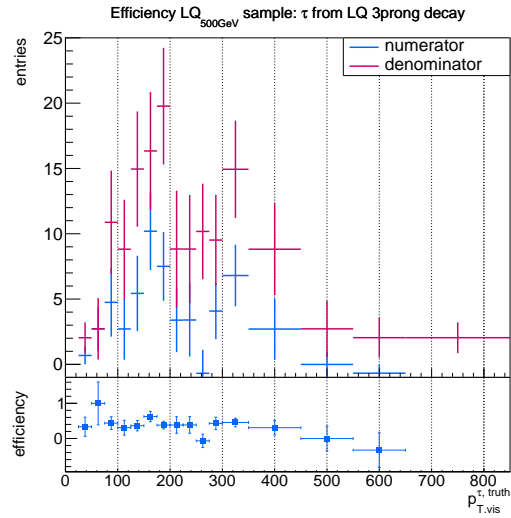
Taus originating directly from LQs have an efficiency of $(51.3 \pm 1.2)\%$ and $(50.7 \pm 1.5)\%$ for the low and high mass point respectively. These two efficiencies are in agreement with each other. The corresponding efficiency plots can be found in figure 6.11 and 6.12 as well as the efficiency categories for taus decaying into one charged or three charged particles. The efficiency for 1-prong decaying taus in case of the low mass LQ sample is $(55.5 \pm 1.4)\%$ and $(38.2 \pm 2.4)\%$ for the 3-prong case. The high mass point LQ samples shows efficiencies for the 1-prong and 3-prong case of $(55.0 \pm 1.7)\%$ and $(36.3 \pm 3.0)\%$. Taus directly from the low mass point leptoquarks show a slight efficiency dependence of the transverse momentum (see 6.11). Towards high momenta the efficiency decreases slightly. Differences in 1-prong and 3-prong cases are not present.

For the high mass point leptoquarks the efficiency dependence on the taus' transverse momentum is constant over the whole momentum range (see fig. 6.12). Like for the low mass point, the 1-prong case reveals no considerable dependence on the taus' p_T . More fluctuations in efficiency can be observed in case of 3-prong (see fig. 6.12c). The slight efficiency decrease for the low mass point sample could be an effect due to the higher mass point of the second LQ sample and the resulting more expanded p_T spectrum, because it shows not such effects. The dependence of the efficiency on kinematic variables like H_T , $H_{T,\text{had}}$, S_T , $S_{T,\text{lep}}$ defined in eq. (6.4)-(6.7)



(a) Efficiency of taus originating LQs of $(51.3 \pm 1.2)\%$ for the low mass LQ events.

(b) Efficiency of taus originating LQs and decaying in the 1-prong mode. The efficiency is $(55.5 \pm 1.4)\%$ for the low mass LQ events.



(c) Efficiency of taus originating LQs and decaying in the 3-prong mode. The efficiency is $(38.2 \pm 2.4)\%$ for the low mass LQ events.

Figure 6.11: Efficiency of taus originating LQs for the low mass LQ signal events. The efficiency is defined as the number of taus matched to a hadronic truth tau over the number of truth taus passing the basic selection.

6 Results

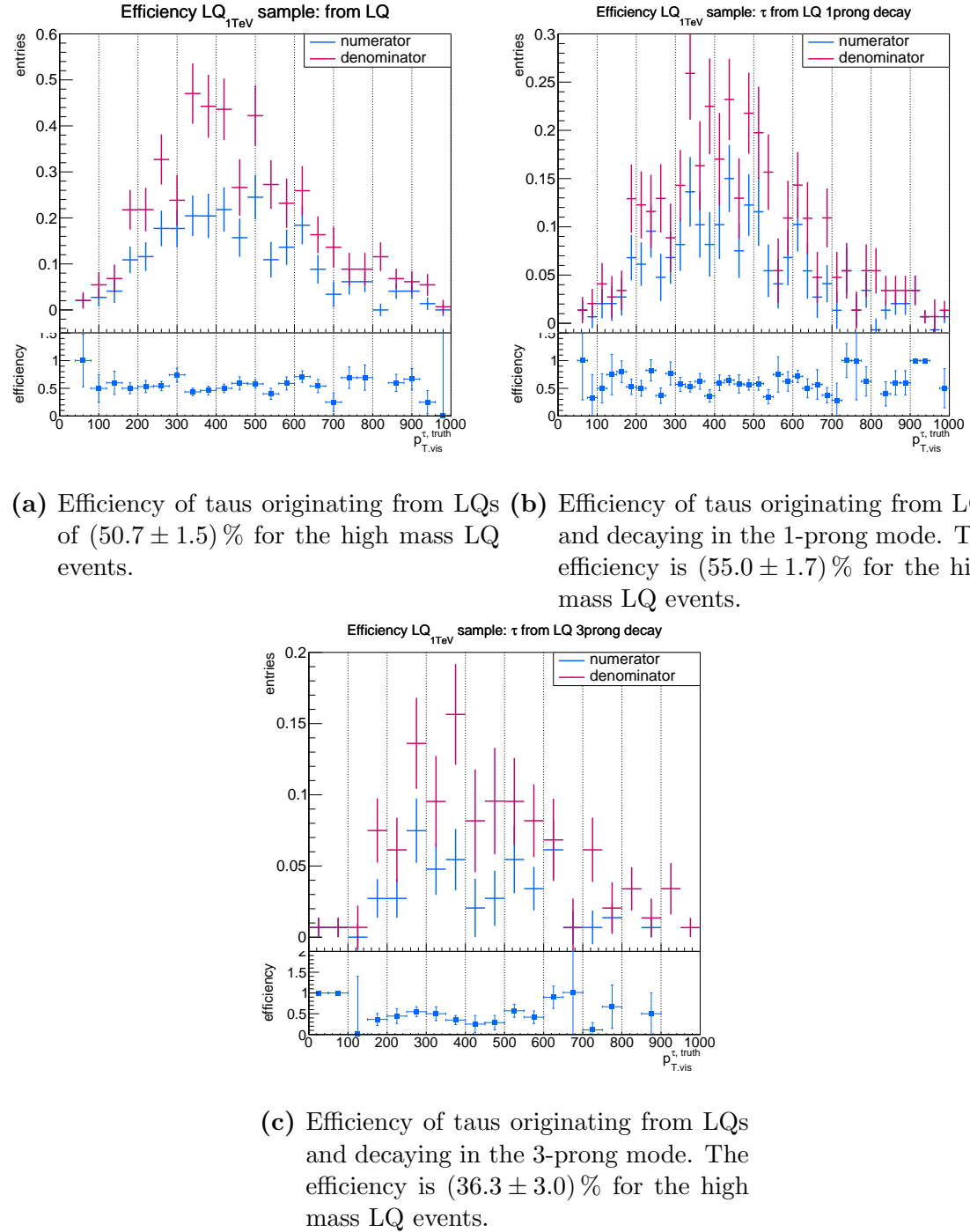


Figure 6.12: Efficiency of taus originating LQs for the high mass LQ signal events. The efficiency is defined as the number of taus matched to a hadronic truth tau over the number of truth taus passing the basic selection.

and the number of jets is also available for the leptoquark related events.

The dependence between H_T ($H_{T,\text{had}}$) and the efficiency in case of the sub-category, where tau leptons originate from LQs, are shown in figure 6.13. The H_T ($H_{T,\text{had}}$) spectrum covers a larger range for the 1 TeV leptoquarks sample due to its higher mass. The H_T distribution extends up to 3 TeV (see fig. 6.13c) compared to figure 6.13a, which extends only to 2.5 TeV. The $H_{T,\text{had}}$ distribution extends up to 2.5 TeV (see fig. 6.13d) compared to figure 6.13b, which extends to 1.2 TeV. The efficiency trend over the whole spectrum is constant besides some fluctuations.

Taking into account not only jets, electrons and muons, but also taus and missing energy for example one can study the correlation between the efficiency and S_T ($S_{T,\text{lep}}$). This is done in figure 6.14 for taus originating from Higgs bosons. The efficiency depends only slightly on the variable S_T (see fig. 6.14a) or $S_{T,\text{lep}}$ (see fig. 6.14b) over the whole spectrum, whereas in case of the more massive LQ sample the efficiency increases towards the high momenta end of the spectrum. This involves the range of 2600 GeV onwards for S_T and 2000 GeV onwards for $S_{T,\text{lep}}$. This difference can exist because of the different mass points of the leptoquarks. The spectrum of the 1 TeV naturally extends to a higher momenta values.

The jet multiplicity depicted against the efficiency can be found in figure 6.15 and shows an interesting feature in both LQ samples. No tau entries for two jets survived the condition that taus are directly from LQ and matched to a truth tau. The low efficiency for two jets in case of the $t\bar{t}H$ sample (see fig. 6.7) may indicate that the already tight conditions for two jets evoked in case of taus originating from LQ that no event survives. The following describes the geometric separation between taus and leptons, taus and jets as well as taus and b-jets for the LQ signal samples.

The minimum separation between taus and light leptons (electrons and muons) is shown in figure 6.16 for both signal samples. It is the efficiency for taus originating from H^0 bosons. The minimum separation is not only concentrated on a small ΔR range, but extends over the whole separation spectrum. A maximum number of taus with minimal separation can be found at $\Delta R = 1.6$ in case of the low mass point sample. Below $\Delta R < 0.4$ no taus can be found, which is explained by the overlap removal (cf. section 5.2). The maximum separation for the 500 GeV sample (see fig. 6.16b) indicates most tau events at $\Delta R = 3.0$. Below $\Delta R < 0.8$ no entry can be found. An interesting feature is that for the maximum separation two efficiency peaks are present at a separation of 1.0 and 1.6. For the 1 TeV signal sample the minimum separation (see fig. 6.16c) does not undercut the value of 0.4 which can be explained again by the overlap removal. Comparing figure 6.16a and 6.16c shows that in case of the high mass point LQ sample no maximum number of taus can be found around $\Delta R = 1.6$. In this case it is more a plateau. Again, two efficiency peaks show up at a separation of 1.0 and 2.0. The maximum separation (see fig. 6.16d) indicates slightly higher efficiency at the end of the separation distribution.

Correspondingly to the background samples the minimum and maximum separation between taus and jets is shown in figure 6.17 for taus originating directly from

6 Results

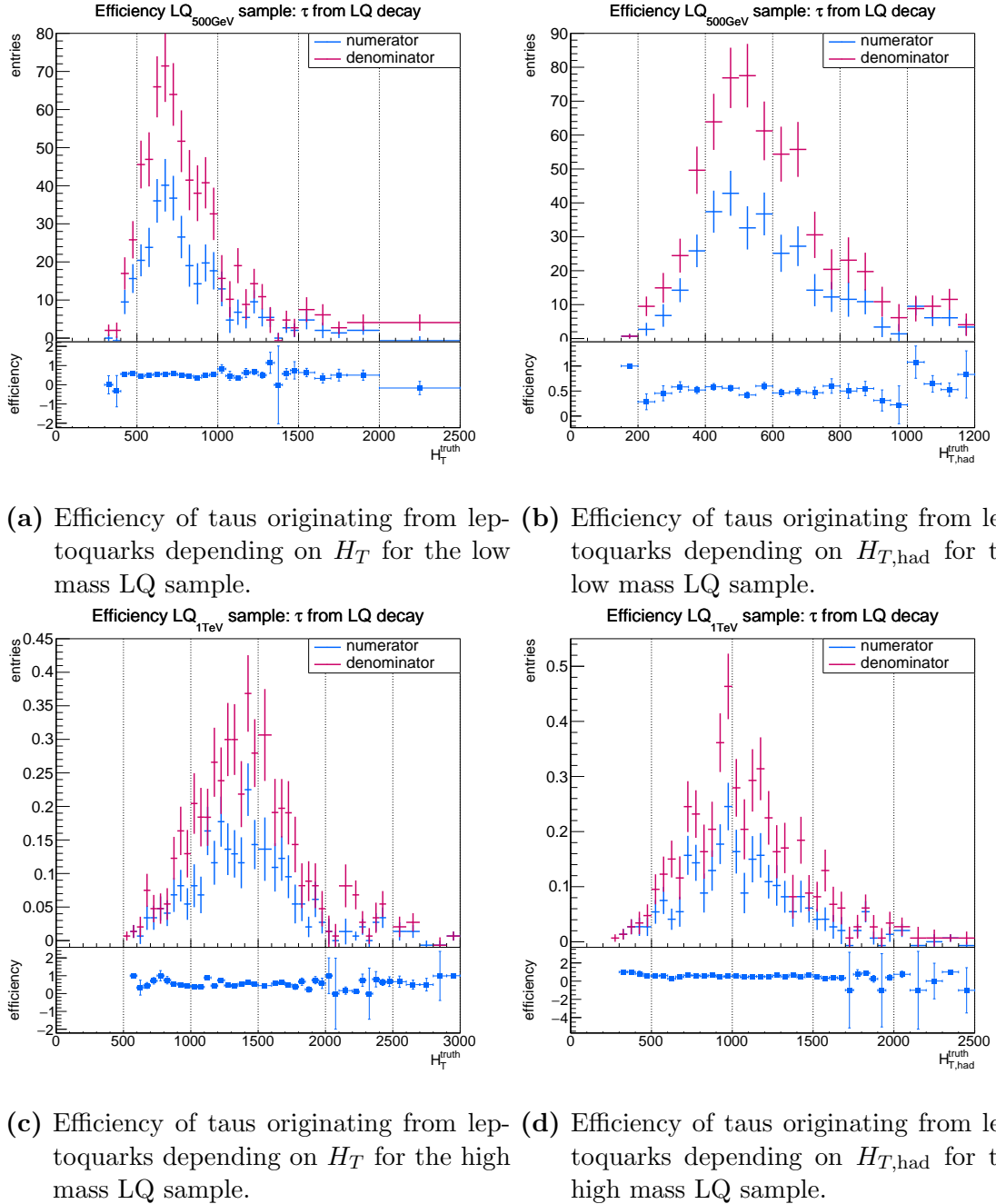


Figure 6.13: Efficiency of taus originating from leptoquarks depending on H_T (a), (c) and $H_{T,\text{had}}$ (b), (d) for the LQ signal events.

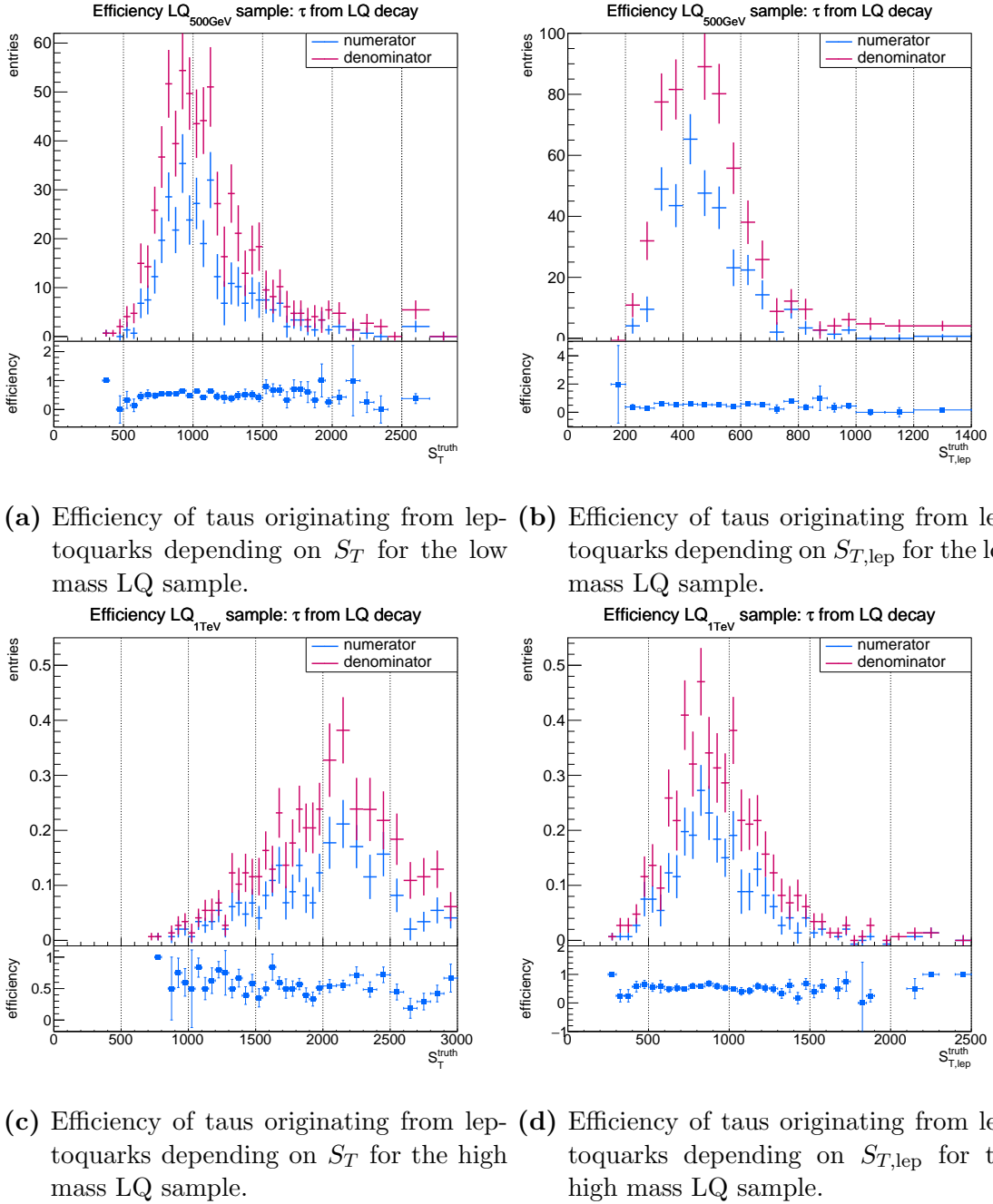
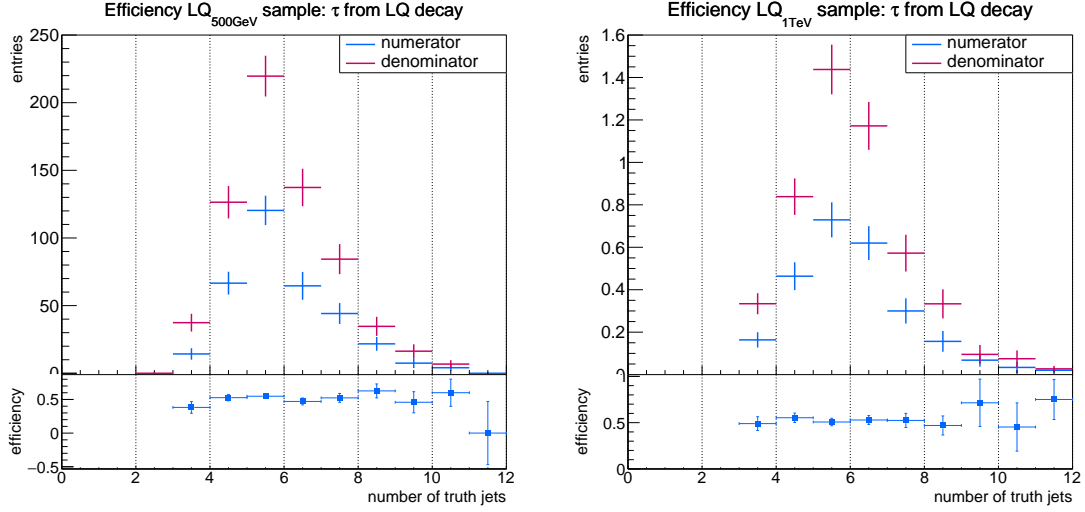


Figure 6.14: Efficiency of taus originating from leptoquarks depending on S_T (a), (c) and $S_{T,\text{lep}}$ (b), (d) for the LQ signal events.

6 Results



(a) Efficiency of taus originating from LQs depending on the number of jets for the LQ sample with low mass point.

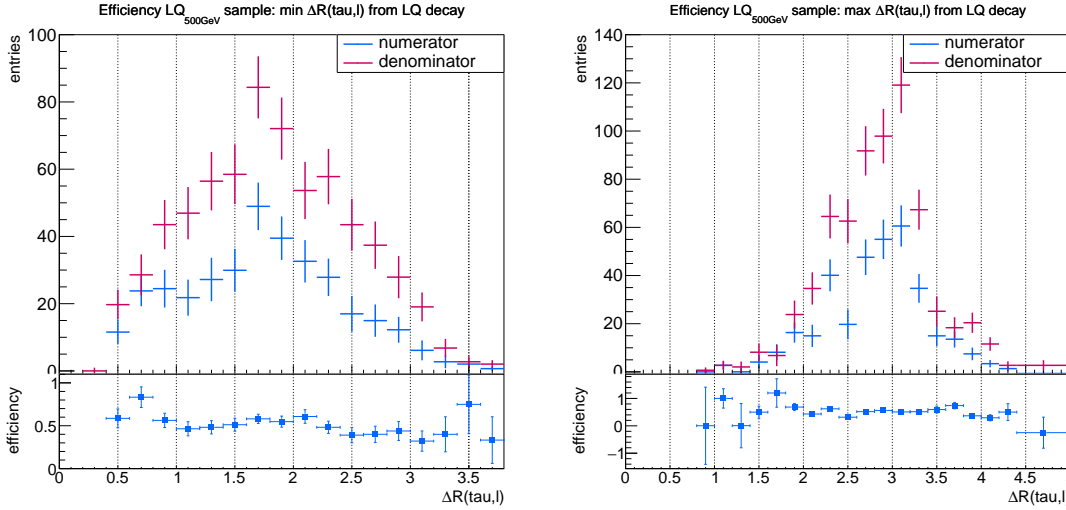
(b) Efficiency of taus originating from LQs depending on the number of jets for the LQ sample with high mass point.

Figure 6.15: Efficiency of taus originating from LQs depending on the number of jets.

LQs. Similar to the separation in the $t\bar{t}H$ sample (cf. figure 6.9) the minimum separation has only high efficiency values at $\Delta R < 0.5$ and no entries otherwise in the spectrum. This can be explained by the jet fake rates, which are expected in that separation region. The maximum separation for both signal samples resembles in principle that from the $t\bar{t}H$ sample with the most taus at a separation of 3.0. No number of taus are found below $\Delta R = 1.2$ and $\Delta R = 1.4$ for the low and high mass point signal sample respectively.

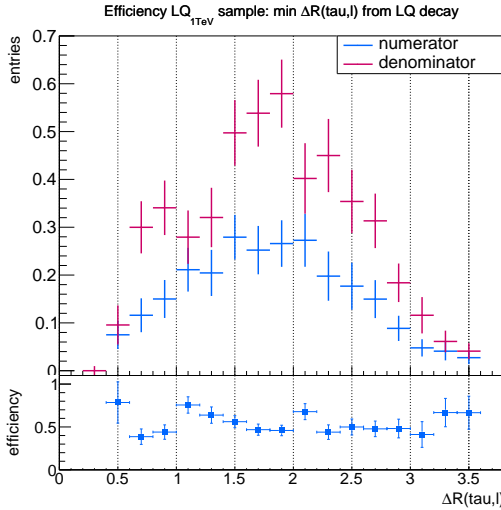
The special case of the minimum and maximum separation between taus and b-flavor jets is shown in figure 6.18 for the sub-category taus originating from LQs. The separation between taus and b-jets in the 500 GeV sample show a broad spectrum over the whole separation range. The minimum separation (see fig. 6.18a) and maximum separation (see fig. 6.18b) show two efficiency peaks within the range of $1.0 < \Delta R < 2.0$ and $1.0 < \Delta R < 2.2$ respectively. Small contributions are found for the minimum separation at < 0.4 (see fig. 6.18c). The 1 TeV sample also shows low efficiency in the range of < 0.4 for the minimum separation. Again peaks of efficiency show up here in the range of 1.0 and 1.4 for the minimum and maximum separation (see fig. 6.18d) respectively.

6.2 Signal and background efficiencies



(a) Minimum separation between taus originating from LQs events and leptons for the low mass point LQ sample.

(b) Maximum separation between taus originating from LQs events and leptons for the low mass point LQ sample.



(c) Minimum separation between taus originating from LQs events and leptons for the high mass point LQ sample.

(d) Maximum separation between taus originating from LQs events and leptons for the high mass point LQ sample.

Figure 6.16: Efficiency of minimum and maximum separation between taus originating from LQs and leptons (electrons and muons).

6 Results

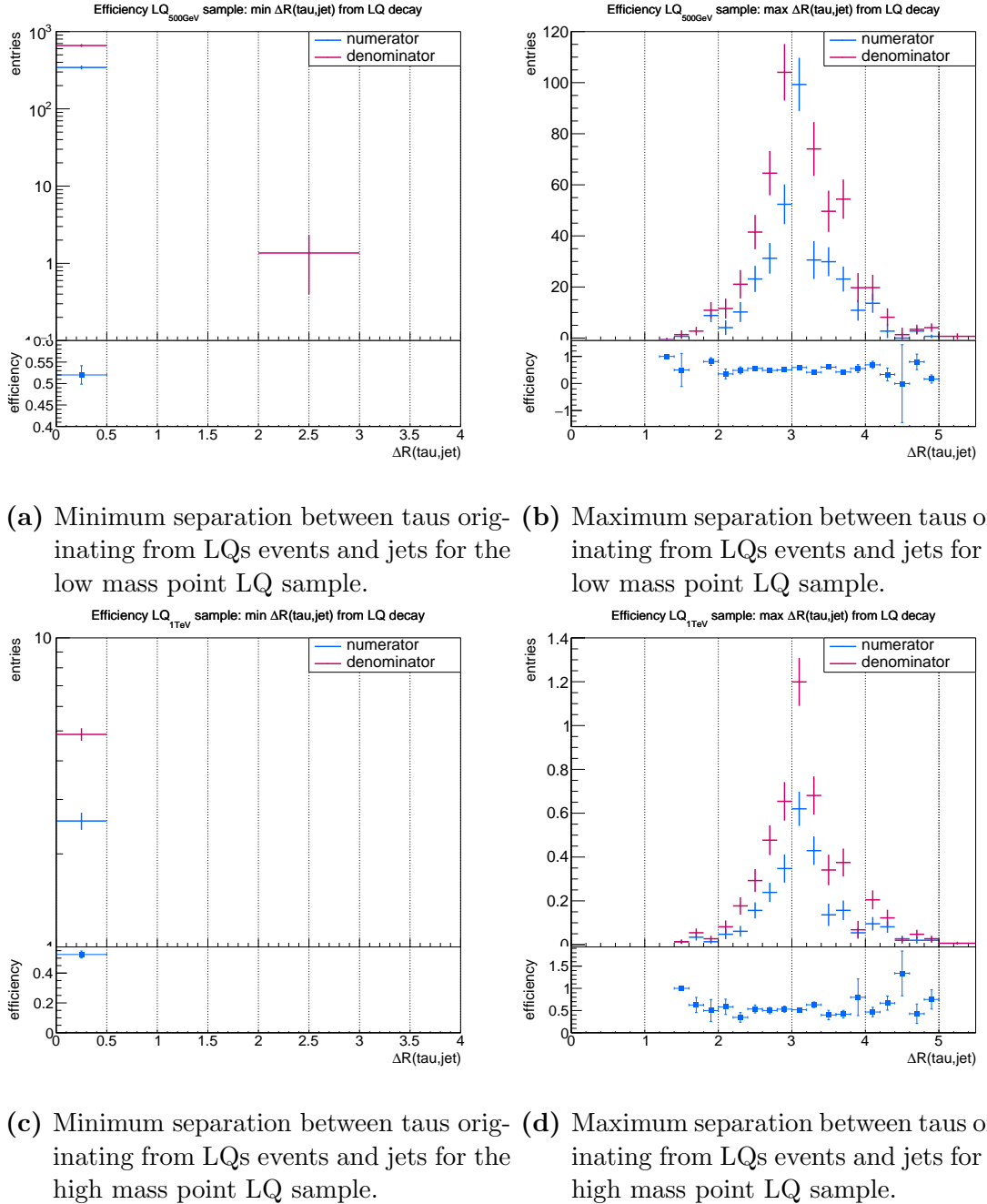
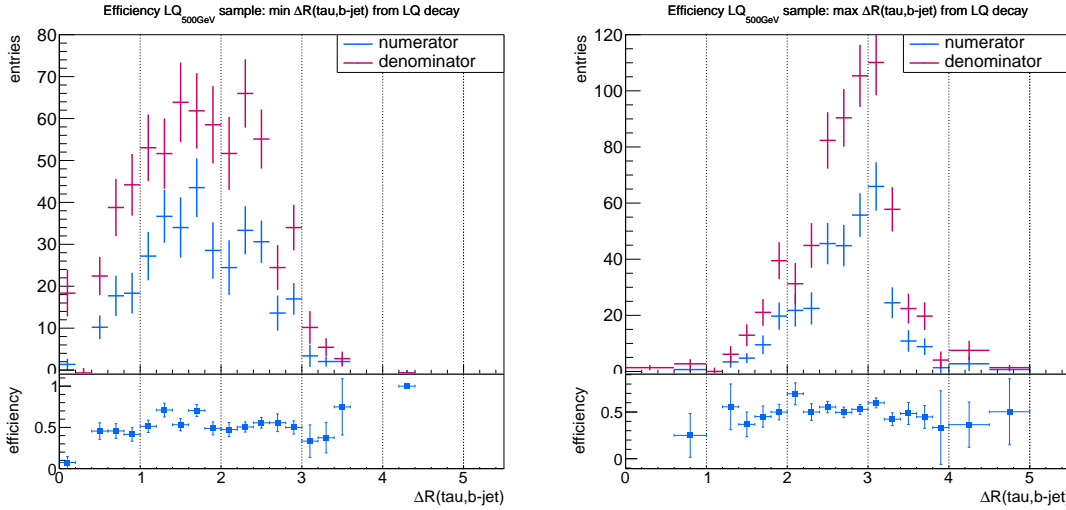
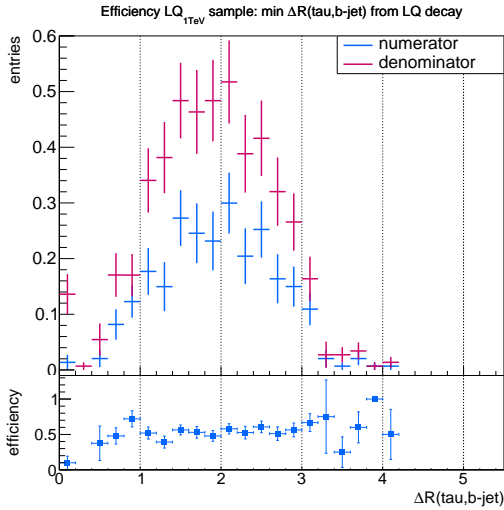


Figure 6.17: Efficiency of minimum and maximum separation between taus originating from LQs and jets.



(a) Minimum separation between taus originating from LQs events and b-jets for the low mass point LQ sample.

(b) Maximum separation between taus originating from LQs events and b-jets for the low mass point LQ sample.



(c) Minimum separation between taus originating from LQs events and b-jets for the high mass point LQ sample.

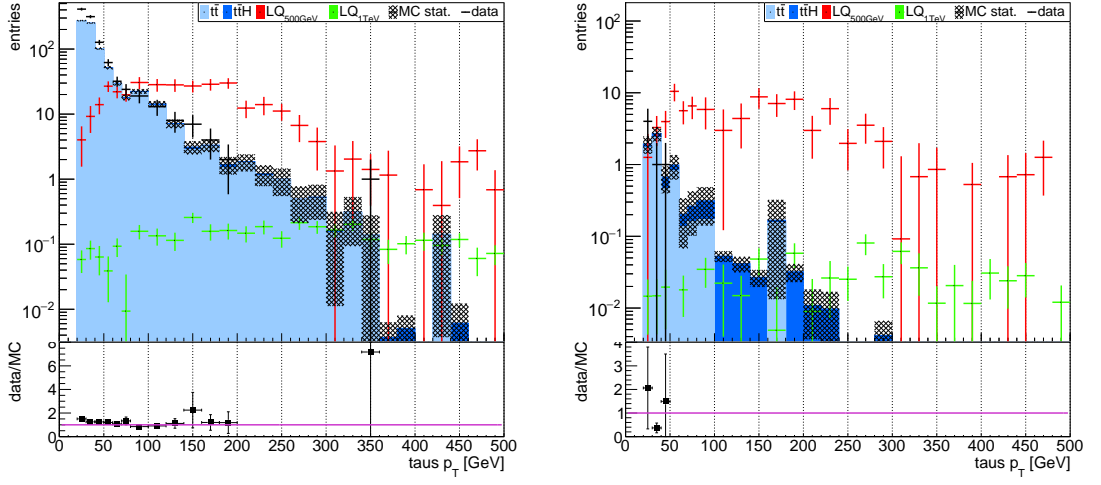
(d) Maximum separation between taus originating from LQs events and b-jets for the high mass point LQ sample.

Figure 6.18: Efficiency of minimum and maximum separation between taus originating from LQs and b-jets.

6.3 Kinematics

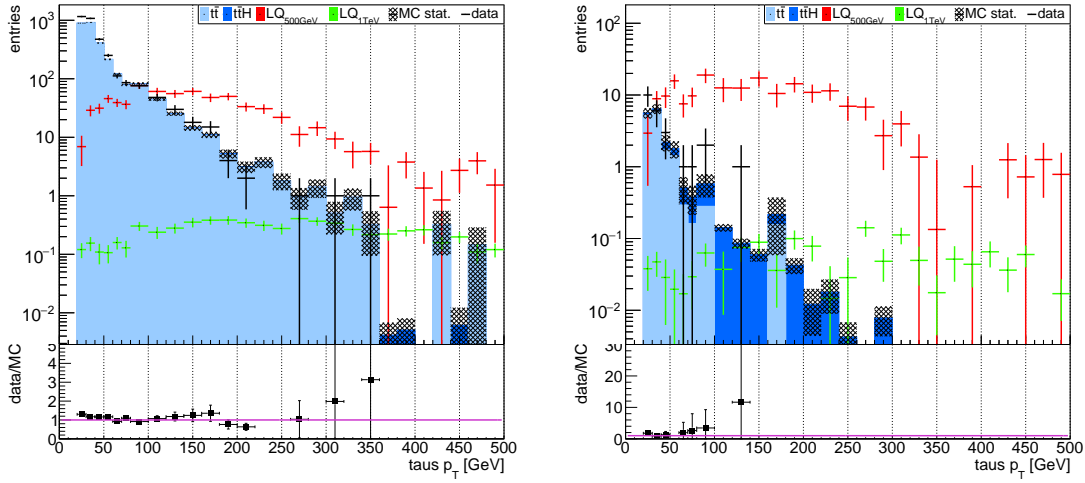
The signal and background efficiencies in section 6.2 help to understand especially the role of the tau lepton for the relevant $t\tau^- + \bar{t}\tau^+$ channel. The next step into the direction of signal studies is to compare the event yield for signal and background samples in the different channels of the event selection (cf. section 5.3). This is done by studying kinematic variables for the tau lepton like the transverse momentum, angular distribution, the variables defined in eq. (6.4)-(6.7) (cf. section 6.2.1) and the separation between taus and objects like electrons, jets and b-jets. The comparison is done with the background and signal MC samples together with data of the data-taking years 2015 until 2018. This reveals, if the signature of the chosen event selection can be extracted and detected within the known standard model processes. The data in this context gives the possibility of reference how well data is resembled by the MC simulation, although this work is not a full LQ search. No systematic variations are applied on the Monte Carlo simulations, which would be the normal procedure for a full search. For data the luminosity of 140 fb^{-1} (cf. table 5.1) is available.

The transverse momentum distribution of all tau leptons is shown in figure 6.19 for different event selections. The selection of at least two b-jets and at least one tau shows (see figure 6.19a) that up to transverse momenta of 80 GeV the LQ signal is hidden from top-quark pair and Higgs contributions. But from that threshold on the momentum distribution of the low mass signal sample exceeds the background. For the high mass point sample this happens at 360 GeV . The MC background samples agree well with data from 50 GeV onward, besides one outlier. Before that value data exceeds the background taken into account. The discrepancy can be explained such that more contributions should be taken into account like vector bosons and additional jets, di-boson events or single-top contributions. Tightening the selection to at least two taus (see figure 6.19b) will reveal even more signal compared to relatively small background. The event yield for data shows that only few events in this selection is expected. The disadvantage in this selection is the few events in general, which results in low statistics. The looser selection of taking only at least one b-jet and at least one tau (see figure 6.19c) shifts the threshold for the signal up to 100 GeV and 350 GeV for the low and high mass point LQ sample respectively, but allows at the same time higher statistics. This effect is clearly visible in the selection of at least one b-jet and at least two tau leptons shown in figure 6.19d. The discrepancy between data and MC in the lower p_T range also exists here, as it depends not directly on the chosen selection. The transverse momentum of taus in data does not exceed 350 GeV and 150 GeV for the selection with at least one tau and at least two taus respectively. This would be interesting threshold for p_T cuts to optimize the signal (see also section 6.4).



(a) p_T distribution of the tau leptons, when selecting at least two b-jets and at least one additional tau.

(b) p_T distribution of the tau leptons, when selecting at least two b-jets and at least two additional tau.



(c) p_T distribution of the tau leptons, when selecting at least one b-jets and at least one additional tau.

(d) p_T distribution of the tau leptons, when selecting at least one b-jets and at least two additional tau.

Figure 6.19: Transverse momentum distribution of all tau leptons for different event selections.

6 Results

The distribution of the azimuthal angle of the tau leptons for different event selection is shown in figure 6.20. It gives the same picture as for the transverse momentum distribution including the lack of MC events. For the selection of at least two b-jets and at least one tau the signal samples are hidden by the background over the whole ϕ range (see figure 6.20a and 6.20c). Only the at least two tau selection reveals the LQ signal. Better statistics can be achieved by using the selection with at least one b-jet and at least two taus (see figure 6.20d).

The pseudorapidity distribution shows the same trend as the p_T and ϕ distribution described above and is shown in figure 6.21. Although the η distribution of the LQ signal has more events concentrated in the region of roughly $|\eta| < 1.5$ compared to the standard model prediction and data, this difference in shape cannot be used as discriminating variable. The background hides too much in with this selection. Even the high mass point LQ sample can not be extracted in the selection of at least two taus. In general the high p_T range and the selection of two taus is more dominated from Higgs background processes, whereas the top-quark pair background processes cover the lower transverse momentum range and selection with less than two taus. This is due to real tau production in the $t\bar{t}H$ sample.

Following the definition of eq. 6.6 (cf. section 6.2.1) the distribution of the missing energy for different selections is shown in figure 6.22. The missing energy is not a optimal discriminant variable, because the signal is not well separated over the whole E_T range in the selection of at least one b-jet and at least one tau (see 6.22c). The signal is in fact better separated in the selection of at least two b-jets and at least one tau as depicted in figure 6.22a. The at least two tau condition improves the separation (see figure 6.22b and 6.22d) between signal and background. Although the studied $t\tau^- + \bar{t}\tau^+$ channel has sources of neutrinos responsible for missing transverse energy through the decay of tau leptons or leptonic W^\pm decays, this is not enough to discriminate it from background neutrino contributions. Again, at least two taus selected induces a more $t\bar{t}H$ dominated background.

The distribution of H_T is shown in figure 6.23. Because this distribution is the sum of the transverse momenta of electrons, muons and jets this is good discriminating variable for particles with high masses like the leptoquarks. High masses like the 0.5 TeV or even 1 TeV produce a broader H_T spectrum extending to higher transverse momenta, which then in turn can be distinguished from standard model events. Figure 6.23a shows that the background decreases from 600 GeV on and reveals at least the 500 GeV mass LQ signal. The selection of at least one tau is not sufficient for the high LQ mass point. The best extraction results are gained from selecting at least two taus and is shown in figure 6.23b and 6.23d. These two selections again show that the $t\bar{t}H$ events are more dominant for the two tau selection due to its abundant tau events. Data has higher event numbers for the selection with

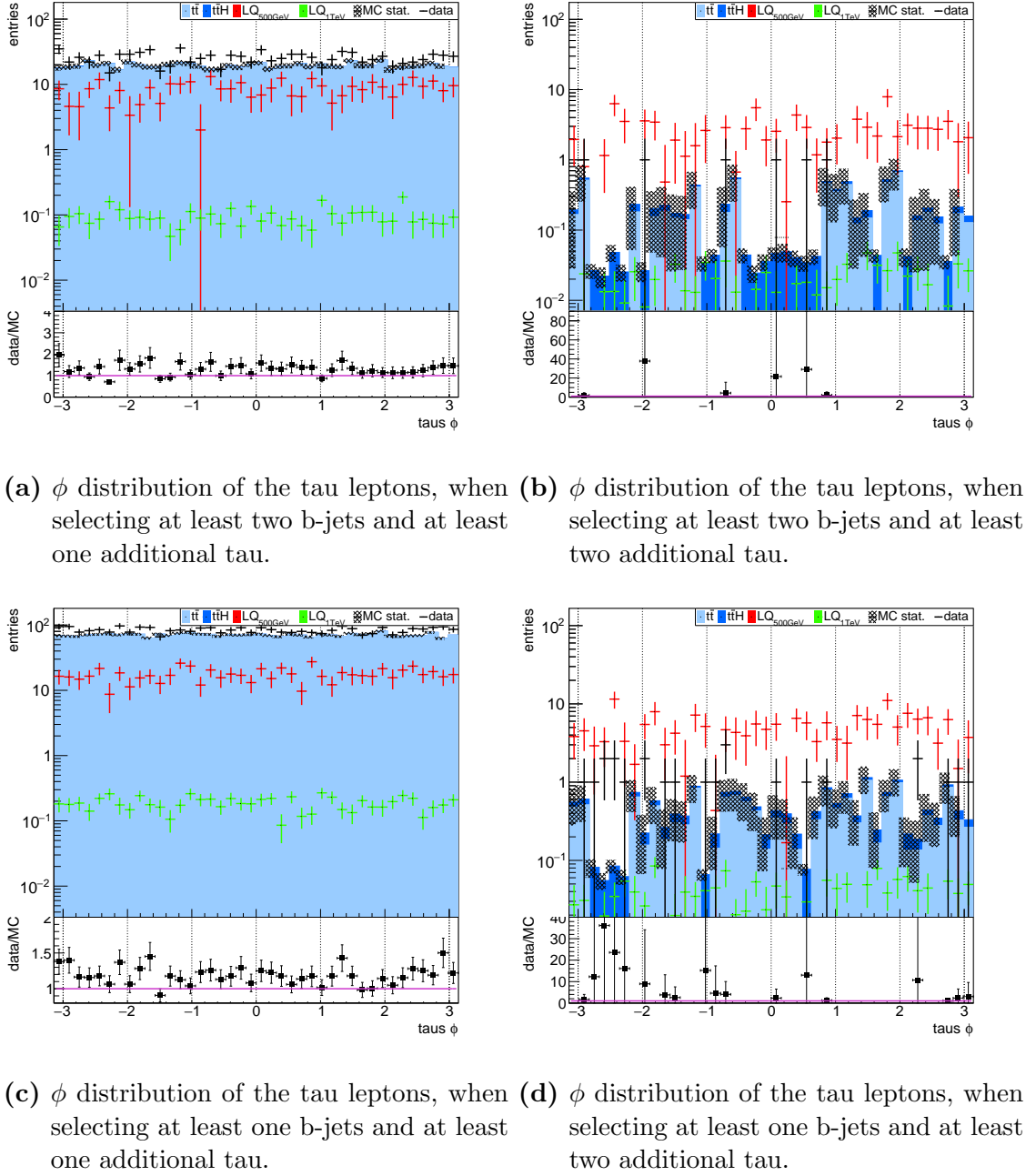


Figure 6.20: Azimuthal angle distribution of all tau leptons for different event selections.

6 Results

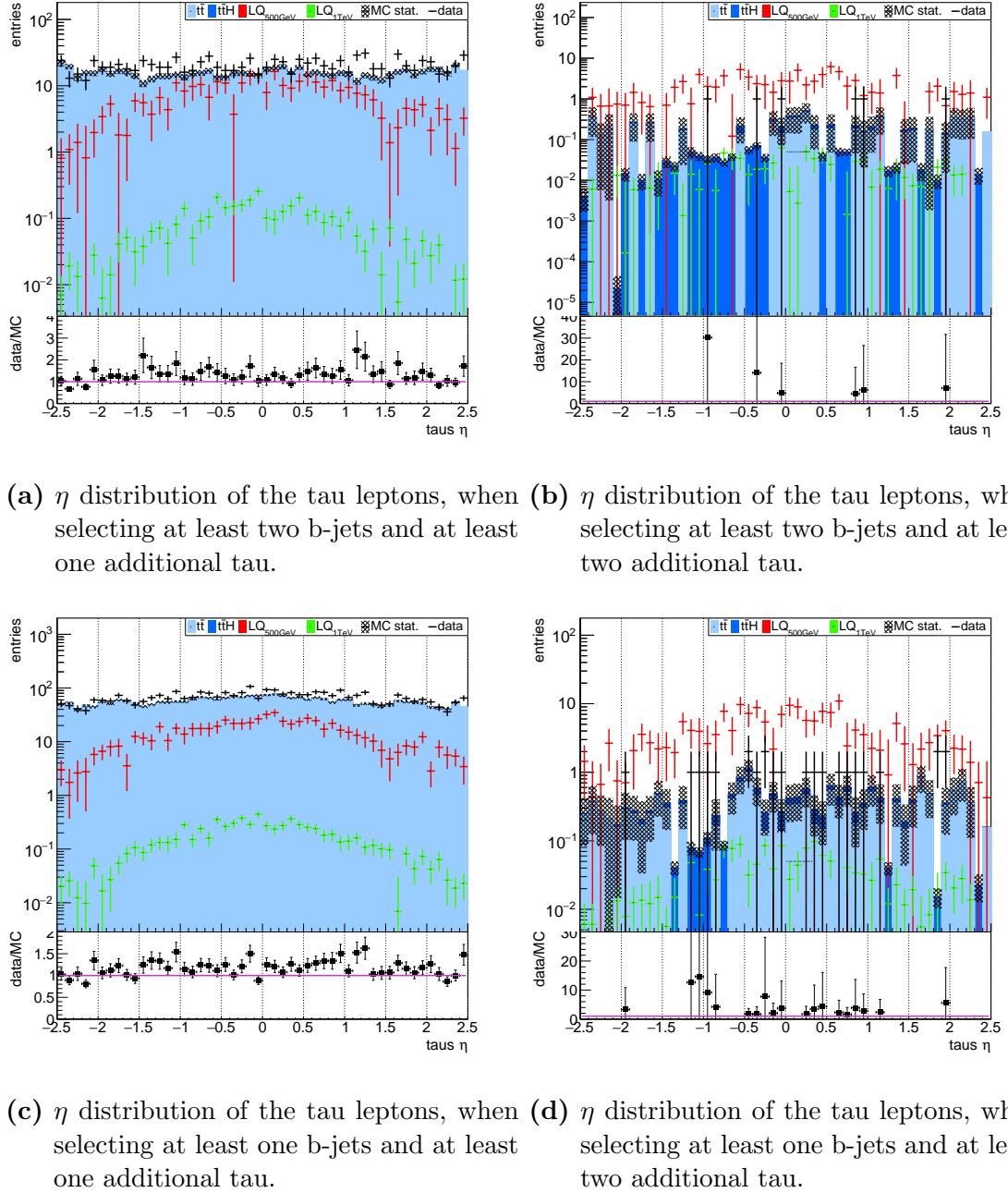
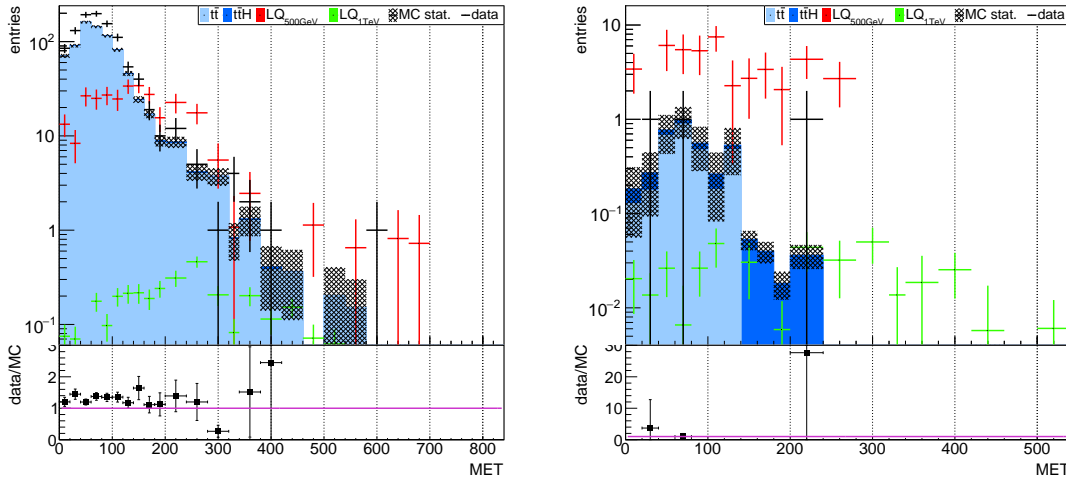
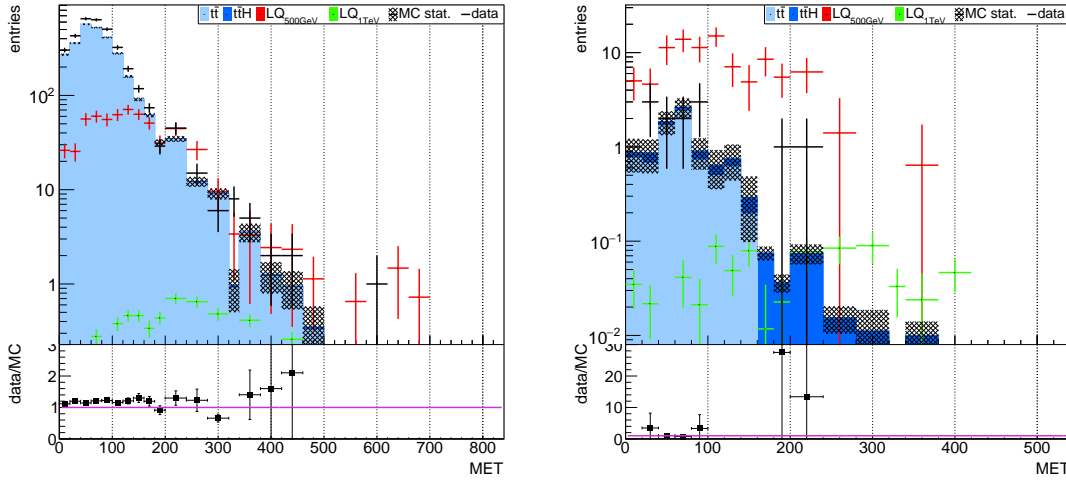


Figure 6.21: Pseudorapidity distribution of all tau leptons for different event selections.



(a) \cancel{E}_T distribution, when selecting at least two b-jets and at least one additional tau.

(b) \cancel{E}_T distribution, when selecting at least two b-jets and at least two additional taus.



(c) \cancel{E}_T distribution, when selecting at least one b-jet and at least one additional tau.

(d) \cancel{E}_T distribution, when selecting at least one b-jet and at least two additional taus.

Figure 6.22: Missing energy distribution for different event selections.

6 Results

at least one tau, which can be explained by the lack of additional contributions. Nevertheless for two tau selection it is a good approximation. The statistics is higher for the selection of at least two b-jets.

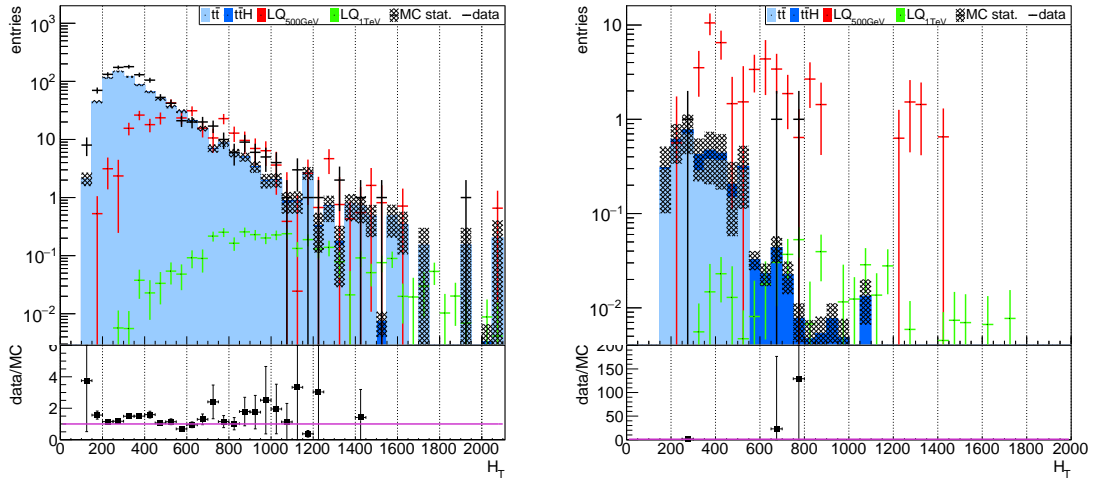
The variable $H_{T,\text{had}}$ in principle shows the same trend as the H_T distribution for a discriminating variable. Nevertheless the effect of extracting the signal is not as good as for H_T . The reason is that less objects are included in the variable. $H_{T,\text{had}}$ only contains the sum of the jets' momenta. The plots are shown in figure 6.24. As a conclusion drawn from the comparison of H_T and $H_{T,\text{had}}$ distribution is that the discrimination is better for variables containing more objects.

The most objects are covered by the S_T variable. Its distribution is shown in figure 6.25. From the findings of the comparison between H_T and $H_{T,\text{had}}$ the choice for the discrimination variable should be S_T . This is confirmed by the fact that it is possible to differentiate between signal and background in the selection of at least one b-jet and at least one tau (see figure 6.25c) as well as in the selection of at least two b-jets and at least one tau (see figure 6.25a). Taking into account at least two tau leptons means an further improvement of the signal selection (see figure 6.25d and 6.25b). As a result the high mass point sample can be distinguished optimally in this selection. Due to its high LQ mass the S_T spectrum reaches high values up to 3.0 TeV.

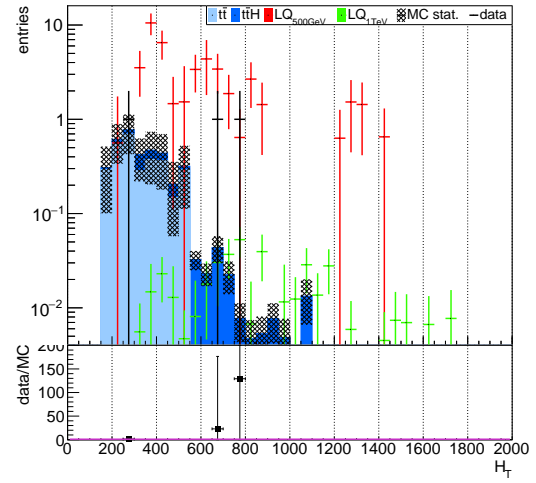
Even excluding the jets in the definition of S_T resulting in the possibly discriminating variable $S_{T,\text{lep}}$ (see figure 6.26), the distribution is also capable to show a difference in signal and background at 400 GeV (see figure 6.26a and 6.26c) in the at least one tau selection of the low mass point LQ sample. But still it is possible to extract the high mass point LQ signal from background in the same selection with at least one tau. The threshold is ~ 1 TeV. The selection of at least two taus gives similar results to that of S_T (see figure 6.26b and 6.26d) with a optimal extraction of the signal samples. From that point of view $S_{T,\text{lep}}$ should be preferred over H_T or the better option is to take S_T .

Minimum and maximum separation ΔR between taus and leptons, taus and jets as well as taus and b-jets within the event selection are partly convenient for a discrimination between signal and background.

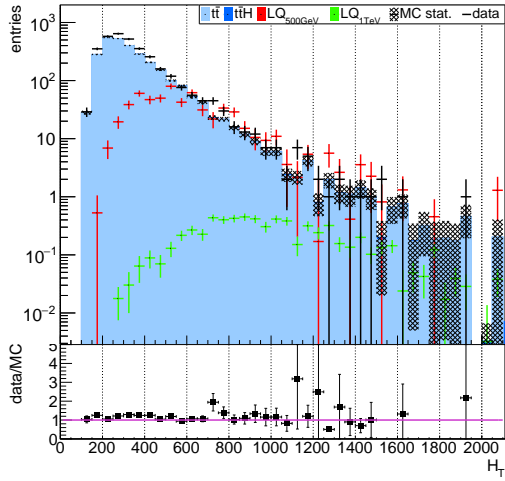
The minimum separation between taus and leptons (electrons and muons) are shown in figure 6.27 for the different selections. The best discrimination can be reached for the selection of at least two tau leptons preferring the case with at least 1-bjet due to sufficient statistics (see figure 6.27b and 6.27d). Nevertheless, in the case of selecting two taus the high mass point LQ signal cannot be extracted from background processes. Within the selection of only one tau both signals are exceeded by background events (see figure 6.27a and 6.27d). The encountered discrepancies



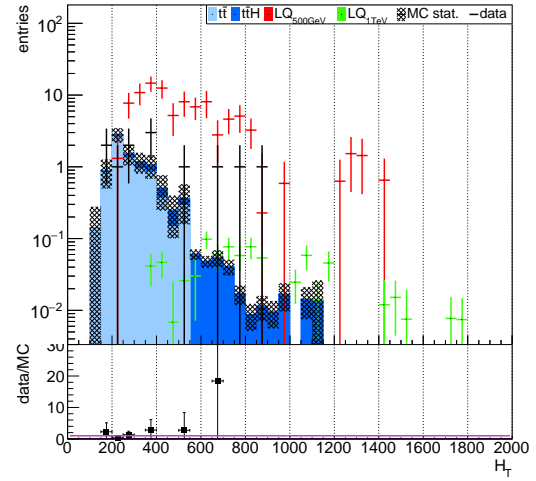
(a) H_T distribution of the tau leptons, when selecting at least two b-jets and at least one additional tau.



(b) H_T distribution of the tau leptons, when selecting at least two b-jets and at least two additional taus.



(c) H_T distribution of the tau leptons, when selecting at least one b-jet and at least one additional tau.



(d) H_T distribution of the tau leptons, when selecting at least one b-jet and at least two additional taus.

Figure 6.23: H_T distribution of the tau lepton for different event selections.

6 Results

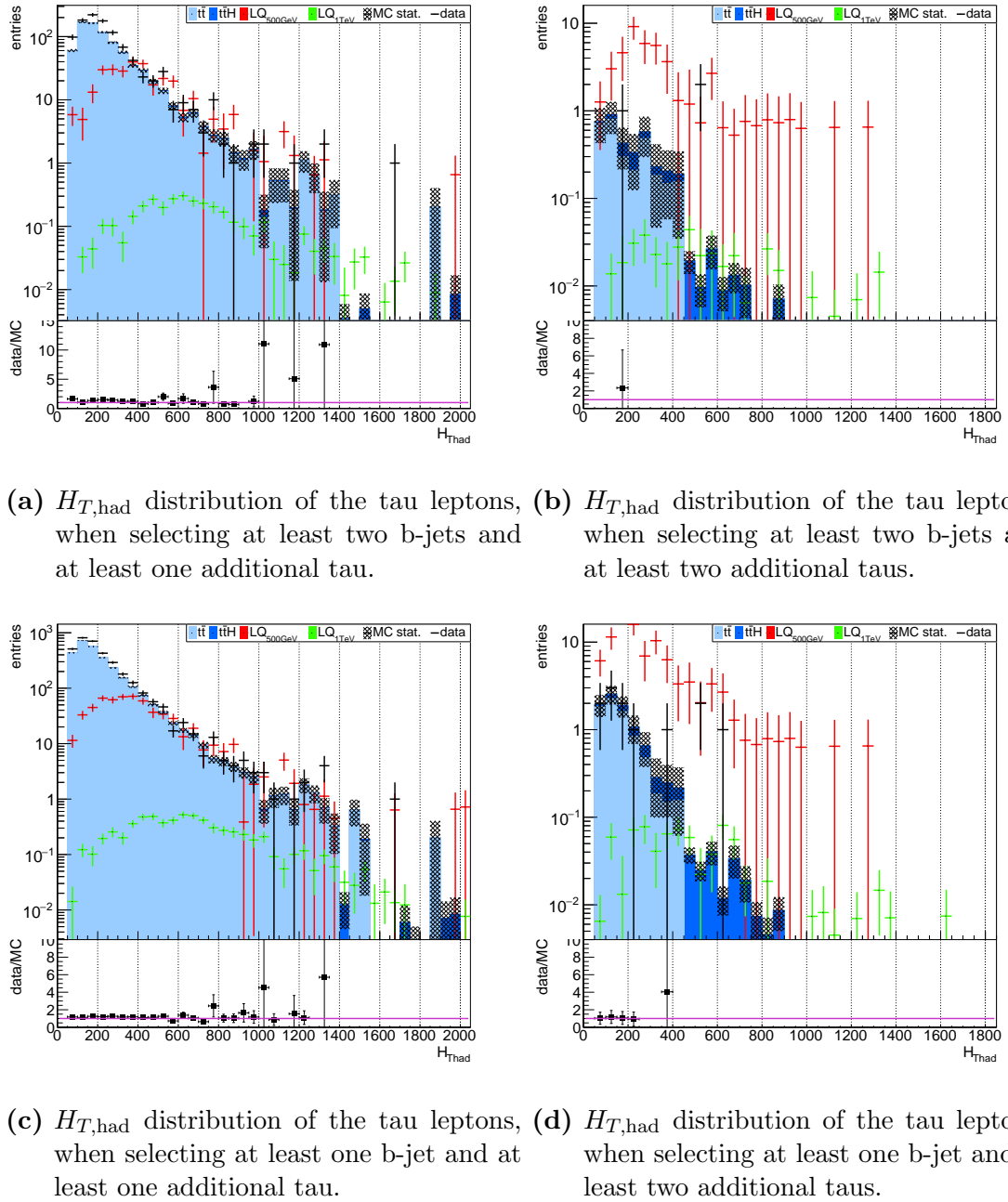


Figure 6.24: $H_{T,\text{had}}$ distribution of the tau lepton for different event selections.

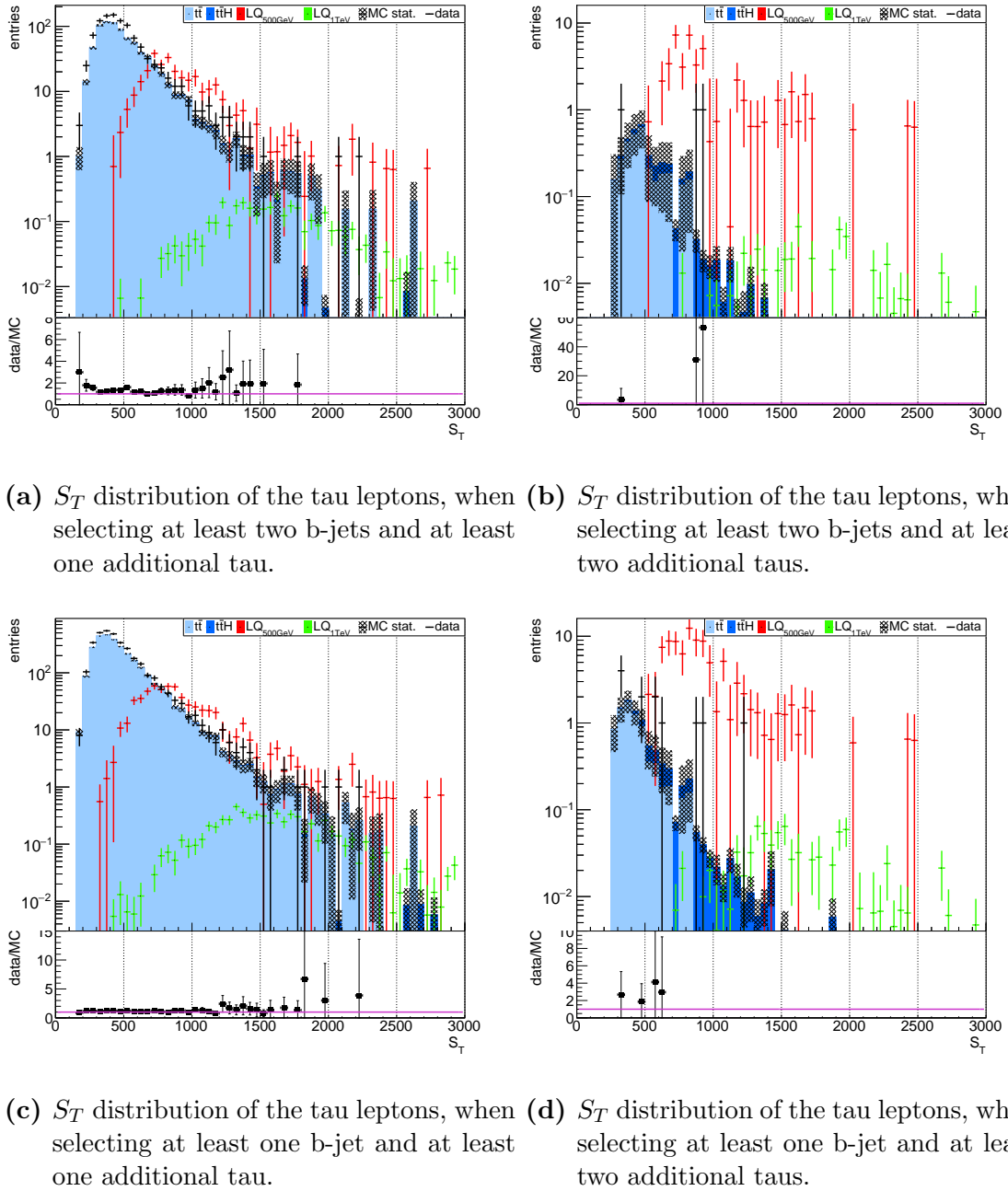
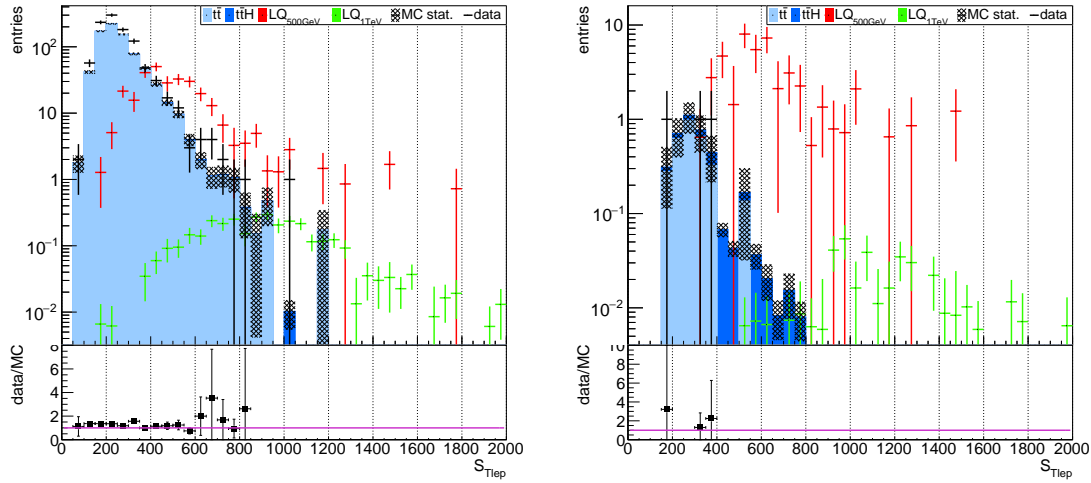


Figure 6.25: S_T distribution of the tau lepton for different event selections.

6 Results



- (a) $S_{T,\text{lep}}$ distribution of the tau leptons, when selecting at least two b-jets and at least one additional tau.
- (b) $S_{T,\text{lep}}$ distribution of the tau leptons, when selecting at least two b-jets and at least two additional taus.

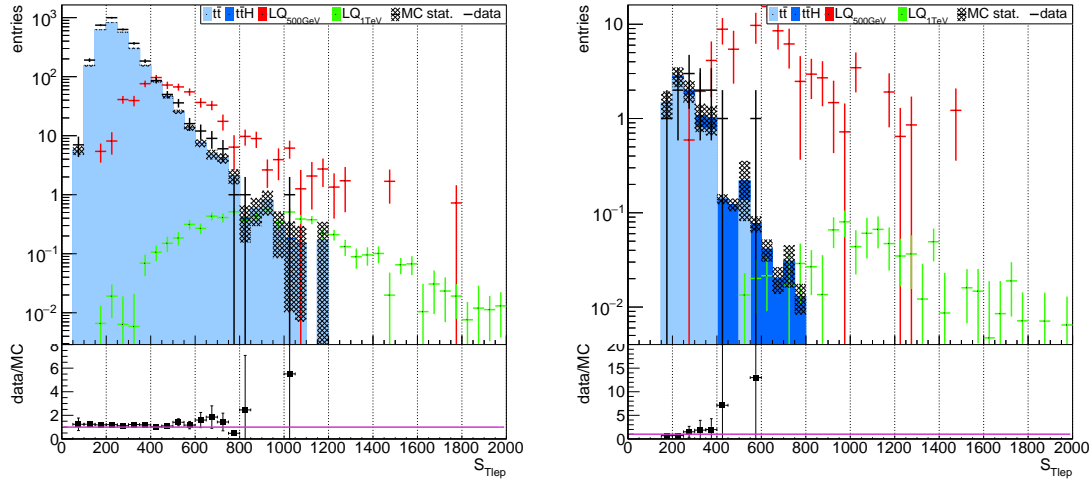


Figure 6.26: $S_{T,\text{lep}}$ distribution of the tau lepton for different event selections.

between data and background MC simulations are present again, which confirms that a small amount of other background contributions is missing in that consideration. More $t\bar{t}H$ events are found in the two tau selection compared to at least one tau, which agrees with the general findings above.

The maximum separation between taus and leptons (electrons and muons) are shown in figure 6.28. The best discrimination between signal and background can be achieved with the selection of at least two taus, but only for the low mass LQ sample. Although this is not the best option compared to S_T variable or the taus' transverse momentum for example.

The minimum and maximum separation between taus and jets as shown in figure 6.29 and 6.30 as discrimination option is also not the best option compared to S_T or tau related distributions. The signal events exceed the background only in the selection with at least two taus for the low mass point LQ signal with the disadvantage of lower statistics. This variable agrees with the findings of the tau and lepton separation.

Following the example of the minimum and maximum separation between taus and jets the separation between taus and b-jets are shown in figure 6.31 and 6.32 and give similar results. Taking this separating variable as discriminant is not the best option due to the low difference between background and high mass point LQ signal.

As a conclusion the findings of this section shows that variables like the tau transverse momentum or the S_T distributions are good candidates for signal extraction and offer the possibility to cut on that values for a signal optimization. In detail this means that the selection of at least two taus should be the choice because of the larger differences in both signal samples compared to the background. The advantage of selecting at least one b-jet is that it provides better statistics compared to the two b-jet case. The background estimation with $t\bar{t}$ and $t\bar{t}H$ agrees with data in case of the two tau selection, which also shows that in this selection the Higgs contributions are more dominant than in selections with less than two taus. Nevertheless some background contributions are missing, which is shown by the selections with less than one tau especially in the low transverse momentum region or the full range of the angular distribution and the separation ΔR .

6 Results

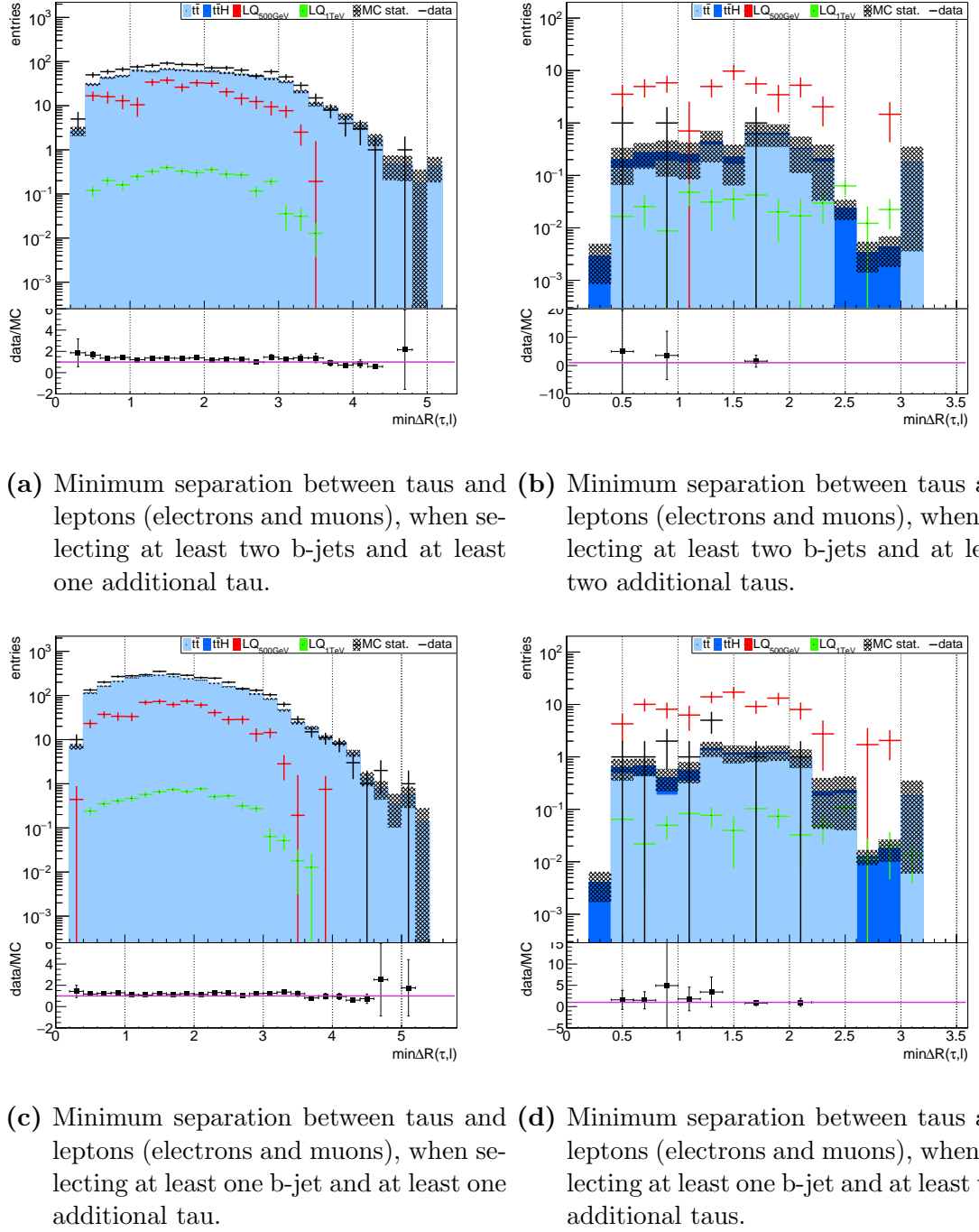
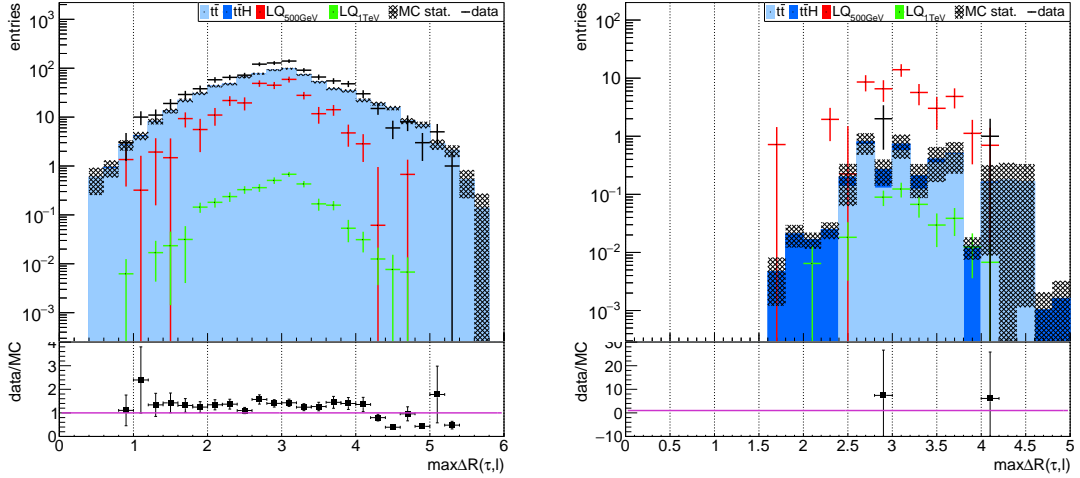
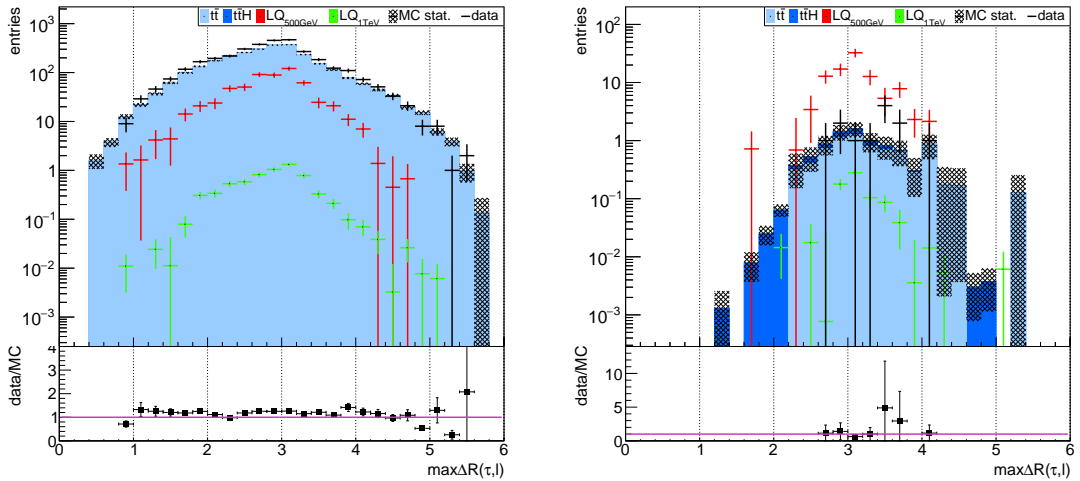


Figure 6.27: Minimum separation between taus and leptons (electrons and muons) for different event selections.



(a) Maximum separation between taus and leptons (electrons and muons), when selecting at least two b-jets and at least one additional tau.

(b) Maximum separation between taus and leptons (electrons and muons), when selecting at least two b-jets and at least two additional taus.



(c) Maximum separation between taus and leptons (electrons and muons), when selecting at least one b-jet and at least one additional tau.

(d) Maximum separation between taus and leptons (electrons and muons), when selecting at least one b-jet and at least two additional taus.

Figure 6.28: Maximum separation between taus and leptons (electrons and muons) for different event selections.

6 Results

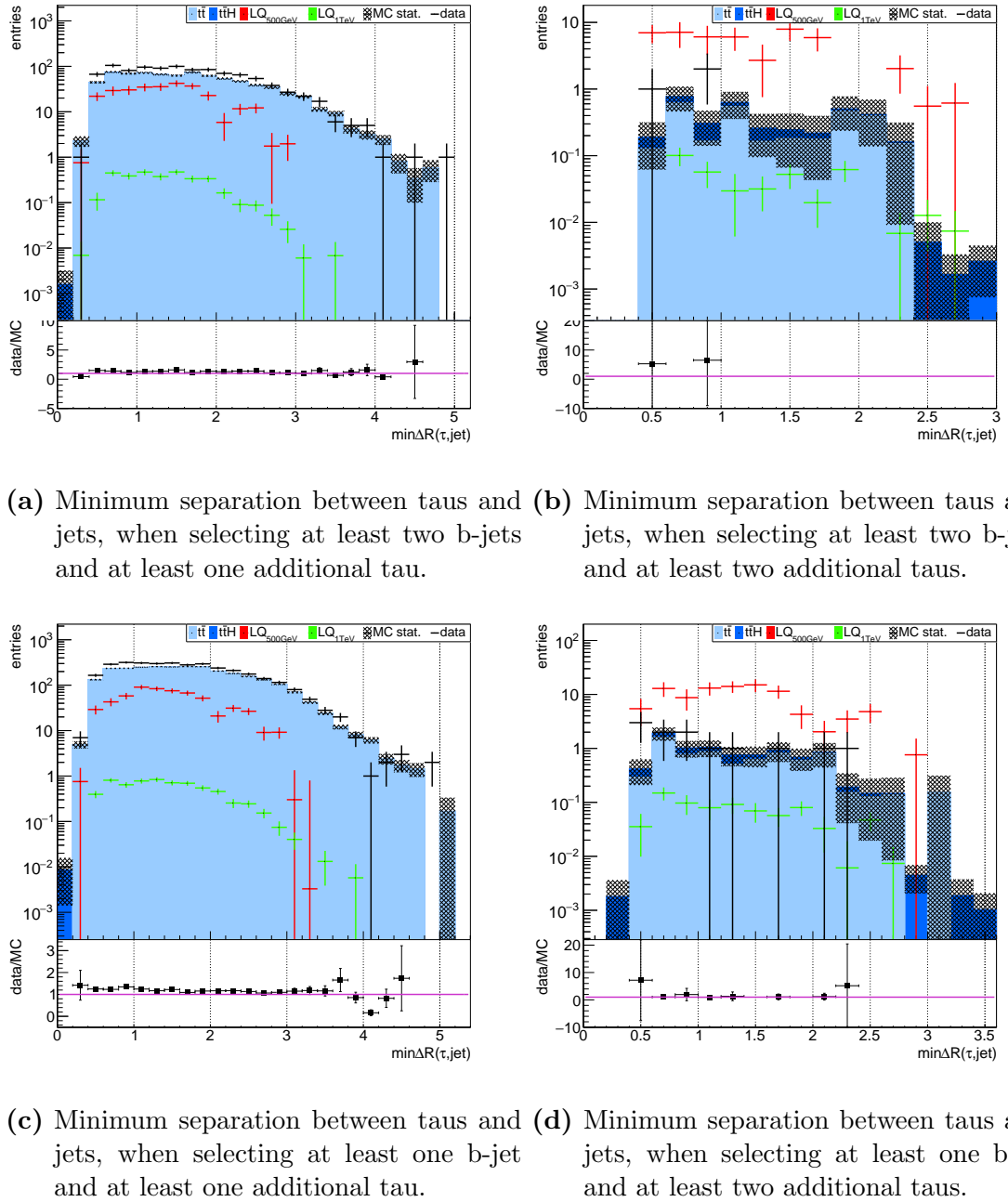
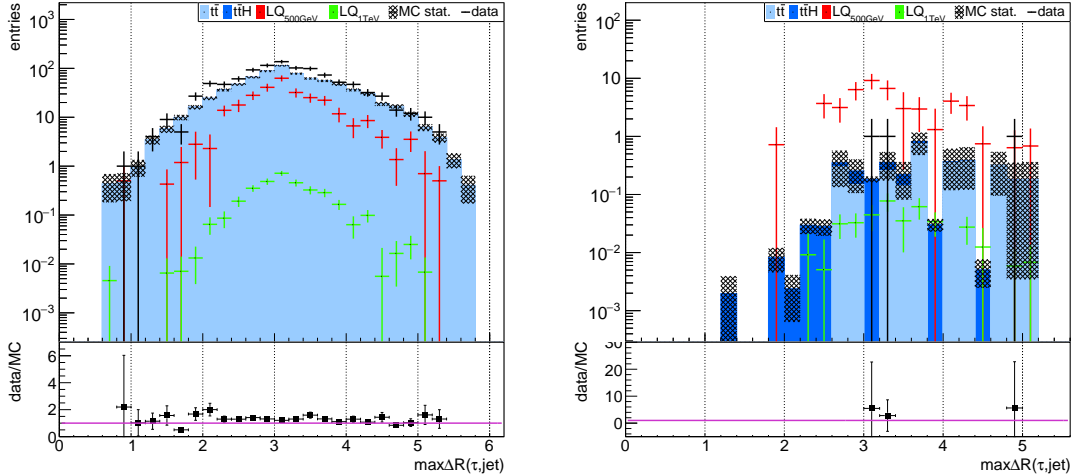
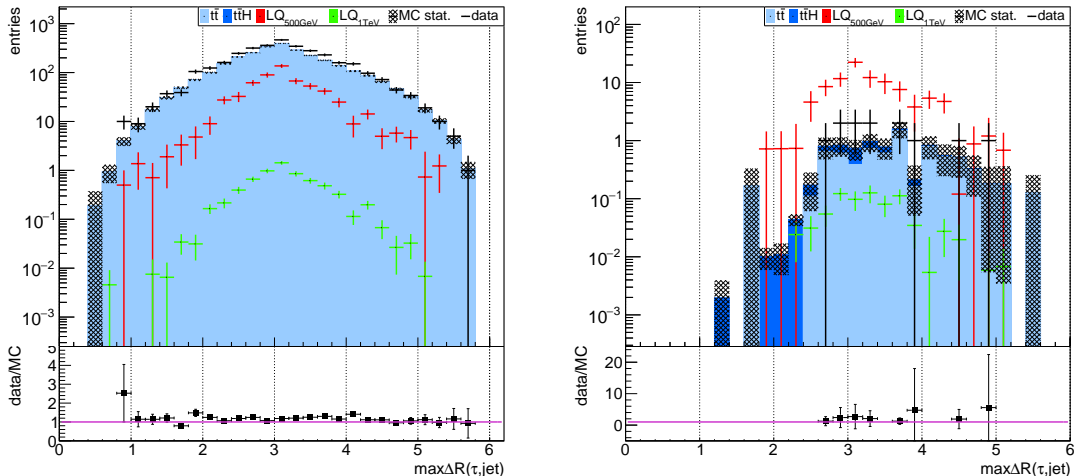


Figure 6.29: Minimum separation between taus and jets for different event selections.



(a) Maximum separation between taus and jets, when selecting at least two b-jets and at least one additional tau.

(b) Maximum separation between taus and jets, when selecting at least two b-jets and at least two additional taus.



(c) Maximum separation between taus and jets, when selecting at least one b-jet and at least one additional tau.

(d) Maximum separation between taus and jets, when selecting at least one b-jet and at least two additional taus.

Figure 6.30: Maximum separation between taus and jets for different event selections.

6 Results

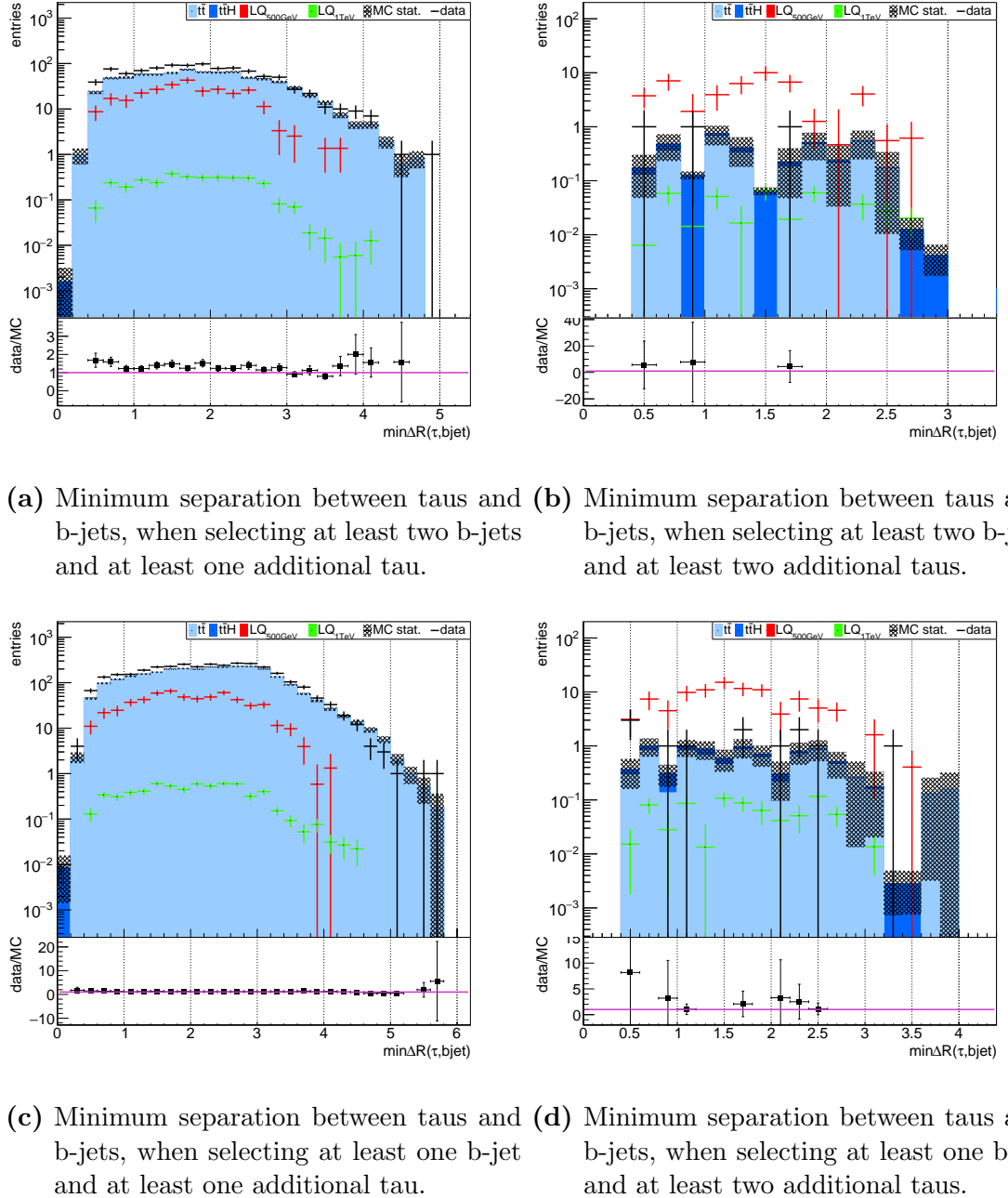
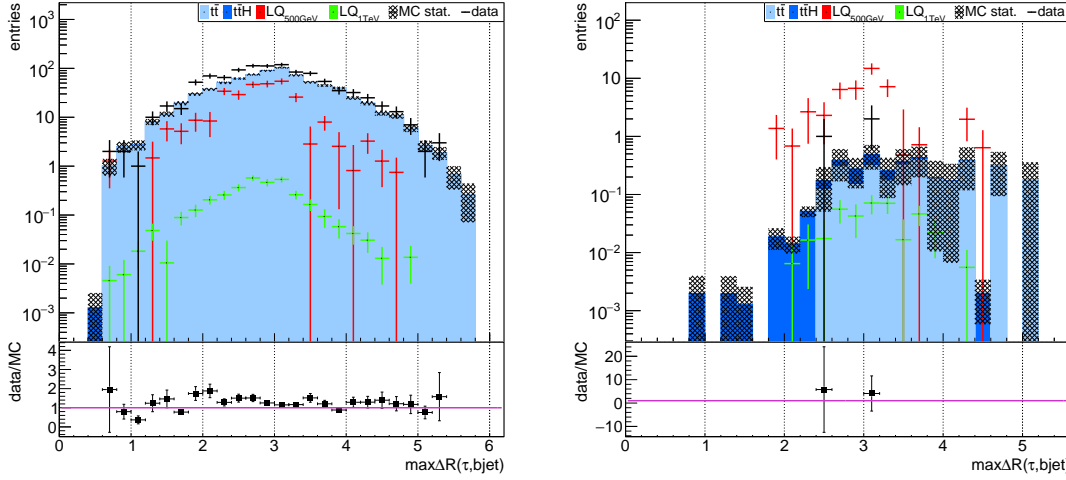
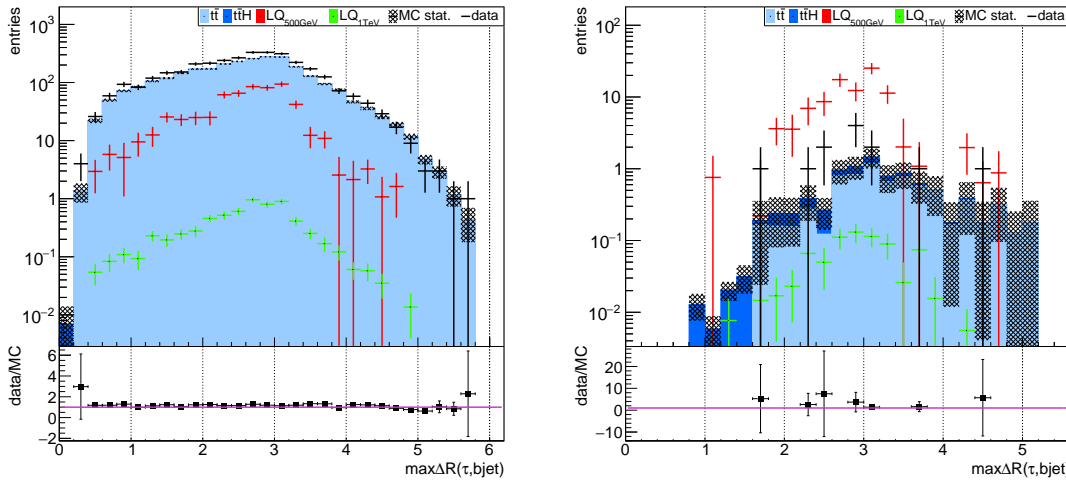


Figure 6.31: Minimum separation between taus and b-jets for different event selections.



(a) Maximum separation between taus and b-jets, when selecting at least two b-jets and at least one additional tau.

(b) Maximum separation between taus and b-jets, when selecting at least two b-jets and at least two additional taus.



(c) Maximum separation between taus and b-jets, when selecting at least one b-jet and at least one additional tau.

(d) Maximum separation between taus and b-jets, when selecting at least one b-jet and at least two additional taus.

Figure 6.32: Maximum separation between taus and b-jets for different event selections.

6.4 Discovery significance

The discovery significance provides a benchmark for a quantitative measurement of the leptoquark signal extraction out of the background contributions. Section 6.3 already showed possible candidates for discriminant variables in the chosen event selection. This chapter gives insight to the discovery significance for the different event selections and shows the variation of the significance by cutting on discriminant variables like the taus' transverse momentum and S_T (cf. eq. (6.6)).

When searching for new physics a certain number of events n is observed, following the Poisson distribution with a mean of $s + b$ that is the number of signal events s and background events b . The discovery significance can be treated as statistical test using the Gaussian p -value with the hypothesis that s becomes a hypothesized number of signal events. This can be achieved by a statistic based on the profile likelihood ratio [87]:

$$\lambda(s) = \frac{L\left(s, \hat{\theta}(s)\right)}{L\left(\hat{s}, \hat{\theta}\right)}. \quad (6.8)$$

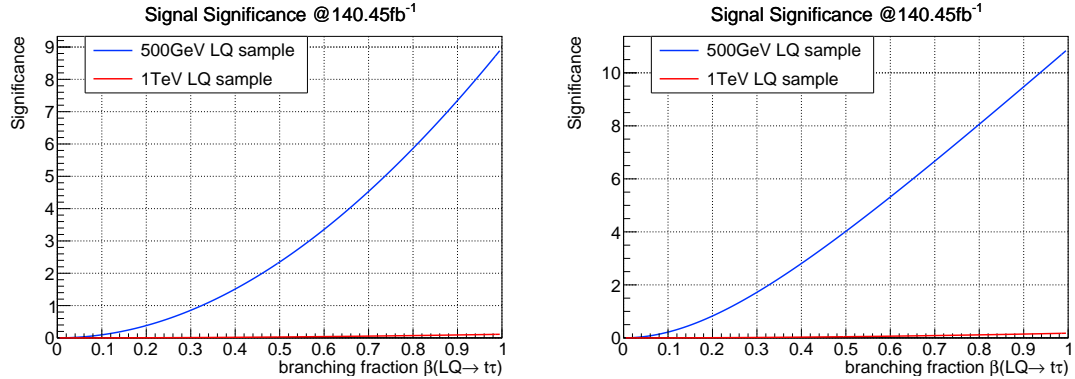
Here $L(s, \theta)$ is the likelihood function, representing the probability for the measurement, under the assumption of the signal parameter s and any additional nuisance parameter θ . The double-hat refers to the nuisance parameter θ that maximize the likelihood for a specific s . Thus, it is the profile likelihood. The denominator is the maximum of the likelihood. [87]

If the number of background events is not known, b can be treated as such nuisance parameter. To further constrain the background events a control measurement with m events can be performed, where the signal is absent. The control measurement follows a Poisson statistic with the mean value of τb . In this context τ represents a scale factor. The resulting likelihood function for that problem is the product [87]:

$$L(s, b) = \frac{(s+b)^n}{n!} e^{-(s+b)} \frac{\tau b}{m!} e^{-\tau b}. \quad (6.9)$$

With the help of Wilks theorem [88] and the replacement of the data values n and m by their expectation values $s + b$ and τb in the *Asimov approximation* gives the expectation significance [87]:

$$Z_A = \sum_{n=0}^N \left[2 \left((s+b) \ln \left[\frac{(s+b)(b+\sigma_b^2)}{b^2 + (s+b)\sigma_b^2} \right] - \frac{b^2}{\sigma_b^2} \ln \left[1 + \frac{\sigma_b^2 s}{b(b+\sigma_b^2)} \right] \right) \right]^{\frac{1}{2}} \quad (6.10)$$



- (a) Discovery significance for the signal LQ samples in the selection of at least two b-jets and at least one additional tau lepton.
- (b) Discovery significance for the signal LQ samples in the selection of at least two b-jets and at least two additional tau leptons.

Figure 6.33: Discovery significance for the signal LQ samples in the selection of at least two b-jets.

with the variance of \hat{b} that maximizes the likelihood given by $\sigma_b^2 = \frac{b}{\tau}$. Here a conservative estimation was made for the background variance and is set to $\sigma_b = 50\%$. If the real variance has a smaller variance the impact of the significance increase would be higher.

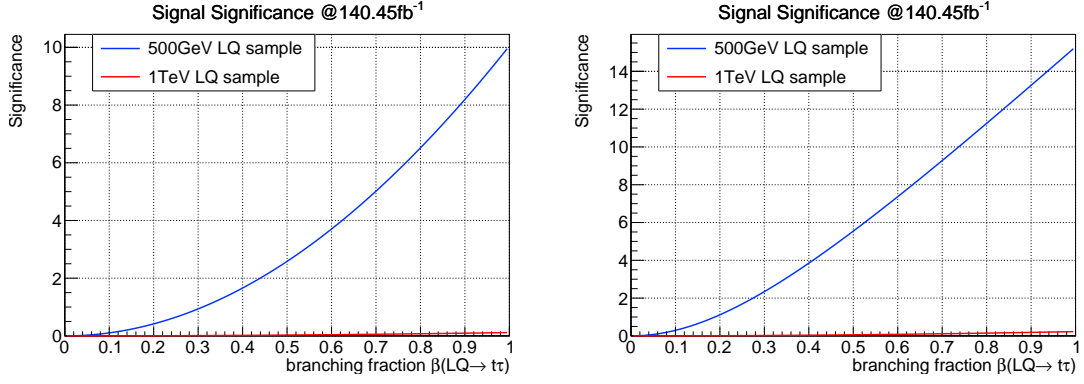
The expected discovery significance for the two leptoquark signal samples are calculated for the different event selection with at least one or two b-jets and at least one or two additional taus (cf. 5.3) in respect to the branching fraction $\beta(LQ \rightarrow t\tau)$ of the leptoquark (cf. section 2.3.2). The used leptoquark MC samples (cf. section 5.1) consider LQ decays with a branching fraction of $\beta = 1$. The following is done in order to obtain the dependency of the significance on the branching ratio and treat β as a free parameter following the basic idea of more generic LQ searches described in section 2.3.2: The relation

$$s(\beta) \propto \sigma \beta (LQ \rightarrow t\tau)^2 \quad (6.11)$$

holds true for the number of signal events $s(\beta)$ at branching fraction $\beta(LQ \rightarrow t\tau)$ and the given cross section σ . The square of the branching ratio is valid, because leptoquark pairs are considered as signal events. According to eq. (6.11), the case of $\beta = 1$ results in $s(\beta = 1) \propto \sigma$. Considering the previous two findings and taking the branching ratio as free parameter, the number of signal events becomes $s(\beta) \propto s(\beta = 1)\beta^2$ for the general case.

The discovery significance for the signal samples in the selection of at least two b-jets is shown in 6.33. The significance follows the expected parabola curve and is greatest for the branching fraction with no further decay modes ($\beta = 1$). Due to

6 Results



- (a) Discovery significance for the signal LQ samples in the selection of at least one b-jet and at least one additional tau lepton.
- (b) Discovery significance for the signal LQ samples in the selection of at least one b-jet and at least two additional tau leptons.

Figure 6.34: Discovery significance for the signal LQ samples in the selection of at least one b-jet.

the small production cross sections in the high mass point LQ sample the significance is very low compared to the low mass point sample. The discovery significance when selecting at least one tau is 9.7 and 0.12 for the low and the high mass point respectively (see fig. 6.33a). As the plots showed in section 6.3 the selection with at least two taus increases the significance, although the increase in figure 6.33b is marginally (12 and 0.18). This can be explained by the general decrease of statistics due to the tight cut requiring at least two b-jets. Figure 6.34 with its selection of at least one b-jet stands in comparison to this with higher statistics. The significance is as high as 11 and 0.13 for the 500 GeV LQ mass point and the 1 TeV LQ mass point respectively. This is valid for the additional selection of at least one tau lepton (see fig. 6.34a). Selecting at least two additional taus creates a significance shown in figure 6.34b. The looser selection with at least one b-jet agrees with the results of section 6.3. The discovery significance is higher compared to the two b-jet selection. For selecting at least two tau the significance is 17 and 0.24 for the low and high mass point respectively (see fig. 6.34b).

In agreement with section 6.3 the highest significance for the LQ signal can be observed with selecting at least one b-jet and additionally at least two tau leptons.

The next step is to search for cuts on kinematic variables to further improve the signal significance. This work presents a first approach for signal optimization in the variables S_T (cf. eq. (6.6)) and in the taus' transverse momentum. In order to find optimal cut values the significance depending on the cut threshold is calculated. Figure 6.35 shows the significance varied by different cut values on the taus' p_T for

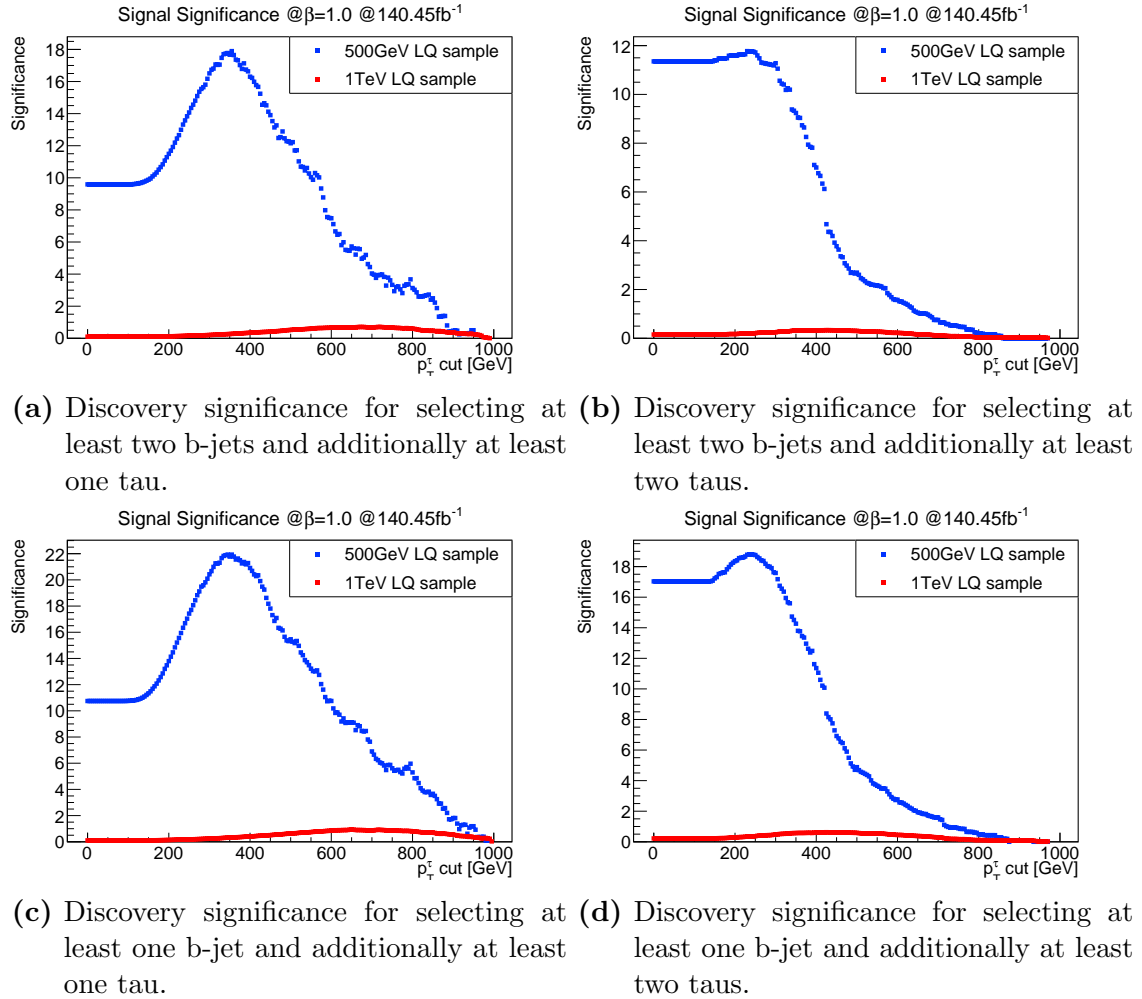


Figure 6.35: Discovery significance depending on the taus' transverse momentum cut value for different event selections at a branching fraction of $\beta = 1$.

6 Results

the different event selections. The cut thresholds are divided in steps of 5 GeV. When selecting at least two b-jets and at least one tau a cut at 355 GeV (see fig. 6.35a) increases the significance up to 22 for signal sample with mass point 500 GeV. An increase of significance is reached for the 1 TeV LQ sample up to 0.92 with a transverse momentum cut of 655 GeV. For the selection of at least two b-jets and at least two taus the increase of significance up to 19 is achieved with a cut at 240 GeV and up to 0.63 with a cut at 425 GeV for the low and high mass point respectively (see fig. 6.35b). Increased significance of 18 and 0.71 is observed for the selection of at least one b-jet and at least one tau lepton, if p_T is cut at 355 GeV and 715 GeV for the low and high mass point sample respectively (see fig. 6.35c). Correspondingly, the discovery significance is greatest with 12 and 0.34 with a 230 GeV and 425 GeV cut, when selecting at least one b-jet and at least two taus (see fig. 6.35d).

Figure 6.36 shows the significance varied by different S_T cut values (see eq. (6.6)) for the different event selections. The cut thresholds are divided in steps of 10 GeV. The significance reaches values of 22 and 1.1 at S_T cuts of 710 GeV and 1430 GeV in the selection of at least two b-jets and at least one tau lepton (see fig. 6.36a). This corresponds to the low and high LQ signal sample. For the selection with at least two b-jets and two tau leptons the increase of the discovery significance is up to 19 and 0.68 at 470 GeV and 850 GeV cuts (see fig. 6.35b). In case of at least one b-jet and at least one tau lepton the increase of significance is up to 18 and 0.71 at cuts based on 710 GeV and 1430 GeV for the low and high mass point sample respectively (see fig. 6.35c). Cuts on S_T of 460 GeV and 840 GeV result in an increase of up to 12 and 0.39 in the discovery significance (see fig. 6.35d).

The general trend is that within a chosen b-jet selection the significance reaches higher values in the one tau selection compared to the two tau selection. This can be explained by higher available statistics in that specific selection. The difference of the b-jet selection shows that selecting at least one b-jet results in higher significance values due to the looser nature of that requirement. At the same time the significance is already at high values with the two tau selection. Table 6.5 summarizes all significance increases for the different selections and the two kinematic variables. Sudden downward changes in the significance curve can be explained by a sudden drop of signal and background events at the same time. Limit considerations of eq. (6.10) show that $\lim_{b \rightarrow 0} Z_A = \lim_{s \rightarrow 0} Z_A = 0$. Local maxima are the result of a sudden drop of background events, whereas the signal events are constant, e.g. no $t\bar{t}$ background for high p_T (S_T).

The transverse momentum and the variable S_T are good discriminant variables providing high discovery significance for at least the low mass point LQ sample within the chosen event selection. This covers at least one b-jet and at least two tau leptons. Due to the low cross section for the 1 TeV LQ sample the significance with at maximum 1 is not as high as expected. Taking the tau p_T and S_T at

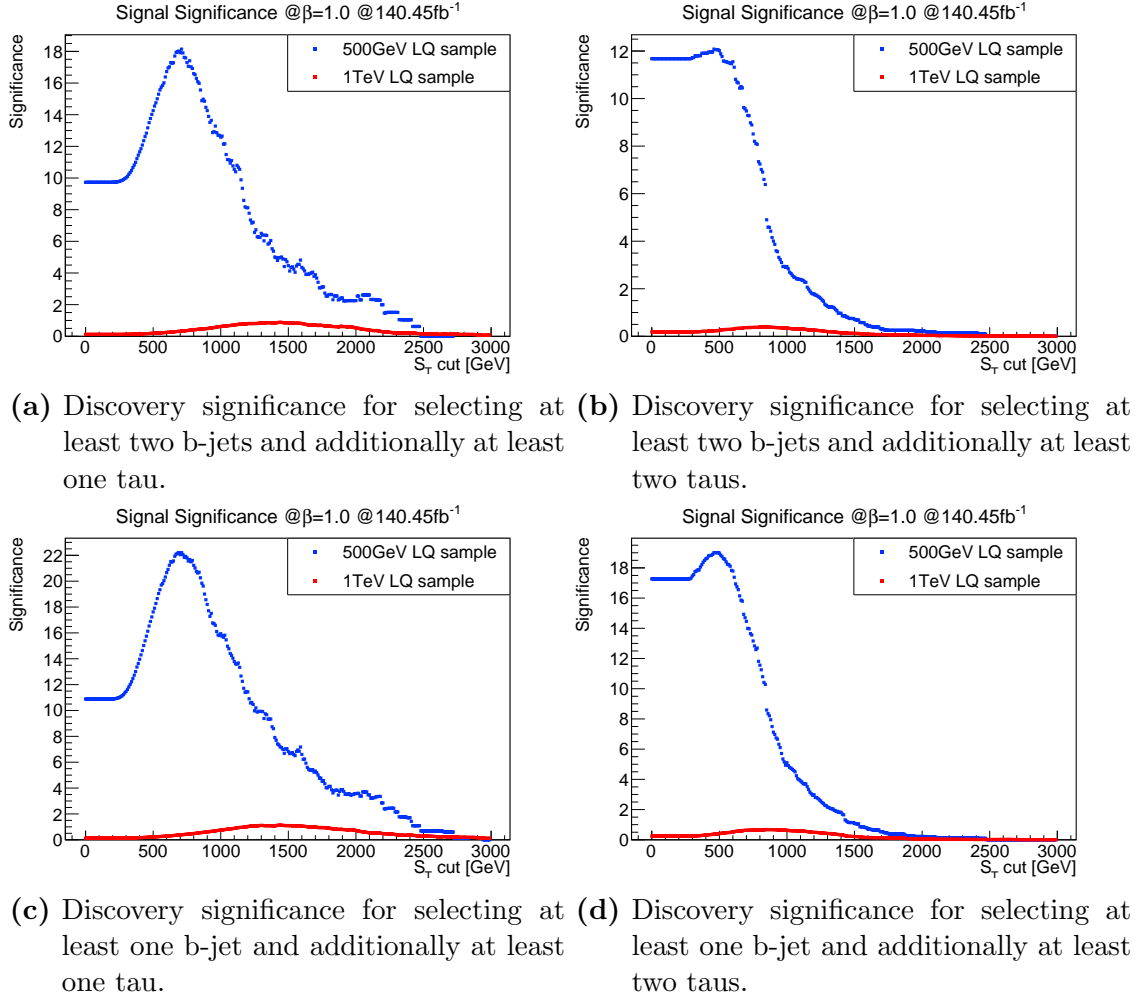


Figure 6.36: Discovery significance depending on S_T (see eq. (6.6)) cut value for different event selections at a branching fraction of $\beta = 1$.

6 Results

selection	LQ sample	kinematic variable variable	increased significance value	cut/GeV
≥ 2 b-jets + $\geq 1 \tau$	500 GeV mass point	p_T	18	355
	1 TeV mass point	p_T	0.71	715
	500 GeV mass point	S_T	18	710
	1 TeV mass point	S_T	0.88	1430
≥ 2 b-jets + $\geq 2 \tau$	500 GeV mass point	p_T	12	230
	1 TeV mass point	p_T	0.34	425
	500 GeV mass point	S_T	12	460
	1 TeV mass point	S_T	0.39	840
≥ 1 b-jets + $\geq 1 \tau$	500 GeV mass point	p_T	22	355
	1 TeV mass point	p_T	0.92	655
	500 GeV mass point	S_T	22	710
	1 TeV mass point	S_T	1.1	1430
≥ 1 b-jets + $\geq 2 \tau$	500 GeV mass point	p_T	19	240
	1 TeV mass point	p_T	0.63	425
	500 GeV mass point	S_T	19	470
	1 TeV mass point	S_T	0.68	850

Table 6.5: Overview of the discovery significance increase in the kinematic variables transverse momentum of all reconstructed taus p_T and S_T for the different event selections.

the same time as parameter θ in eq. (6.8) would further increase the discovery significance.

Conclusion

The tau reconstruction efficiency and fake rate study shows that the background contributions contaminating the potential leptoquark signal in the $t\tau^- + \bar{t}\tau^+$ channel can be approximated by contributions mainly from $t\bar{t}$ and $t\bar{t}H$ processes within the chosen event selection. Measured data are best resembled by these two background samples especially for the selection of at least two tau leptons. Fake candidates like jets faking a hadronic tau show a strong jet p_T dependence on the fake rate. Tau reconstruction efficiencies for the leptoquark signal sample leads to the conclusion that the efficiency only slightly depends on the taus' p_T , whereas the minimum and maximum separation between taus and different objects like jets, b-jets or leptons show an efficiency dependence. One step further would be to include systematic uncertainties into the efficiency and fake study as well as additional background processes for more accuracy.

Various kinematic distributions of data in comparison to the simulated background events and the simulated leptoquark events within the performed selections revealed insight to the signal extraction. The best option is to choose the selection with at least one b-jet and additional tau leptons, where more events survive in order to contribute to higher statistics compared to the selections of at least two b-jets and additional taus. Promising variables to further apply cuts on are the reconstructed taus p_T or S_T distribution. Furthermore the study of kinematic distributions revealed that the proportion of dominant $t\bar{t}H$ events increases with the selection of at least two tau leptons.

Insight to the discovery significance is given for both simulated leptoquark events based on the above mentioned variables p_T and S_T . Within the chosen event selection the discovery significance for the low mass point sample reaches values of 17. Further steps would include a more detailed study of the proposed cuts to increase the signal significance first and foremost also for the high mass point leptoquarks with their low production cross section. To do so a maximum likelihood ratio taking the reconstructed tau p_T and S_T at the same time as parameter would be a step towards a discovery significance increase. A full search strategy for the leptoquarks with the decay characteristics of $t\tau^- + \bar{t}\tau^+$ would involve clear definitions of signal,

7 Conclusion

background and control regions, although the selection of different b-jet and tau multiplicity as well as variations of the requirement opposite and same sign leptons provides diverse definition possibilities for such a task.

List of Figures

2.1	Overview of the Standard Model.	14
2.2	Feynman diagrams of leptoquark pair production processes at proton-proton colliders like the LHC.	21
2.3	Feynman diagram of a leptoquark decay governed by Yukawa coupling. .	22
2.4	Upper limits of the product of the cross section and β^2 depending on the leptoquark mass for the $t\tau^-\bar{t}\tau^+$ channel.	23
2.5	Leptonic and hadronic top decay.	24
2.6	Branching fractions of top-pairs.	25
3.1	Schematic of the CERN accelerator complex.	28
3.2	Structure of the ATLAS detector and the coordinate system.	31
4.1	Tracks in a b-jet.	39
4.2	Light-flavor (a) and c-jet rejection (b) versus b-jet efficiency for the MV2c10 tagger.	40
5.1	Feynman diagrams showing the dominant top-pair production at the LHC.	44
5.2	Higgs production associated with a top-quark pair.	45
5.3	Overview of the event selection.	50
6.1	Estimation of a jet faking a tau lepton for the background events. . .	56
6.2	Estimation of a b-jet faking a tau lepton for the background events. .	57
6.3	Estimation of a light-jet faking a tau lepton for the background events. .	58
6.4	Efficiency of taus originating from Higgs bosons.	60
6.5	Efficiency of taus originating from Higgs bosons for events from $t\bar{t}H$ sample.	61
6.6	Efficiency of taus originating from Higgs bosons for events from $t\bar{t}H$ sample.	62
6.7	Efficiency of taus originating from Higgs bosons depending on the number of jets.	63
6.8	Efficiency of taus originating from Higgs bosons for the separation between taus and leptons.	63

6.9	Efficiency of taus originating from Higgs bosons for the separation between taus and jets.	64
6.10	Efficiency of taus originating from Higgs bosons for the separation between taus and b-jets.	66
6.11	Efficiency of taus originating LQs for the low mass LQ signal events.	67
6.12	Efficiency of taus originating LQs for the high mass LQ signal events.	68
6.13	Efficiency of taus originating from leptoquarks for the LQ signal events.	70
6.14	Efficiency of taus originating from leptoquarks for the LQ signal events.	71
6.15	Efficiency of taus originating from LQs depending on the number of jets.	72
6.16	Efficiency of separation between taus originating from LQs and leptons.	73
6.17	Efficiency of separation between taus originating from LQs and jets.	74
6.18	Efficiency of separation between taus originating from LQs and b-jets.	75
6.19	Transverse momentum distribution of all tau leptons for different event selections.	77
6.20	Azimuthal angle distribution of all tau leptons for different event selections.	79
6.21	Pseudorapidity distribution of all taus lepton for different event selections.	80
6.22	Missing energy distribution for different event selections.	81
6.23	H_T distribution of the tau lepton for different event selections.	83
6.24	$H_{T,\text{had}}$ distribution of the tau lepton for different event selections.	84
6.25	S_T distribution of the tau lepton for different event selections.	85
6.26	$S_{T,\text{lep}}$ distribution of the tau lepton for different event selections.	86
6.27	Minimum separation between taus and leptons (electrons and muons) for different event selections.	88
6.28	Maximum separation between taus and leptons (electrons and muons) for different event selections.	89
6.29	Minimum separation between taus and jets for different event selections.	90
6.30	Maximum separation between taus and jets for different event selections.	91
6.31	Minimum separation between taus and b-jets for different event selections.	92
6.32	Maximum separation between taus and b-jets for different event selections.	93
6.33	Discovery significance for the signal LQ samples in the selection of at least two b-jets.	95
6.34	Discovery significance for the signal LQ samples in the selection of at least one b-jet.	96
6.35	Discovery significance depending on the taus' transverse momentum cut value.	97
6.36	Discovery significance depending on the S_T cut value.	99

List of Tables

2.1	Lie symmetry groups of the Standard Model.	11
2.2	Overview of elementary particles with some selected properties.	13
2.3	Overview of the scalar and vector leptoquarks proposed by the minimal-Buchmüller-Rückl-Wyler model.	18
2.4	Main decay modes of τ^- .	26
5.1	Integrated luminosity for the data-taking periods 2015-2018.	46
5.2	List of single electron triggers.	48
5.3	List of single muon triggers.	49
6.1	Observed and predicted event yield for the event selection.	52
6.2	Fake rates for the $t\bar{t}$ and the $t\bar{t}H$ sample.	55
6.3	Efficiencies for the $t\bar{t}H$ sample.	57
6.4	Efficiencies for the two LQ samples with 500 GeV and 1 TeV mass point.	65
6.5	Overview of the discovery significance increase in the kinematic variables p_T and S_T for the different event selections.	100

Bibliography

- [1] Robert Mann. *An Introduction to Particle Physics and the Standard Model* -. CRC Press, Boca Raton, Fla, 2011.
- [2] V. Parameswaran Nair. *Concepts in Particle Physics - A Concise Introduction to the Standard Model*. World Scientific Publishing Company, Singapore, 2017.
- [3] Ian Brock and Thomas Schörner-Sadenius. *Physics at the Terascale*. Wiley, New York, 2011.
- [4] W. N. Cottingham and D. A. Greenwood. *An Introduction to the Standard Model of Particle Physics* -. Cambridge University Press, Cambridge, 2007.
- [5] David Griffiths. *Introduction to Elementary Particles* -. Wiley, New York, 2. aufl. edition, 2008.
- [6] M. Tanabashi et al. Review of particle physics. *Phys. Rev. D*, 98:030001, Aug 2018.
- [7] Maksym Teklishyn. Measurement of the η c (1s) production cross-section via the decay η c to proton-antiproton final state. 09 2014.
- [8] Y. Fukuda et al. Evidence for oscillation of atmospheric neutrinos. *Phys. Rev. Lett.*, 81:1562–1567, Aug 1998.
- [9] Q. R. Ahmad et al. Direct evidence for neutrino flavor transformation from neutral-current interactions in the sudbury neutrino observatory. *Phys. Rev. Lett.*, 89:011301, Jun 2002.
- [10] G. L. Fogli, E. Lisi, A. Marrone, D. Montanino, A. Palazzo, and A. M. Rotunno. Global analysis of neutrino masses, mixings and phases: entering the era of leptonic CP violation searches. *Phys. Rev.*, D86:013012, 2012.

- [11] Claus Kiefer. *Quantum Gravity* -. OUP Oxford, New York, London, 3rd edition, 2007.
- [12] Andrew Fowlie, Csaba Balazs, Graham White, Luca Marzola, and Martti Raidal. Naturalness of the relaxion mechanism. *JHEP*, 08:100, 2016.
- [13] Prasad Hegde, Karl Jansen, C. J. David Lin, and Attila Nagy. Stabilizing the electroweak vacuum by higher dimensional operators in a Higgs-Yukawa model. *PoS*, LATTICE2013:058, 2014.
- [14] Steven Weinberg. Implications of dynamical symmetry breaking. *Phys. Rev. D*, 13:974–996, Feb 1976.
- [15] J D Vergados. *The Standard Model and Beyond* -. World Scientific Publishing Company, Singapore, 2017.
- [16] Yorikiyo Nagashima. *Beyond the Standard Model of Elementary Particle Physics* -. John Wiley & Sons, New York, new. edition, 2014.
- [17] Masahiro Kuze and Yves Sirois. Search for particles and forces beyond the standard model at HERA ep and Tevatron $p\bar{p}$ colliders. *Prog. Part. Nucl. Phys.*, 50:1–62, 2003. [Erratum: Prog. Part. Nucl. Phys. 53, 583(2004)].
- [18] Hisaki Hatanaka, Takeo Inami, and C. S. Lim. The Gauge hierarchy problem and higher dimensional gauge theories. *Mod. Phys. Lett.*, A13:2601–2612, 1998.
- [19] W. de Boer. Grand unified theories and supersymmetry in particle physics and cosmology. *Prog. Part. Nucl. Phys.*, 33:201–302, 1994.
- [20] R. N. Mohapatra. Neutrino mass and grand unification. *Phys. Scripta*, T121:185–191, 2005.
- [21] Howard Georgi and S. L. Glashow. Unity of all elementary-particle forces. *Phys. Rev. Lett.*, 32:438–441, Feb 1974.
- [22] Donald H. Perkins. *Introduction to High Energy Physics* -. Cambridge University Press, Cambridge, 4th edition, 2000.
- [23] Goran Senjanovic. Proton decay and grand unification. *AIP Conf. Proc.*, 1200:131–141, 2010.

Bibliography

- [24] K. Kobayashi et al. Search for nucleon decay via modes favored by supersymmetric grand unification models in Super-Kamiokande-I. *Phys. Rev.*, D72:052007, 2005.
- [25] John C. Baez and John Huerta. The Algebra of Grand Unified Theories. *Bull. Am. Math. Soc.*, 47:483–552, 2010.
- [26] Jogesh C. Pati and Abdus Salam. Lepton number as the fourth "color". *Phys. Rev. D*, 10:275–289, Jul 1974.
- [27] JoAnne L. Hewett and Thomas G. Rizzo. Low-energy phenomenology of superstring-inspired e6 models. *Physics Reports*, 183(5):193 – 381, 1989.
- [28] Hesselbach, S., Franke, F., and Fraas, H. Neutralinos in E6 inspired supersymmetric U(1)' models. *Eur. Phys. J. C*, 23(1):149–162, 2002.
- [29] W. Buchmüller and R. Rückl and D. Wyler. Leptoquarks in lepton-quark collisions. *Physics Letters B*, 191(4):442 – 448, 1987.
- [30] Michael E. Peskin and Daniel V. Schroeder. *An Introduction to Quantum Field Theory* -. Addison-Wesley Publishing Company, Reading, 1995.
- [31] Bastian Diaz, Martin Schmaltz, and Yi-Ming Zhong. The leptoquark Hunter's guide: Pair production. *JHEP*, 10:097, 2017.
- [32] J. L. Hewett and S. Pakvasa. Scalar-leptoquark production at hadron colliders. *Phys. Rev. D*, 37:3165–3171, Jun 1988.
- [33] M. Kramer, T. Plehn, M. Spira, and P. M. Zerwas. Pair production of scalar leptoquarks at the CERN LHC. *Phys. Rev.*, D71:057503, 2005.
- [34] Morad Aaboud et al. Search for scalar leptoquarks in pp collisions at $\sqrt{s} = 13$ TeV with the ATLAS experiment. *New J. Phys.*, 18(9):093016, 2016.
- [35] ATLAS Collaboration, G. Aad, B. Abbott, et al. Searches for scalar leptoquarks in pp collisions at $\sqrt{s} = 8$ TeV with the atlas detector. *The European Physical Journal C*, 76(1):5, Jan 2016.
- [36] Georges Aad et al. Search for third generation scalar leptoquarks in pp collisions at $\sqrt{s} = 7$ TeV with the ATLAS detector. *JHEP*, 06:033, 2013.

- [37] Albert M Sirunyan et al. Search for third-generation scalar leptoquarks decaying to a top quark and a τ lepton at $\sqrt{s} = 13$ TeV. 2018.
- [38] Ann Heinson. Useful diagrams of top signals and backgrounds. http://www-d0.fnal.gov/Run2Physics/top/top_public_web_pages/top_feynman_diagrams.html. Last update: October 29, 2011.
- [39] CERN. About CERN. <https://home.cern/about>. retrieved on September 4, 2018.
- [40] CERN. CERN Complex. http://www.lhc-facts.ch/img/news2015/lhccomplex_.jpg. Last update: October 29, 2011.
- [41] Lyndon Evans and Philip Bryant. LHC Machine. *Journal of Instrumentation*, 3(08):S08001, 2008.
- [42] The ALICE Collaboration, K Aamodt, et al. The ALICE experiment at the CERN LHC. *Journal of Instrumentation*, 3(08):S08002, 2008.
- [43] Gerfried J Wiener, Julia Woithe, Alexander Brown, and Konrad Jende. Introducing the lhc in the classroom: an overview of education resources available. *Physics Education*, 51(3):035001, 2016.
- [44] The LHCb Collaboration, A Augusto Alves Jr, et al. The LHCb Detector at the LHC. *Journal of Instrumentation*, 3(08):S08005, 2008.
- [45] The CMS Collaboration, S Chatrchyan, et al. The CMS experiment at the CERN LHC. *Journal of Instrumentation*, 3(08):S08004, 2008.
- [46] The ATLAS Collaboration, G Aad, et al. The ATLAS Experiment at the CERN Large Hadron Collider. *Journal of Instrumentation*, 3(08):S08003, 2008.
- [47] Rende Steerenberg. LHC report: LHC reaches 2017 targets. <https://home.cern/cern-people/updates/2017/11/lhc-report-lhc-reaches-2017-targets>. posted by Stefania Pandolfi on 7 Nov 2017. Last updated 26 Jun 2018.
- [48] Cheuk-Yin Wong. *Introduction to High-Energy Heavy-Ion Collisions*. WORLD SCIENTIFIC, 1994.
- [49] Alessandro La Rosa. The ATLAS Insertable B-Layer: from construction to operation. *JINST*, 11(12):C12036, 2016.

Bibliography

- [50] Georges Aad et al. Technical Design Report for the Phase-I Upgrade of the ATLAS TDAQ System. Technical Report CERN-LHCC-2013-018. ATLAS-TDR-023, Sep 2013. Final version presented to December 2013 LHCC.
- [51] Electron efficiency measurements with the ATLAS detector using the 2015 LHC proton-proton collision data. Technical Report ATLAS-CONF-2016-024, CERN, Geneva, Jun 2016.
- [52] T G Cornelissen, M Elsing, I Gavrilenco, J-F Laporte, W Liebig, M Limper, K Nikolopoulos, A Poppleton, and A Salzburger. The global χ^2 track fitter in atlas. *Journal of Physics: Conference Series*, 119(3):032013, 2008.
- [53] Morad Aaboud et al. Performance of the ATLAS Trigger System in 2015. *Eur. Phys. J.*, C77(5):317, 2017.
- [54] Samuel David Jones. The ATLAS Electron and Photon Trigger. Jun 2018.
- [55] Gabriella Pásztor. The Upgrade of the ATLAS Electron and Photon Triggers towards LHC Run 2 and their Performance. Technical Report ATL-DAQ-PROC-2015-053. arXiv:1511.00334, CERN, Geneva, Oct 2015. Comments: Presentation at the DPF 2015 Meeting of the American Physical Society Division of Particles and Fields, Ann Arbor, Michigan, August 4-8, 2015.
- [56] Georges Aad et al. Muon reconstruction performance of the ATLAS detector in proton-proton collision data at $\sqrt{s} = 13$ TeV. *Eur. Phys. J.*, C76(5):292, 2016.
- [57] Performance of the ATLAS Silicon Pattern Recognition Algorithm in Data and Simulation at $\sqrt{s} = 7$ TeV. Technical Report ATLAS-CONF-2010-072, CERN, Geneva, Jul 2010.
- [58] Hannah Elizabeth Herde. Muon reconstruction performance in ATLAS at Run-II. *PoS*, EPS-HEP2015:285, 2015.
- [59] Aranzazu Ruiz-Martinez and ATLAS Collaboration. The ATLAS Run-2 Trigger Menu for higher luminosities: Design, Performance and Operational Aspects. Sep 2017.
- [60] Georges Aad et al. Topological cell clustering in the ATLAS calorimeters and its performance in LHC Run 1. *Eur. Phys. J.*, C77:490, 2017.
- [61] M. Aaboud and others. Jet reconstruction and performance using particle flow with the atlas detector. *The European Physical Journal C*, 77(7):466, Jul 2017.

- [62] Matteo Cacciari, Gavin P. Salam, and Gregory Soyez. The anti- k_t jet clustering algorithm. *Journal of High Energy Physics*, 2008(04):063, 2008.
- [63] Per Ola Hansson Adrian. The ATLAS b-Jet Trigger. In *Proceedings, 31st International Conference on Physics in collisions (PIC 2011): Vancouver, Canada*, 2011.
- [64] Michela Paganini. Machine Learning Algorithms for b -Jet Tagging at the ATLAS Experiment. In *18th International Workshop on Advanced Computing and Analysis Techniques in Physics Research (ACAT 2017) Seattle, WA, USA*, 2017.
- [65] Luca Scodellaro. b tagging in ATLAS and CMS. In *5th Large Hadron Collider Physics Conference (LHCP 2017) Shanghai, China, May 15-20, 2017*, 2017.
- [66] Expected performance of the ATLAS b -tagging algorithms in Run-2. Technical Report ATL-PHYS-PUB-2015-022, CERN, Geneva, Jul 2015.
- [67] Optimisation of the ATLAS b -tagging performance for the 2016 LHC Run. Technical Report ATL-PHYS-PUB-2016-012, CERN, Geneva, Jun 2016.
- [68] Georges Aad et al. Reconstruction of hadronic decay products of tau leptons with the ATLAS experiment. *Eur. Phys. J.*, C76(5):295, 2016.
- [69] Reconstruction, Energy Calibration, and Identification of Hadronically Decaying Tau Leptons in the ATLAS Experiment for Run-2 of the LHC. Technical Report ATL-PHYS-PUB-2015-045, CERN, Geneva, Nov 2015.
- [70] Zinonas Zinonos. Reconstruction and identification of hadronic decays of tau leptons in ATLAS. In *Proceedings, 2nd Conference on Large Hadron Collider Physics Conference (LHCP 2014): New York, USA, June 2-7, 2014*, 2014.
- [71] Andy Buckley et al. General-purpose event generators for LHC physics. *Phys. Rept.*, 504:145–233, 2011.
- [72] Glen Cowan. *Statistical Data Analysis -*. Oxford University Press, New York, 1998.
- [73] J. Allison et al. Recent developments in Geant4. *Nuclear Instruments and Methods in Physics Research Section A: Accelerators, Spectrometers, Detectors and Associated Equipment*, 835:186 – 225, 2016.

Bibliography

- [74] Z. Marshall. The atlas simulation software. *Nuclear Physics B - Proceedings Supplements*, 197(1):254 – 258, 2009. 11th Topical Seminar on Innovative Particle and Radiation Detectors (IPRD08).
- [75] Julian Glatzer. Inclusive top pair production at 7, 8 and 13 TeV in ATLAS. Technical Report ATL-PHYS-PROC-2015-172, CERN, Geneva, Dec 2015.
- [76] Bingfang Yang and Ning Liu. One-loop QCD correction to top pair production in the littlest Higgs model with T-parity at the LHC. *EPL*, 111(1):11001, 2015.
- [77] The ATLAS collaboration. Measurements of the Higgs boson production cross section at 7, 8 and 13 TeV centre-of-mass energies and search for new physics at 13 TeV in the $H \rightarrow ZZ^* \rightarrow \ell^+ \ell^- \ell'^+ \ell'^-$ final state with the ATLAS detector. 2015.
- [78] J. Alwall, R. Frederix, S. Frixione, V. Hirschi, F. Maltoni, O. Mattelaer, H. S. Shao, T. Stelzer, P. Torrielli, and M. Zaro. The automated computation of tree-level and next-to-leading order differential cross sections, and their matching to parton shower simulations. *JHEP*, 07:079, 2014.
- [79] Sjöstrand, Torbjörn and Ask, Stefan and Christiansen, Jesper R. and Corke, Richard and Desai, Nishita and Ilten, Philip and Mrenna, Stephen and Prestel, Stefan and Rasmussen, Christine O. and Skands, Peter Z. An Introduction to PYTHIA 8.2. *Comput. Phys. Commun.*, 191:159–177, 2015.
- [80] Richard D. Ball et al. Parton distributions for the LHC Run II. *JHEP*, 04:040, 2015.
- [81] ATLAS Run 1 Pythia8 tunes. Technical Report ATL-PHYS-PUB-2014-021, CERN, Geneva, Nov 2014.
- [82] Simone Alioli, Paolo Nason, Carlo Oleari, and Emanuele Re. A general framework for implementing NLO calculations in shower Monte Carlo programs: the POWHEG BOX. *JHEP*, 06:043, 2010.
- [83] Studies on top-quark Monte Carlo modelling for Top2016. Technical Report ATL-PHYS-PUB-2016-020, CERN, Geneva, Sep 2016.
- [84] Morad Aaboud et al. Measurement of top quark pair differential cross-sections in the dilepton channel in pp collisions at $\sqrt{s} = 7$ and 8 TeV with ATLAS. *Phys. Rev.*, D94(9):092003, 2016.

- [85] David J. Lange. The EvtGen particle decay simulation package. *Nuclear Instruments and Methods in Physics Research Section A: Accelerators, Spectrometers, Detectors and Associated Equipment*, 462(1-2):152 – 155, 2001. BEAUTY2000, Proceedings of the 7th Int. Conf. on B-Physics at Hadron Machines.
- [86] ATLAS Software Project. ATLAS Software documentation. <https://atlassoftwaredocs.web.cern.ch/athena/>. Last update: April 24, 2017.
- [87] Glen Cowan. Discovery sensitivity for a counting experiment with background uncertainty. <https://www.pp.rhul.ac.uk/~cowan/stat/medsig/medsigNote.pdf>, 2012.
- [88] S. S. Wilks. The large-sample distribution of the likelihood ratio for testing composite hypotheses. *Ann. Math. Statist.*, 9(1):60–62, 03 1938.

Acknowledgment

This thesis would have been impossible without the aid and support of the following people and therefore I would like to thank *you*:

- Professor Thomas Trefzger for the opportunity to write my master thesis at the chair Lehrstuhl für Physik und ihre Didaktik and the great team work within the outreach project Netzwerk Teilchenwelt.
- Professor Raimund Ströhmer for all the constructive suggestions and the very helpful discussions.
- Dr. Mabsana Haleem for the supervision of my thesis, the detailed explanations even in times when you were not at the institute and all the instructive discussions about my topic and beyond.
- Verena Herget for the great time as colleague in the office, all the chatting about this and that, the proofreading in the evening and at weekends, the team work within the outreach project, for your friendship and the various leisure activities =).
- Dr. Deb Sankar Bhattacharya for all the helpful hints and the well-spent time for our photography projects - we are the “Trödeltrupp” xD.
- Denise Böhm for the fruitful collaboration within the outreach project and beyond: I enjoyed the time with you!
- Dr. Stephan Lück for the best lunch times in the kitchen - sorry for eating your salad - and all the inspiring chats about photography, film series, computers, games or whatever other topics we have found so far xD.
- Thorben Swirski for the proofreading, the happy debugging and the helpful explanations.

- Robin Boshuis and Lucas Klein for the pleasant atmosphere in the office as part-time colleagues ;)
- Susan Schäfer and Florian Treisch for your effort to organize the team building activities besides the work and the great time: I really enjoyed it!
- all other members of the chair and the secretaries for the pleasant atmosphere you created and that you were always helpful. Thanks. =)
- my close family, especially my parents and siblings, you always provided unfailing support and continuous encouragement throughout my years of study and writing this thesis. This accomplishment would not have been possible without them. Thank you. ☺

Declaration of Authorship

I hereby declare that I am the sole author of this master thesis and that I have not used any sources other than those listed in the bibliography and identified as references.

I further declare that I have not submitted this thesis at any other institution in order to obtain a degree.

Würzburg, 17 January 2019.

Daniel Adlkofer